Chem Soc Rev

REVIEW ARTICLE

View Article Online
View Journal | View Issue

Cite this: *Chem. Soc. Rev.*, 2019, **48**, 4854

The charge carrier dynamics, efficiency and stability of two-dimensional material-based perovskite solar cells

Bing Wang,[a] James Iocozzia,[a] Meng Zhang,[a] Meidan Ye,[b] Shicheng Yan,[c] Huile Jin,[d] Shun Wang,*[d] Zhigang Zou*[c] and Zhiqun Lin*[a]

Perovskites have been firmly established as one of the most promising materials for third-generation solar cells. There remain several great and lingering challenges to be addressed regarding device efficiency and stability. The photovoltaic efficiency of perovskite solar cells (PSCs) depends drastically on the charge-carrier dynamics. This complex process includes charge-carrier generation, extraction, transport and collection, each of which needs to be modulated in a favorable manner to achieve high performance. Two-dimensional materials (TDMs) including graphene and its derivatives, transition metal dichalcogenides (*e.g.*, MoS_2, WS_2), black phosphorus (BP), metal nanosheets and two-dimensional (2D) perovskite active layers have attracted much attention for application in perovskite solar cells due to their high carrier mobility and tunable work function properties which greatly impact the charge carrier dynamics of PSCs. To date, significant advances have been achieved in the field of TDM-based PSCs. In this review, the recent progress in the development and application of TDMs (*i.e.*, graphene, graphdiyne, transition metal dichalcogenides, BP, and others) as electrodes, hole transporting layers, electron transporting layers and buffer layers in PSCs is detailed. 2D perovskites as active absorber materials in PSCs are also summarized. The effect of TDMs and 2D perovskites on the charge carrier dynamics of PSCs is discussed to provide a comprehensive understanding of their optoelectronic processes. The challenges facing the PSC devices are emphasized with corresponding solutions to these problems provided with the overall goal of improving the efficiency and stability of photovoltaic devices.

Received 4th April 2019

DOI: 10.1039/c9cs00254e

rsc.li/chem-soc-rev

[a] *School of Materials Science and Engineering, Georgia Institute of Technology, Atlanta, GA 30332, USA. E-mail: zhiqun.lin@mse.gatech.edu*

[b] *Research Institute for Biomimetics and Soft Matter, Fujian Provincial Key Laboratory for Soft Functional Materials Research, Department of Physics, Xiamen University, Xiamen, 361005, China*

[c] *Eco-materials and Renewable Energy Research Center, National Laboratory of Solid State Microstructures, College of Engineering and Applied Sciences, Nanjing University, Nanjing 210093, People's Republic of China. E-mail: zgzou@nju.edu.cn*

[d] *Nano-materials & Chemistry Key Laboratory, Institute of New Materials and Industrial Technologies, Wenzhou University, Wenzhou, Zhejiang, 325035, P. R. China. E-mail: shunwang@wzu.edu.cn*

Bing Wang

Dr Bing Wang received her PhD from Nanjing University in 2014. She then worked as a research assistant at Eco-materials and Renewable Energy Research Center of Nanjing University. Her work involved photoelectrochemical devices for solar energy conversion. Now she is a postdoctoral research associate in prof. Zhiqun Lin's group in the School of Materials Science and Engineering at the Georgia Institute of Technology. Her current work focuses on the synthesis of high-performance perovskite solar cells.

James Iocozzia

Dr James Iocozzia obtained his Bachelor of Science in Polymer and Fiber engineering from the Georgia Institute of Technology in 2012. He received his PhD from the School of Materials Science and Engineering at the Georgia Institute of Technology in 2018. His research interests include nanocomposites, block copolymers, and hyper-branched polymer systems for the development of functional nano-materials in the areas of drug delivery, energy, and stimuli-responsive materials.

1. Introduction

Photovoltaic solar cells can convert energy from the sun into direct current electricity using the photovoltaic effect. Such devices have been regarded as a very promising energy generation source and attracted much attention from the academic community. Several photovoltaic solar cells have helped to shape the environment of renewable sources of energy, including silicon solar cells, III–V solar cells, quantum dot-sensitized solar cells, dye-sensitized solar cells, organic solar cells and perovskite solar cells (PSCs). Crystalline silicon is nontoxic and abundantly available, and allows for the fabrication of solar cells with up to 27% conversion efficiencies with negligible degradation. For these reasons, it has been the long term market leader. However, this mature technology is constrained by some fundamental drawbacks, such as high temperature and energy intensive manufacturing processes, and a relatively large global demand for Si. The effectiveness of crystalline solar cells depends strongly on their continuous structure with minimal grain boundaries to facilitate the movement of photo-generated carriers. The main commercial motivation for developing highly efficient photovoltaic solar cells is to reduce production costs and produce high-quality semiconductors. PSCs have rapidly emerged as one such candidate. The development of PSCs is on its way to challenging the dominance of polycrystalline silicon and other thin film technologies. High power conversion efficiencies can be achieved by simple low cost processing.[1]

The term "perovskite" is used to describe compounds with the formula ABO_3, in which A denotes the larger atom (cuboctahedral coordination) and B denotes the smaller atom. In general, A and B are two cations while O is an anion that bonds to both. The coordination may deviate from ideal due to the differences in the atomic radii of the constituents. This deviation from ideality is defined by the Goldschmidt tolerance factor (t). The Goldschmidt tolerance factor can predict the stability and distortion of the crystal structure of ABO_3 perovskite materials and is defined by the expression $t = (r_A + r_O)/[\sqrt{2}(r_B + r_O)]$, where r_A, r_B, and r_O are the ionic radii of A, B, and O, respectively.[2] Distortions from the cubic structure can arise from the

Meng Zhang

Dr Meng Zhang is presently a postdoctoral fellow at the School of materials chemistry and engineering at Georgia Institute of Technology, USA. She received her PhD degree in engineering thermophysics from Zhejiang University, China, in 2016. Her research focuses on solar conversion, including photocatalysis and perovskite solar cells.

Meidan Ye

Dr Meidan Ye is an Associate Professor in the Research Institute for Biomimetics and Soft Matter, Department of Physics at Xiamen University. She received her PhD in Physical Chemistry from the State Key Laboratory of Physical Chemistry of Solid Surfaces, and College of Chemistry and Chemical Engineering at Xiamen University in 2014. Her research work focuses on advanced nanostructured materials for energy devices and flexible electronics, such as perovskite solar cells, dye/quantum dot-sensitized solar cells, photocatalysis, supercapacitors and flexible sensors.

Shicheng Yan

Dr Shicheng Yan received his PhD in materials science from the Northwestern Polytechnical University (NWPU), P. R. China, in 2007. Then, he has been on the faculty of the Nanjing University (NJU) since 2010 and has served as Professor since 2017. His research interests include artificial photosynthesis and renewable energy. Technical details of these research topics focus on light-induced electron transfer reactions, reaction thermodynamics and kinetics, surface/interface chemistry, and photo/electrochemistry of semiconductor/liquid interfaces.

Huile Jin

Dr Huile Jin is an Associate Professor at college of Chemistry and Materials Engineering, Wenzhou University. His research interests include the development of advanced energy materials for supercapacitors, lithium-ion batteries and fuel cells. He has published more than 40 articles in journals including Adv. Mater., Adv. Energy Mater., J. Am. Chem. Soc., Angew. Chem., Int. Ed., etc. He is also listed as an inventor on over 30 patents. He was the recipient of "551 Talent Project of Wenzhou City" in 2016.

size-mismatch of the ions resulting in additional perovskite structures, such as layered two-dimensional (2D) perovskites.[3,4] The Ruddlesden–Popper (RP) phase is a form of layered perovskite structure which consists of 2D perovskite slabs interlayered with cations. The general formula of the RP phase can be written as $A_{n+1}B_nO_{3n+1}$ (with $n \geq 1$ representing the number of connected layers of vertex-sharing BO_6 octahedra).[3,5] The layer thickness of $A_{n+1}B_nO_{3n+1}$ increases as n increases. Perovskites are 2D materials at low n values. As n increases, structural gradients from 2D to 3D perovskites coexist.[6] When $n = \infty$, perovskites turn into a pure 3D form. Fig. 1 shows the ideal tetragonal unit cells for $n = 1$, 2, and 3 of RP-type 2D perovskites. Compared to typical three-dimensional (3D) ABO_3 perovskites, 2D perovskites have attracted a great deal of attention in recent years due to their combination of an advantageous 2D shape for facilitating charge carrier migration and perovskite composition possessing intrinsic photovoltaic properties.[7] Similar to conventional two-dimensional materials (TDMs), 2D perovskites can be assembled into uniform and ultrathin flexible films with highly oriented microstructures.[8] Layered perovskites can be grown in different forms by tailoring the alignment of crystallographic planes of their 2D slabs.[9] They also have long charge carrier diffusion lengths, high quantum yields,

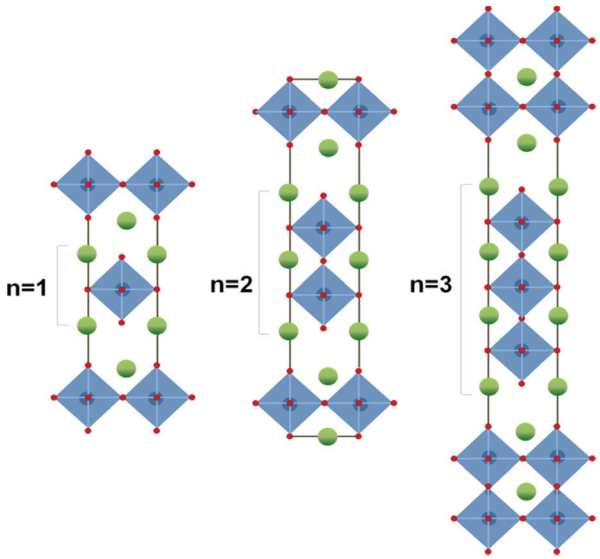

Fig. 1 The ideal Ruddlesden–Popper-type perovskite structure, $A_{n+1}B_nO_{3n+1}$ (n = 1, 2, 3; A atoms are the green balls, B atoms are the blue balls in the center of each octahedron, and O atoms are the red balls at the ends of each octahedron).

Shun Wang

Dr Shun Wang is a Professor at college of Chemistry and Materials Engineering, Wenzhou University. His research is focused on nanostructured functional materials, including carbon-based nanocomposites, functional Te nanocrystals, and hierarchically structured and assembled materials for electrochemical energy storage and conversion technology. He has published over 100 papers in journals including Nat. Commun., Adv. Mater., Adv. Energy Mater., J. Am. Chem. Soc., etc. He has also filed over 30 patents and patent applications. He is the editor-in-chief of Carbon Energy, and a recipient of "151 Talents of Zhejiang Province", "Excellent University Teachers of Zhejiang Province" and the prizes of science and technology of Zhejiang Province (Second Class).

Zhigang Zou

Dr Zhigang Zou has long-term devoted himself to the research field of new energy and photocatalytic materials. He has published 602 SCI-indexed articles, SCI-cited 24 338 times without self-citation, with an H-index of 74. Elsevier has continuously elected him as the most cited Chinese researcher for 5 years. He is now the "Yangtze River Scholars" distinguished professor at Nanjing University, the academician of the Chinese Academy of Science, and the academician of the Third World Academy of Science. He also serves as the member of the advisory board of NPG Asia Materials, the academic leader of the National Key Laboratory for nuclear chemical and chemical disaster protection, the leader of relative project of nuclear chemical and chemical disaster protection, and one member of the strategic Steering Committee of the hydrogen energy and fuel cell industry innovation strategy alliance of China.

Zhiqun Lin

Dr Zhiqun Lin received his PhD in Polymer Science and Engineering from the university of Massachusetts at Amherst in 2002. In 2004 he joined the Department of Materials Science and Engineering at the Iowa State University as an Assistant Professor and was promoted to Associate Professor in 2010. He moved to Georgia Institute of Technology in 2011, and became Professor of Materials Science and Engineering in 2014. His research interests include polymer-based nanocomposites, block copolymers, polymer blends, conjugated polymers, functional nanocrystals, solar cells, batteries, and hydrogen generation.

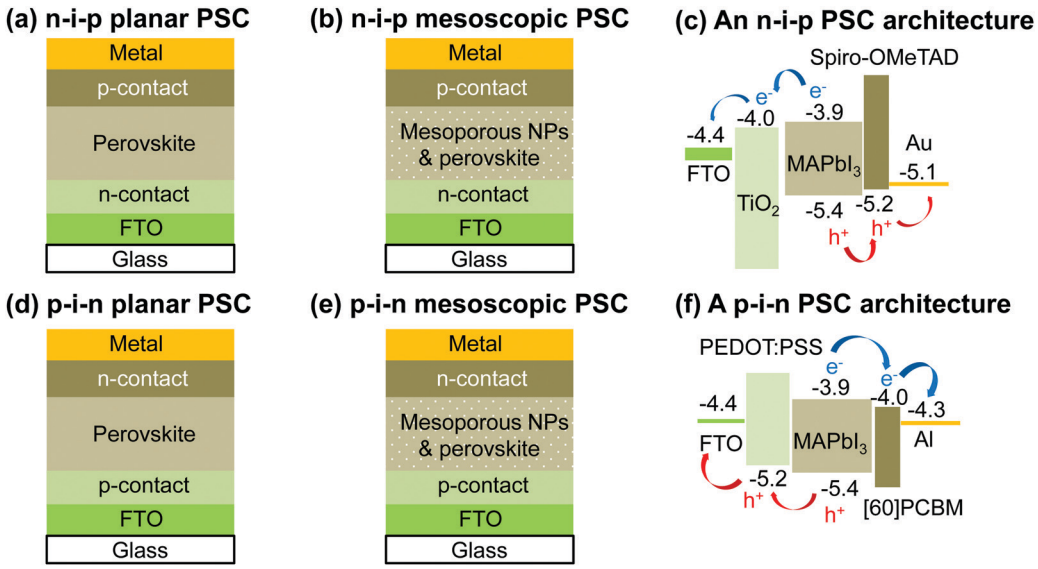

Fig. 2 Solid-state device architectures of (a) n-i-p planar and (b) n-i-p mesoscopic PSCs. (c) Energy band diagram of an n-i-p PSC architecture: FTO/TiO_2/$MAPbI_3$/Spiro-OMeTAD/Au. Solid-state device architectures of (d) p-i-n planar and (e) p-i-n mesoscopic PSCs. (f) Energy band diagram of a p-i-n PSC architecture: FTO/PEDOT:PSS/$MAPbI_3$/[60]PCBM/Al (note: NPs refers to nanoparticles).

high light absorption coefficients, and low rates of non-radiative charge recombination inherited from 3D perovskites.[10] Unlike 3D perovskites, 2D perovskites have tunable photoelectric properties and excellent environmental stability.[11] Solar cells based on layered 2D perovskites are detailed in this review.

Organic–inorganic metal halide perovskites are a class of compounds in the perovskite family with alternating layered structures of organic and inorganic constituents. Methylammonium lead iodide ($CH_3NH_3PbI_3$, or $MAPbI_3$) is one of the most common materials. It consists of a large organic cation, methylammonium ($CH_3NH_3^+$), lead (Pb) as the smaller cation and iodine as the halogen anion. This structure was first used in solar cells by Miyasaka *et al.* in 2009.[12] $CH_3NH_3PbX_3$ (X = Br, I) perovskite materials adsorbed on mesoporous TiO_2 were applied as a sensitizer in a dye-sensitized solar cell (DSSC) with a liquid electrolyte. Initially, $MAPbI_3$ dyes produced efficiencies around 3.8%.[12] However, liquid electrolytes often contain volatile and corrosive components which often leak within the device and reduce the lifetime of solar cells. In 2012, Park *et al.* used perovskite absorbers as the primary photoactive layer to fabricate solid-state meso-superstructured PSCs.[13] Spiro-MeOTAD and mesoporous TiO_2 were employed as the hole and electron transporting layers, respectively. The fabricated solar cell delivered a power conversion efficiency (PCE) of 9.7%.[13] Subsequently, extensive work has been devoted to improving the performance of PSCs by controlling the composition,[14–18] interfacial engineering,[19–22] and optimizing the device architecture.[18,23–26] These efforts resulted in a maximum reported certified PCE of 24.2%.[27] The general structure of a PSC is composed of an electrode layer, a perovskite photoactive layer, and charge transport layers (*i.e.*, a hole transporting layer (HTL) and an electron transporting layer (ETL)). In addition, buffer layers have also been inserted at the interfaces between the perovskite and HTL/ETL or HTL/ETL and electrode layers to improve the performance of PSC devices.[20,21,28,29] Bound electron–hole pairs are generated in the energy conversion process of PSCs. The charge carriers are then separated and shuttled to the corresponding electrode. As perovskites can conduct both electrons and holes,[30] the HTL and ETL are not necessary to fabricate a working PSC.[31,32] However, the use of charge transport layers can enhance the separation of electrons and holes. Most PSCs have adopted a structure in which the active perovskite compound is placed between the HTL and the ETL. Depending on the structure, PSCs generally have two types of solid-state device architectures:[33,34] mesoporous-structured PSCs that incorporate a mesoporous layer or a mesoporous-planar bilayer (p-i-n or n-i-p structure), and planar PSCs (p-i-n or n-i-p structure) in which all layers are planar (Fig. 2).

To date, numerous TDMs have been reported, and they can be categorized into groups based on their structural similarities:[35] (1) materials with atomic layers arranged in hexagonal honeycomb lattices, such as graphene,[36] borophene,[37] germanene,[38] hexagonal-boron nitride (h-BN),[39] and black phosphorus (BP);[40] (2) transition metal dichalcogenides[41,42] with the general stoichiometric formula of MX_2 (where M represents the transition metal and X represents the chalcogen, *e.g.*, MoS_2, $MoSe_2$ and WS_2); and (3) metal oxide nanosheets/nanoplates,[43–48] such as titania nanosheets[45,46] and ZnO nanoplates.[48] Due to their unique optical and electronic properties (Table 1), these TDMs have been widely investigated for many optoelectronic applications, such as solar cells,[49] photodetectors,[50,51] and light emitting devices.[52] In the context of PSCs, TDMs have been extensively explored as functional interlayers in different device architectures. In typical PSCs, the undesirable recombination of electrons and holes usually occurs during the charge transport process in which electrons in the perovskite layer recombine with holes in the HTL, and electrons in the ETL recombine with holes in the perovskite

Table 1 Optical and electrical properties of two-dimensional materials

2D materials	Band gap (eV)	Band type	Carrier mobility ($cm^2 V^{-1} s^{-1}$)	Ref.
Graphene	0	Direct	10^3–2×10^5	63 and 64
Graphdiyne	1.26	Direct	2×10^5	65
BP	1.60	Direct	10^4–2.6×10^4	66 and 67
Monolayer MoS_2	1.715	Direct	10–130	63
Bulk MoS_2	1.710–0.788	Indirect	30–500	63
Monolayer WSe_2	1.7	Direct	140–250	63
Bulk WSe_2	1.2	Indirect	500	63
h-BN	5.9	Direct	NA	63
SnO_2 nanosheet	3.6	Direct	100–200	68
ZnO nanosheet	3.4	Direct	20–40	69

layer. Inhibiting charge recombination is an effective way to improve the performance of PSCs. The interfaces within PSCs can be engineered through the addition of TDMs to enhance charge transport and improve performance. Consequently, the controlled synthesis of TDMs with well-defined structures and superior properties is essential for their large scale application in photovoltaics. Primary methods for the synthesis of TDMs include exfoliation[53–56] and chemical vapor deposition (CVD)[28,57–62] which will be discussed in the following sections.

2. Synthesis of traditional two-dimensional materials and layered perovskites

2.1 Preparation of two-dimensional materials

2.1.1 Exfoliation methods. The preparation of TDMs by exfoliation is cost-efficient and versatile because it can be combined with other chemical treatments to produce a variety of functionalized TDMs.[20,35,70–72] The mechanical exfoliation method is widely used to prepare single or few layered TDMs by the application of mechanical forces to solutions of layered materials *via* stirring, shaking, or ultra-sonication.[53–55] Surfactants are commonly employed to reduce van der Waals interactions which hold layers together as well as keep the exfoliated products suspended in the solvent.[53] Since most TDMs are hydrophobic, it is difficult to dissolve them directly in common solvents (such as water, ethanol, and acetone) without prior surface treatment. This challenge has been recently addressed by Lee *et al.*[56] They exfoliated bulk-layered materials (graphene, h-boron nitride, MoS_2, *etc.*) by controlling the temperature of the sonication bath. As shown in Fig. 3, the exfoliated 2D platelets remain well dispersed in water without using any surfactants for over a month.[56] The stability of the exfoliated nanoplatelets is attributed to the surface charges on the TDMs as a result of edge functionalization (hydroxyl- and carboxyl-functional groups on graphene materials) or their intrinsic polarity.[56] Compared with pristine graphene, carboxyl- and hydroxyl-functionalized graphene has a stronger positive and negative charge, respectively.[56] For h-BN, there are alternating layers of charge distribution resulting in strong polarity across the B and N termination edges. In contrast, MoS_2 exhibits moderate polarity due to the negative charge on the sulfur surface and counter charges on the inner molybdenum surface.[56] In addition to mechanical exfoliation, chemical exfoliation methods including ion intercalation[73] and solvent-based exfoliation[74] are employed to produce TDMs of one or a few layers. Chemical exfoliation methods are generally employed to exfoliate graphene oxide (GO) from oxidized graphite[75] by reacting graphite with strong acids (*e.g.*, nitric acid) and/or oxidants (*e.g.*, $KMnO_4$), known as the modified Hummers' method.[76] Unfortunately, these methods are not suitable for synthesizing large area TDMs due to the low yield and inability to control sheet size and layer number.

2.1.2 Chemical vapor deposition. Compared to the exfoliation method, chemical vapor deposition (CVD) has been recognized as a popular method to grow high-quality TDM films on a large reproducible scale.[28,57–62] CVD growth of TDMs involves activated chemical reactions of precursors in a specially controlled environment. It uses transition metals (*e.g.*, Pt, Ni) as catalysts. It is possible to change the process of TDM production by adjusting the catalyst to prepare films with different qualities. Fig. 4 summarizes the general experimental setup of a CVD experiment for preparing two-dimensional graphene. The setup consists of a furnace, a quartz chamber, a control system and mass flow controllers (MFC) for reactant gases.[62] The precursors, conditions, atmosphere, substrates and catalysts are several key factors affecting the final quality of TDMs.

2.2 Layered two-dimensional perovskites

2.2.1 The structure of two-dimensional perovskites. Two-dimensional perovskites have a layered structure. The most commonly reported layered 2D perovskite possesses an orientation.[77,78] The general formula of layered perovskite compounds is $L_2(ABX_3)_{n-1}BX_4$, where L represents long chain organic cations (*e.g.*, octylammonium and butylammonium), A represents monovalent metal or organic molecular cations (*e.g.*, Cs^+, $CH_3NH_3^+$ and $C_2H_5NH_3^+$), B represents divalent metal cations (*e.g.*, Pb^{2+}, Cu^{2+}, Sn^{2+}, Ni^{2+}, and Ge^{2+}), X represents halide anions (*e.g.*, Cl^-, Br^-, and I^-), and n represents the number of metal halide octahedral layers between the two layers of the long chain organic cations ($n \geq 1$). As the perovskite layer number is reduced, the bandgap gradually increases from E_g = 1.60 eV ($n = \infty$) to 1.89 eV ($n = 4$), 2.00 eV ($n = 3$), 2.14 eV ($n = 2$) and 2.40 eV ($n = 1$) for the perovskite $MAPbI_3$, as shown in Fig. 5.[79–81] Due to the presence of stable excitons with a large binding energy, 2D perovskites exhibit attractive optical properties. For example, it is reported that 2D perovskites can exhibit a four times stronger third harmonic generation in the mid-infrared range over the 3D counterpart because of strong quantum confinement.[81] The substantial carrier mobility in the plane of the perovskite sheet can be realized due to its controlled long-range out-of-plane orientation for nondispersive charge transport. This property makes such systems strongly applicable to optical devices.[82,83]

2.2.2 Preparation of two-dimensional perovskites

2.2.2.1 Liquid phase methods. An efficient method to produce hybrid 2D perovskites is to exchange the cations present in perovskite nanocrystals with long chain alkyl cations. Fig. 6a shows the process whereby 2D perovskite layers can be produced from 3D crystal structures by blocking the interaction of layered

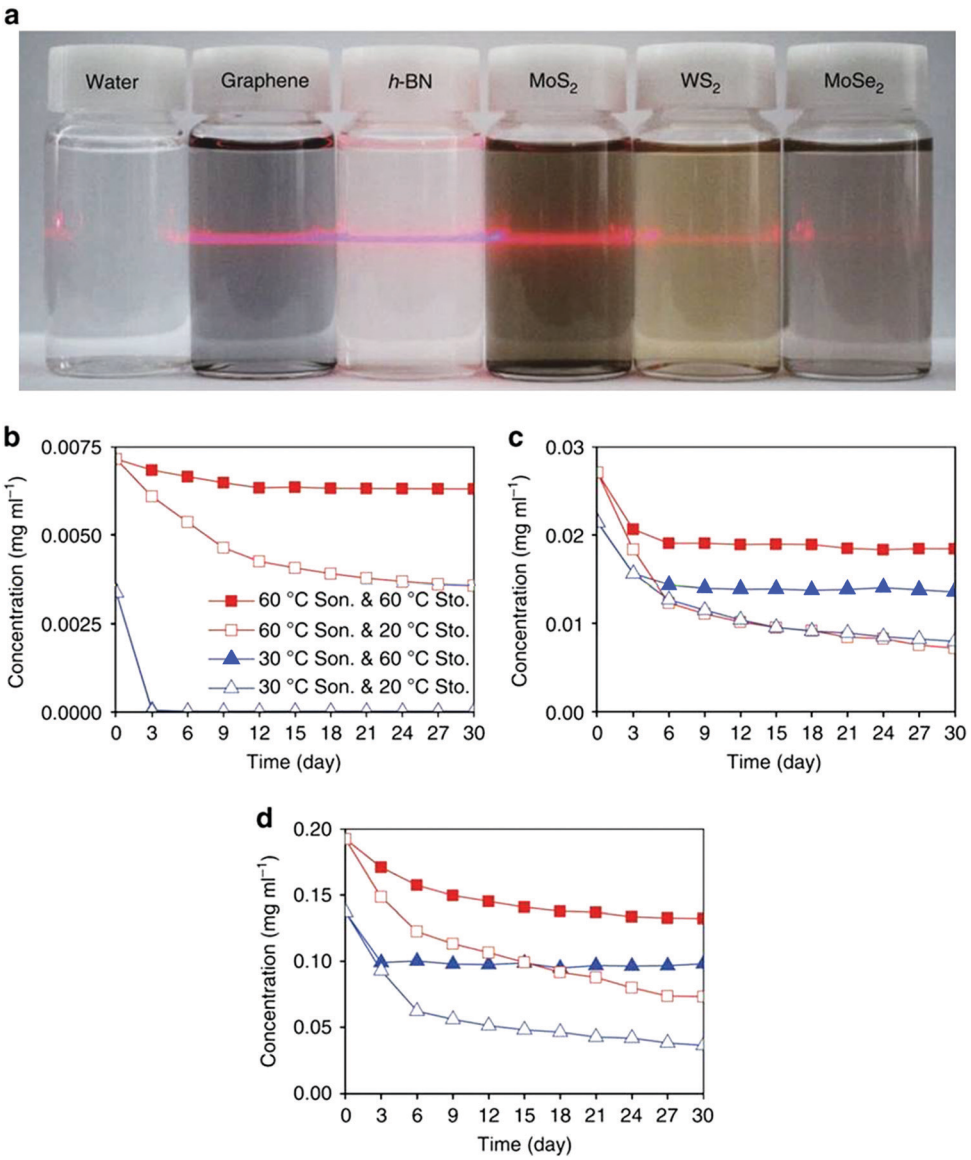

Fig. 3 (a) Digital images of five different TDM aqueous solutions one month after dispersion. The long-term solution stability of (b) graphene, (c) h-BN and (d) MoS_2 sonicated at 60 °C and 30 °C and stored at 60 °C and 20 °C. Squares and triangles refer to sonication at 60 °C and 30 °C, and solid and blank symbols denote storage at 60 °C and 20 °C, respectively. Reproduced from ref. 56 with permission from Springer Nature, copyright 2015.

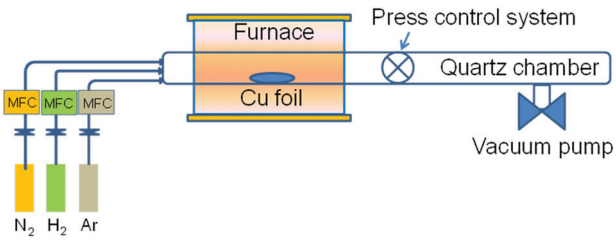

Fig. 4 Schematic showing a typical chemical-vapor-deposition setup. Mass flow controllers (MFC) supply reactant gases at the necessary flow rate. Pressure and vacuum control systems are used to adjust TDM growth conditions, and Cu foil is used as a catalyst.

perovskites using long organic molecular chains in the "A" position.[84] In this method, self-assembly between metal halides and organic chains is driven by coordination, hydrogen bonding and van der Waals forces upon mixing. The length of the chains is crucial as it drives the reorganization to form 2D structures. Liquid phase methods using organic alkyl ammonia derivatives as the long alkyl chain source are the most commonly used for synthesizing perovskites with different morphologies,[85–87] including perovskite nanosheets and nanoplatelets, due to their simplicity and low cost. The size and morphology of 2D perovskites can be tuned by controlling the surfactant and mass ratio of organic cations in the perovskite. 2D perovskites prepared by a liquid phase method were firstly reported by Tisdale *et al.* in early 2015.[85] 2D $CH_3NH_3PbBr_3$ perovskite nanoplatelets (single unit cell is shown in Fig. 6b) are synthesized with octylammonium bromide $CH_3(CH_2)_7NH_3Br$ as the long-chain ligand. 2D nanoplatelets of $CH_3NH_3PbBr_3$ with different thicknesses were obtained by a

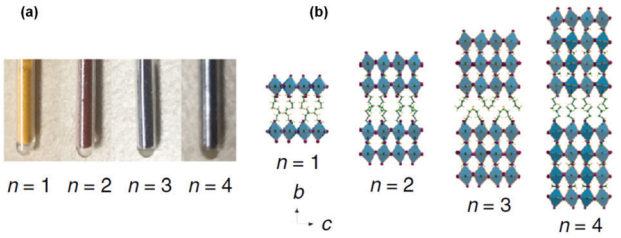

Fig. 5 (a) A photograph of perovskite sample powders; the colors indicate a blue shift in the band gap with a reduction in layer number, *n*. (b) Crystal structures viewed along the (100) crystallographic projection. Pb^{2+} atoms are represented by dark green balls, I^- atoms by purple balls, N atoms by dark blue balls, H atoms by yellow balls, and C atoms by light green balls. Reproduced from ref. 81 with permission from Springer Nature, copyright 2017.

slight modification of the synthesis method. 2D all-inorganic perovskite $CsPbBr_3$ nanosheets[88,89] and $CsPb_2Br_5$ nanosheets[90,91] can also be synthesized in the liquid phase with ammonium derivatives as the long chain source. The as-synthesized nanosheets can be well dispersed for fabricating solution-based optoelectronic devices. Balakrishnan and Kamat used an ammonium salt with long alkyl chains, dodecyl dimethylammonium bromide (DDAB), to induce the exfoliation of perovskite nanocrystals by forming an intermediate $PbBr^{3-}$ complex followed by reorganization to transform $CsPbBr_3$ nanocrystals into crystalline two-dimensional $CsPb_2Br_5$ nanosheets (Fig. 6c).[90] Such structural transformations are important for surface treatment to passivate defect sites and design 2D interfaces.

2.2.2.2 Vapor phase methods. Vapor phase methods transform the perovskite precursor into the gas phase through sublimation, evaporation or decomposition. Then, the saturated vapor is condensed into a crystal. The methods include both chemical vapor deposition[92] and van der Waals expitaxy.[93]

The former technique can offer conformal and controllable thin film growth whereas the latter enables the vapor phase epitaxial growth of perovskites with mismatched lattice constants. Compared with liquid phase methods, vapor phase methods synthesize more uniform films over larger areas with improved crystallinity and reduced impurities.[94,95] However, these methods involve more complex physical and chemical processes, are more energy intensive and are more difficult to scale up.[96,97]

At present, vapor phase methods are generally used to prepare 2D perovskite materials in either one step[93,94] or two steps.[59,95–97] The one-step method directly uses a mixture of all the precursors, such as PbX_2 and CH_3NH_3X for synthesizing $CH_3NH_3PbX_3$, as raw starting materials. Then the perovskite nanosheets are produced from the above precursor vapors in a vacuum quartz tube under reduced pressure. The two-step method involves first the deposition of a PbX_2 film under vacuum which is then placed into a quartz reaction tube. Next, the CH_3NH_3X powder is placed in the middle of the quartz tube. When the reaction begins, CH_3NH_3X under an Ar or N_2 airflow reacts with the surface of the PbX_2 film. CH_3NH_3X molecules insert into the PbX_2 layer leading to the formation of the 2D perovskite. Shi *et al.* employed a one-step method to grow thin $CH_3NH_3PbCl_3$ perovskite platelets on a muscovite mica

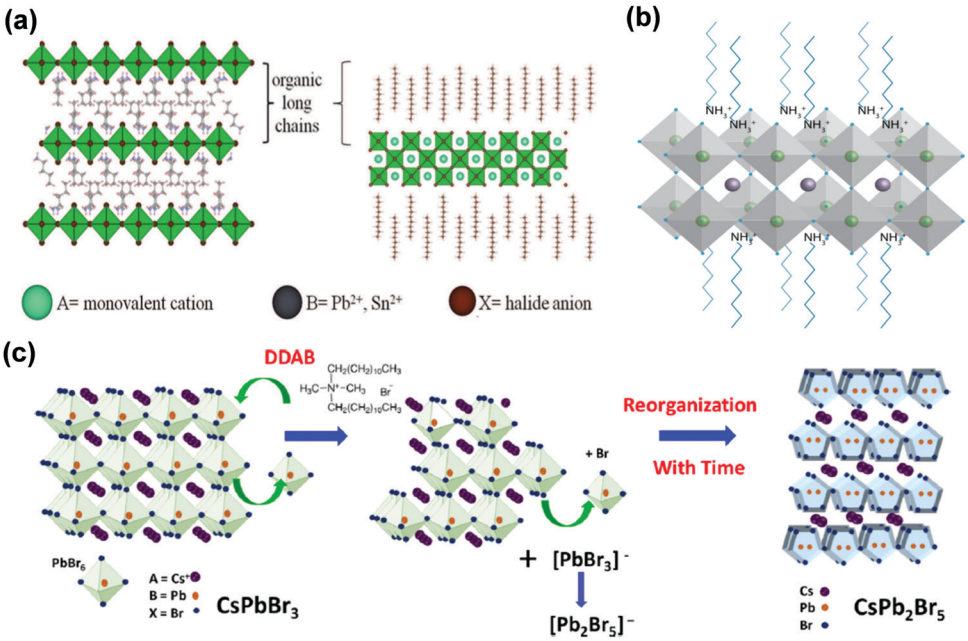

Fig. 6 (a) 2D layered perovskite crystal structures (lateral view and top view). Reproduced from ref. 84 with permission from John Wiley and Sons, copyright 2017. (b) 2D perovskite nanoplatelets one unit cell thick. Reproduced from ref. 85 with permission from American Chemical Society, copyright 2015. (c) Schematic representation of ligand-assisted exfoliation and transformation of cubic $CsPbBr_3$ perovskite nanocrystals to tetragonal $CsPb_2Br_5$ nanosheets.[90] The addition of DDAB into the $CsPbBr_3$ solution induces the formation of $[PbBr_3]^-$ *via* the reaction $nCsPbBr_3 + DDA^+ \rightarrow (n - x)CsPbBr_3 + xDDA^+[PbBr_3]^- + xCs^+$. Then, the $[PbBr_3]^-$ complex reorganizes to form the stable $[Pb_2Br_5]^-$ species which combines with Cs^+ to form $CsPb_2Br_5$. Reproduced from ref. 90 with permission from American Chemical Society, copyright 2018.

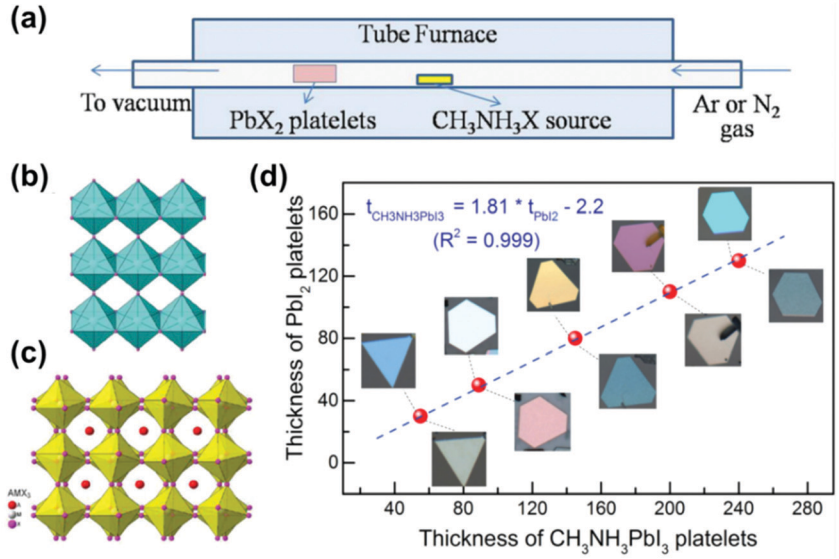

Fig. 7 (a) Schematic showing the setup for synthesizing the methyl ammonium lead halide perovskite ($CH_3NH_3PbX_3$, X = Cl, Br, I) using a vapor-transport system. (b) Structure of PbI_2 in which the Pb atoms are at the center of the halide octahedron. (c) Structure of $CH_3NH_3PbX_3$ in which the $CH_3NH_3^+$ groups (red spheres) are located within the center of eight lead halide octahedra. (d) Thickness of PbI_2 platelets before (images above the data line) and after (images below the data line) being converted to $CH_3NH_3PbI_3$. Reproduced from ref. 95 with permission from John Wiley and Sons, copyright 2014.

substrate by van der Waals epitaxy.[93] They simultaneously placed all the inorganic and organic precursors, $PbCl_2$, CH_3NH_3Cl powders and the muscovite mica substrate, in an alumina tube followed by heating in argon. To control the reaction process, the precursors and muscovite mica substrate were carefully placed to ensure uniform deposition.[93] As a result, ultrathin (sub-10 nm) and large-sized (a few tens of micrometers in length and width) crystalline 2D perovskite thin films were obtained on layered muscovite mica. Xiong *et al.* synthesized $CH_3NH_3PbX_3$ perovskite nanoplatelets using a two-step vapor phase process beginning with the growth of lead halide nanoplatelets *via* van der Waals epitaxy followed by a gas–solid heterogeneous reaction with methylammonium halide vapor to convert the as-grown platelets into the perovskite.[95] The experimental setup is shown in Fig. 7. The thicknesses of the PbI_2 and $CH_3NH_3PbI_3$ platelets have a linear relationship as they grow. This is consistent with the *c* lattice ratio.[95]

Different synthesis methods for TDMs and 2D perovskites greatly impact their performance in PSC devices due to their distinct optical and electronic properties.[59,98,99] TDMs have been reported as electrodes and charge transport layers (*i.e.*, HTL, ETL and buffer layer) in PSCs because they can separate and collect photo-generated charge carriers produced in perovskite absorbers which affects the performance (the open circuit voltage V_{OC}, the short circuit current density J_{SC} and fill factor FF) of PSCs. In addition, 2D layered perovskite absorbers have also been widely studied due to their impact on PSC performance. Table 2 summarizes the performance of TDM/2D perovskite-incorporated PSCs reported in recent studies which are addressed in this review. In the next sections, the effect of TDMs or 2D perovskites on the charge-carrier dynamics, efficiency and stability of PSCs is reviewed and discussed.

3. Two-dimensional material-based perovskite solar cells

3.1 Conductivity, transmittance and stability of graphene electrode charge carrier collectors

Transparent electrodes are critical to high-performance PSCs. An ideal transparent electrode should be highly conductive, inexpensive, stable, and an effective charge collector. Transparent electrodes in PSCs have been prepared mainly with indium tin oxide (ITO) or poly(3,4-ethylenedioxythiophene):poly(styrenesulfonate) (PEDOT:PSS). However, conventional transparent ITO electrodes are fragile (essentially metal doped glass) and the PEDOT:PSS-based transparent electrodes are hydroscopic (absorb moisture from the atmosphere) leading to the destruction of the perovskite layers which are water soluble.[134] Consequently, more suitable flexible transparent electrode materials are urgently needed for PSCs. Graphene is one promising material for PSC electrodes due to its composition of earth abundant carbon, excellent electrical and optical properties, and mechanical toughness.[98] Large-area graphene grown by CVD was implemented as a transparent electrode in PSCs.[28] Graphene-based PSCs showed high optical transmission below the perovskite energy bands leading to superior charge collection efficiency.[98] Graphene bottom electrodes in flexible inverted PSCs can enhance the photovoltaic performance of the PSC owing to their improved morphology and higher transparency as compared to those based on other carbon allotropes such as carbon nanotubes.[98] However, the transfer step for depositing graphene electrodes into PSC devices has lower reproducibility, which can significantly affect the conductivity of graphene electrodes. Thus, a more consistent graphene transfer method is required to improve its reproducibility and justify the use of

Table 2 Performance of TDM/2D perovskite-incorporated PSCs

No.	Function	2D materials	Synthesis method	Device structure	V_{OC} (V)	J_{sc} (mA cm^{-2})	FF	PCE (%)	Ref.
1	Electrode	Graphite	Exfoliation	n-i-p mesoscopic	0.90	23.0	0.68	14.1	100
2	Electrode	Graphene	CVD	n-i-p planar	0.95	17.8	0.72	12.0	57
3	Electrode	Graphene	CVD	p-i-n planar	1.00	21.7	0.78	16.8	99
4	Electrode	$AuCl_3$-Doped graphene	Photolithography patterning	p-i-n planar	1.09	21.0	0.78	17.9	101
5	Electrode	NdS_2	Exfoliation	n-i-p mesoscopic	1.05	14.3	0.53	8.3	102
6	ETL	Graphene/TiO_2	Exfoliation	n-i-p mesoscopic	1.04	21.9	0.73	15.6	103
7	ETL	Graphene/ZnO	Commercially available	n-i-p planar	0.93	20.0	0.56	10.3	77
8	ETL	Graphene/$SrTiO_3$	Exfoliation	n-i-p mesoscopic	1.00	18.1	0.58	9.4	104
9	ETL	Graphene/polymer	Exfoliation	n-i-p mesoscopic	0.95	19.3	0.64	13.4	105
10	ETL	rGO/TiO_2	Exfoliation	n-i-p mesoscopic	0.93	22.0	0.71	14.5	106
11	ETL	rGO/TiO_2	Exfoliation	n-i-p mesoscopic	0.84	16.5	0.67	9.3	107
12	ETL	rGO/TiO_2–Li	Exfoliation	n-i-p mesoscopic	1.11	22.0	0.80	19.5	108
13	ETL	Graphene–TiO_2/GO–Li	Exfoliation	n-i-p mesoscopic	1.03	22.6	0.69	16.2	109
14	ETL	rGO/Zn_2SnO_4	Exfoliation	n-i-p mesoscopic	1.05	22.5	0.76	17.9	110
15	ETL	Naphthalene diimide–graphene/SnO_2	Exfoliation	n-i-p planar	1.08	22.7	0.82	20.2	111
16	ETL	GD/PCBM	Exfoliation	p-i-n planar	0.97	23.4	0.65	14.8	23
17	ETL	GD/fullerene	Exfoliation	n-i-p planar	1.11	23.3	0.78	20.2	112
18	ETL	PCBM(GD)/ZnO(GD)	Exfoliation	n-i-p planar	1.05	24.1	0.79	20.0	113
19	ETL	TiS_2	Exfoliation	n-i-p planar	1.00	24.7	0.75	18.8	114
20	ETL	SnO_2 nanosheet	Hydrothermal method	n-i-p mesoscopic	1.08	22.6	0.71	17.3	115
21	HTL	GO	Exfoliation	p-i-n planar	0.94	13.7	0.52	6.6	18
22	HTL	PEDOT/GO	Exfoliation	p-i-n planar	1.02	21.6	0.82	18.1	116
23	HTL	GO/PEDOT:PSS	Commercially available	p-i-n planar	0.84	15.8	0.74	9.7	117
24	HTL	GO/PEDOT:PSS	Exfoliation	p-i-n planar	0.96	18.0	0.76	13.1	118
25	HTL	rGO	Exfoliation	p-i-n planar	0.95	14.8	0.71	10.0	119
26	HTL	rGO/PEDOT:PSS	Exfoliation	p-i-n planar	0.95	17.1	0.64	10.6	120
27	HTL	GD/P3HT	Exfoliation	n-i-p mesoscopic	0.94	19.6	0.71	13.2	121
28	HTL	GD/P3CT-K	Exfoliation	p-i-n planar	1.06	22.8	0.81	19.5	122
29	HTL	BP	Exfoliation	n-i-p mesoscopic	1.06	20.2	0.76	16.4	25
30	HTL	MoS_2	Exfoliation	p-i-n planar	1.01	20.7	0.78	16.4	123
31	HTL	WS_2	CVD	p-i-n planar	0.82	15.9	0.64	8.1	124
32	HTL	1T-rich MoS_2	Exfoliation	p-i-n planar	0.87	20.3	0.77	13.6	125
33	HTL	1T-rich WS_2	Exfoliation	p-i-n planar	0.93	20.6	0.72	13.8	125
34	Buffer layer between Perov./ETL	GO–Li	Exfoliation	n-i-p mesoscopic	1.02	20.0	0.70	14.3	20
35	Buffer layer between ETL/electrode	GO–Li/TiO_x sol	Exfoliation	p-i-n planar	0.91	15.6	0.72	10.2	72
36	Buffer layer between Perov./HTL	MoS_2	Exfoliation	n-i-p mesoscopic	0.93	21.5	0.67	13.3	126
37	Buffer layer between Perov./HTL	rGO/4FPH	Exfoliation	n-i-p planar	1.11	21.5	0.79	18.7	22
38	Buffer layer between HTL/electrode	rGO	Exfoliation	n-i-p mesoscopic	1.11	23.2	0.78	20.4	127
39	Absorber	GO/$MAPbI_3$	Exfoliation	n-i-p planar	1.07	23.7	0.69	17.6	128
40	Absorber	$(BA)_2(MA)_2Pb_3I_{10}$	Liquid phase method	p-i-n planar	1.01	16.7	0.74	12.5	129
41	Absorber	$(PEA)_2(MA)_2[Pb_3I_{10}]$	Liquid phase method	n-i-p planar	1.18	6.7	0.60	4.7	130
42	Absorber	$MAI(PbI_2)_{1-x}(FeCl_2)_x$	Liquid phase method	n-i-p planar	1.10	22.2	0.71	17.3	131
43	Absorber	$(PEA)_2FA_8Sn_9I_{28}$	Liquid phase method	p-i-n planar	0.58	14.2	0.62	5.1	132
44	Absorber	$(HOOC(CH_2)_4NH_3)_2PbI_4$/$MAPbI_3$	Commercially available	n-i-p mesoscopic	1.03	18.8	0.75	14.6	133

Perov.: perovskite active layer; GO: graphene oxide; rGO: reduced graphene oxide; GD: graphdiyne; BP: black phosphorus; P3HT: poly(3-hexylthiophene); 4-FPH: 4-fluorophenyl; MA: methylammonium; FA: formamidinium; BA: *n*-butylammonium; PEA: phenylethylammonium. Devices labelled no. 1–5 are discussed in Section 3.1; no. 6–20 are discussed in Section 3.2; no. 21–33 are discussed in Section 3.3; no. 34–38 are discussed in Section 3.4; no. 39–44 are discussed in Section 4.

highly conductive graphene electrodes in PSC devices. Yan *et al.* first reported the fabrication of semi-transparent PSCs by laminating stacked multi-layer graphene prepared by CVD as the top transparent electrode.[57] To improve the reproducibility of the graphene electrodes, the graphene film was first coated with a layer of poly(methyl methacrylate) (PMMA). Subsequently, a poly(dimethylsiloxane) (PDMS) film was deposited onto the PMMA film to improve the mechanical strength of the graphene electrode. The PDMS/PMMA/graphene film can be easily transferred and laminated onto a solar cell. As the sheet resistance of graphene films (1050 ± 150 Ω sq^{-1}) is high, a thin layer of poly-(3,4-ethylenedioxythiophene):poly(styrenesulfonate) (PEDOT:PSS) was employed as an adhesion layer (sticky coating) on the perovskite layer to improve the conductivity of the graphene electrode. The layer and band structures of devices are shown in Fig. 8a and b. Multilayer graphene films can decrease transmittance, and affect the light absorption of the active layers in PSCs. The use of two-layered graphene doped with PEDOT:PSS as the electrode offered lower sheet resistance (140 ± 35 Ω sq^{-1}, Fig. 8c) and higher transmittance (>90% in the visible region, Fig. 8d) in the visible region.[57] The average PCE of the optimized device with double-layer graphene electrodes reached 12.02% and 11.65% when illuminated from the bottom (FTO side) and top (graphene side), respectively.

Despite the high conductivity of graphene electrodes achieved, one major difficulty in the preparation of graphene

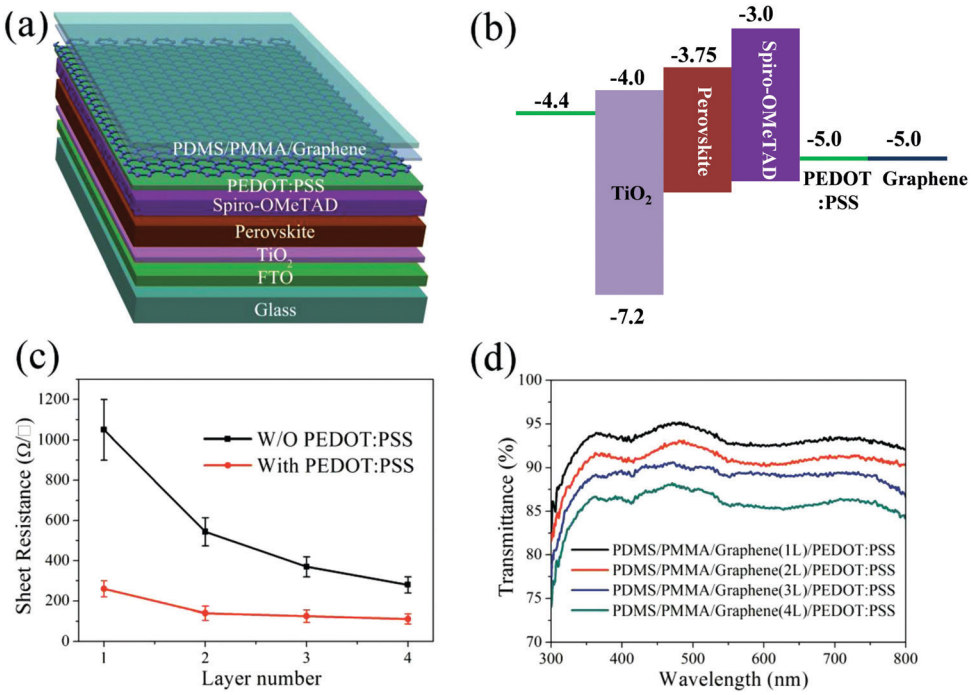

Fig. 8 (a) Layer and (b) band structures of a PSC. (c) Sheet resistance of graphene films before and after PEDOT:PSS doping. (d) UV-vis spectra of PEDOT:PSS doped graphene electrodes with graphene. Reproduced from ref. 57 with permission from John Wiley and Sons, copyright 2015.

electrodes is that the transfer polymers such as PMMA cannot be completely removed from the graphene surface. The residual transfer polymers can affect the quality of carrier transport layers and perovskite layers coated on the electrode surface. Poly(3-hexylthiophene) (P3HT) is found to be a good candidate as the supporting polymer of graphene electrodes.[58] The P3HT-transferred graphene film is cleaner than the PMMA-transferred one. As P3HT is a p-type semiconductor, it can induce p-type doping in graphene and consequently increase the conductivity of graphene. The graphene film prepared with P3HT exhibits a lower sheet resistance ($\sim$300 Ω sq^{-1}) than that prepared with PMMA ($\sim$500 Ω sq^{-1}).[58] With the P3HT-transferred transparent graphene electrode, a PSC with the structure of ITO/graphene/P3HT/$MAPbI_3$/$PC_{71}BM$/Ag can achieve the best PCE of 14.6%. In addition, PSCs using graphene electrodes show good bending durability due to the high flexibility of the electrodes.[58] The resistance of the graphene electrode was unchanged after 500 bending tests (bending radius of 0.175 cm).[58] Jung, Chio *et al.* fabricated flexible PSCs utilizing graphene as the bottom transparent electrode and analyzed their bending durability (Fig. 9a and b).[99] The terms "Gr-Mo/PEN device" and "ITO/PEN device" refer to PSC devices fabricated on polyethylene naphthalate (PEN) substrates containing a MoO_3/graphene electrode or ITO electrode, respectively. The MoO_3 layer was used to optimize the wettability of the graphene surface which enables the formation of uniform PEDOT:PSS layers.[135] Moreover, the MoO_3 layer can decrease the sheet resistance of the single layer graphene by over 50% from 1260 Ω sq^{-1} to 552 Ω sq^{-1} due to the p-type doping of MoO_3 on graphene.[99] This behavior is similar to the function of the P3HT polymer previously mentioned.[58] Interestingly, despite the higher sheet resistance of the MoO_3/graphene electrode (552 Ω sq^{-1}) *versus* the ITO electrode (13.3 Ω sq^{-1}), the PSC devices using these two electrodes showed similar J_{sc} values due to the fact that graphene transmitted more light (>97% transmittance) than ITO (>89% transmittance).[99] The PSC device with the Gr/Mo electrode reached a PCE of 16.8% with no hysteresis and exhibited improved stability under bending deformation, maintaining PCEs > 90% of peak efficiency after 1000 bending cycles (Fig. 9c and d).[99] However, the ITO/PEN device decreased to only 40% of its initial value after 1000 bending cycles. This could be attributed to a significantly higher failure strain of graphene ($\sim$25%)[136] than that of ITO ($\sim$1%).[137] Graphene could withstand more severe mechanical deformation than ITO before generating cracks on the surfaces. The excellent mechanical toughness of the Gr-Mo/PEN device strongly suggests that perovskite photovoltaics with graphene electrodes can pave the way to flexible photovoltaic applications.

Ultimately, the graphene electrode is sufficiently transparent to allow significant light transmittance (>97%), thus allowing it to overcome the drawbacks of the higher sheet resistance and lower charge collection efficiency with respect to traditional anode materials such as ITO. Graphene is exceedingly ductile, and the failure strain of graphene is about 25 times greater than that of ITO.[136,137] Consequently, the use of graphene electrodes in flexible PSC devices reduces the chances of crack formation under bending conditions, leading to stable electrical performance under significant degrees of deformation. This unique combination of stable performance while bending makes such devices particularly apt for portable and wearable electronics.

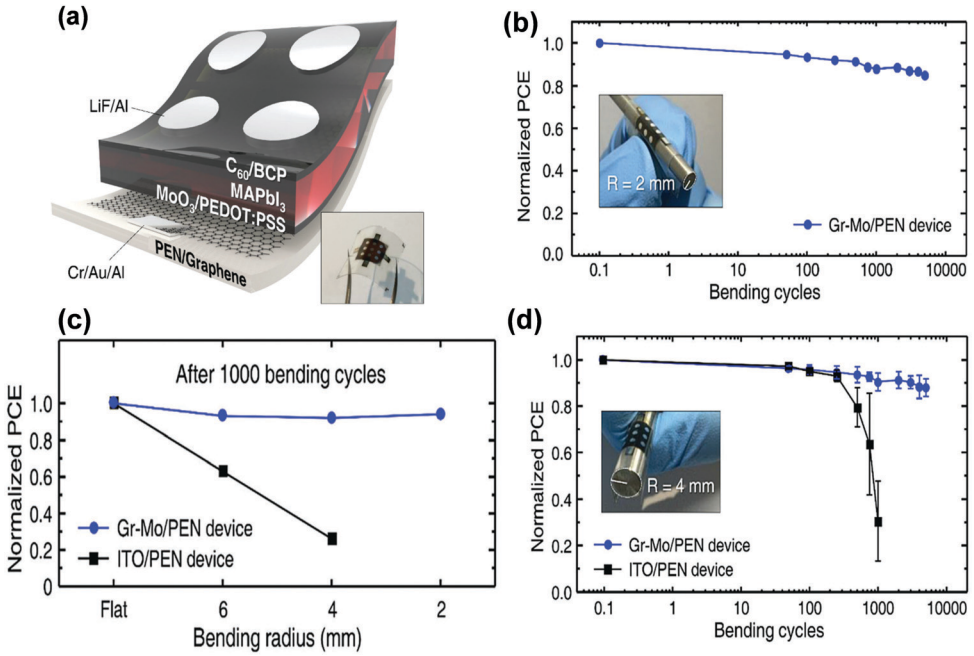

Fig. 9 (a) Structure of graphene-based PSCs (inset: a photograph). (b) Bending stability test of graphene-based PSCs. (c) Normalized PCEs measured after 1000 bending cycles. (d) Normalized PCEs at a bending radius (R) of 4 mm (inset: the Gr-Mo/PEN device bent at R = 4 mm). Reproduced from ref. 99 with permission from The Royal Society of Chemistry, copyright 2016.

Although graphene is a promising electrode material in PSCs, the sheet resistance of currently prepared graphene thin films remains high. Also, the high tensile strength of graphene leads to fracturing at low strain. This makes it challenging to take advantage of its extraordinary electronic properties in PSCs.[138] It is important to reduce the sheet resistance while maintaining the high light transmissivity of the graphene thin film to ensure good performance of graphene-based PSC devices. Doping of graphene with materials such as P3HT[58] and MoO_3[99] has proven to be an efficient method to reduce the sheet resistance of the graphene electrode in PSCs. This is because the doping optimizes the work function of graphene to minimize the energy barrier between the electrode and charge transport layers to enable efficient charge collection. For example, the work function was elevated from 4.23 eV to 4.71 eV and from 4.29 eV to 4.72 eV by hole-doping of MoO_3 into graphene and ITO anodes, respectively.[135] A MoO_3 interfacial layer with a thickness of 2 nm achieved a desirable energy level alignment between the graphene anode and the HTL.[135] As a result, a peak PCE of 17.1% was realized.[135] $AuCl_3$ can also be used to improve the resistance of the graphene electrode by p-type doping. As the work function of Au (5.1 eV) is larger than that of pristine graphene (4.5 eV), the electrons are transferred from graphene to Au^+ during the doping process, resulting in the downward shift of the Fermi level below the Dirac point.[139] Owing to the p-type $AuCl_3$ doping, the work function monotonically increased from 4.52 to 4.86 eV with the increasing concentration of $AuCl_3$.[101] The $AuCl_3$-doped graphene anode showed an improved sheet resistance ($\sim$70 Ω cm^{-2}) compared to pristine transparent graphene conducting electrodes ($\sim$890 Ω cm^{-2}).[101] p-Type doping aims primarily to reduce the sheet resistance of the graphene anode. While the extensive work on graphene anodes has proven fruitful with respect to device performance and stability, the graphene cathode in PSCs is rarely reported due to the large work function of graphene. n-Type doping is an efficient method to decrease the work function and sheet resistance of the graphene cathode. Relevant studies have been reported in other photovoltaic applications apart from PSCs. The formation of n-type graphene can be rendered by doping with ethylene diamine, diethylene triamine, and triethylene tetramine containing two, three, and four amine groups, respectively.[140] As the number of amine groups is increased, the sheet resistance of the doped graphene was reduced from $\sim$700 Ω sq^{-1} to $\sim$205 Ω sq^{-1} with a corresponding decrease in transmittance of only 1%. The work function was gradually reduced from $\sim$4.60 eV to $\sim$4.46 eV.[140] n-Type graphene doped with (4-(1,3-dimethyl-2,3-dihydro-1*H*-benzoimidazol-2-yl)phenyl)-dimethylamine was employed as a cathode in inverted polymer light-emitting diodes.[141] Such n-doping reduced the work function of graphene by $\sim$0.45 eV without significant reduction of optical transmittance.[141] The sheet resistance of graphene was reduced by $\sim$35% after n-type doping.[141] On the basis of these studies, to achieve highly conductive graphene anodes and cathodes for high performance PSCs, greater effort must be dedicated to the development of additional favorable hole and electron dopants.

3.2 Effect of two dimensional material-based electron transporting layers on the carrier dynamics and performance of perovskite solar cells

The ETL is one of the most important components in high-performance PSCs. It extracts photo-generated electrons from

the perovskite active layer and transports these charges to the electrodes. Simultaneously, the ETL serves as a hole blocking layer to suppress charge recombination.[142] Ideally, ETLs should efficiently transport electrons to minimize the series resistance of PSC devices. Optimizing the characteristics of the ETL, especially the charge mobility, morphology, energy level alignment, and related interfacial properties, is essential for high-performance PSCs.[142] It has been reported that the work functions of TDMs are tunable, and the electrical conductivity is easily adjusted through functionalization and specific treatment methods.[143–145] Owing to their useful processing–property relationship, TDMs are highly promising alternatives to traditional ETL materials in PSCs.

3.2.1 Electron extraction and transport efficiency of graphene derivatives and their effect on device performance. Since monolayer graphene was first successfully fabricated by Novoselov *et al.* in 2004, the electrical and optical properties of graphene have been significantly enhanced.[146] Being an ambipolar material capable of efficient transport of both holes and electrons, reduced graphene oxide (rGO) and other solution processable graphene derivatives with tunable energy levels (by functionalization) exhibit remarkably high carrier mobility, a wide spectral absorption range, and high optical transparency.[145,147] Recently, graphene-based ETLs have found success in scalable fabrication processes by achieving optimized charge carrier dynamics compared to the conventional ETL materials.[109,148] Incorporation of graphene into the ETLs reduces the series resistance in solar cells, leading to an increase in overall device efficiency.[149]

3.2.1.1 Electron extraction and transport efficiency of graphene derivative/inorganic material composites and their effect on device performance. TiO_2 is widely used as an ETL in PSC devices. It has an electron mobility of approximately 1 $cm^2\ V^{-1}\ s^{-1}$ with a conduction band minimum of 4.2 eV *vs.* vacuum level.[150] However, pristine TiO_2 still has a relatively low electrical conductivity limiting its application as an ETL. To address this problem, graphene derivatives doped with metal oxides have been employed as ETLs for improving the electron extraction and transport efficiency. As graphene has a work function between that of the typical FTO cathode and the conduction band of the TiO_2 ETL, it may reduce the formation of energy barriers at the interfaces, thereby functioning as a mediator of electron transfer.[151] The mobility of a TiO_2 compact ETL after incorporating graphene can be improved from 0.7×10^{-3} $m^2\ V^{-1}\ s^{-1}$ to 6.3×10^{-3} $m^2\ V^{-1}\ s^{-1}$, more than 8 times that of the pure TiO_2 ETL.[152] The enhanced mobility improves electron transport and collection efficiency, leading to improved device performance (15.4% with graphene and 11.2% without graphene).[152] The high mobility of the ETL reduces its resistivity as well as the series resistance of PSC devices. In the case of rGO/TiO_2 nanocomposite films, the resistivity was reduced from 3.03×10^5 Ω cm to 4.94×10^4 Ω cm after adding rGO into TiO_2. A decrease in the series resistance from 10.1 Ω cm^{-2} to 4 Ω cm^{-2} was also observed when incorporating graphene flakes with a TiO_2 ETL in PSCs.[103] This suggests an increase in the conductivity and a reduction in the contact resistance. To further improve the electron dynamics of graphene (G)/TiO_2 ETLs in PSCs, a lithium-neutralized graphene oxide (GO-Li) interlayer between the ETL and perovskite layers was added (Fig. 10). The carrier extraction efficiency of the ETL composites increased by a factor of one and two, respectively, relative to devices using graphene/TiO_2 and standard TiO_2 ETLs.[109] In addition, the ETL composed of G + $mTiO_2$ + GO-Li significantly improved the crystallinity of the $MAPbI_3$ active layer with a trap density about one order of magnitude lower.[109] Consequently, J_{sc} was enhanced significantly from 19.7 to 22.8 mA cm^{-2}.

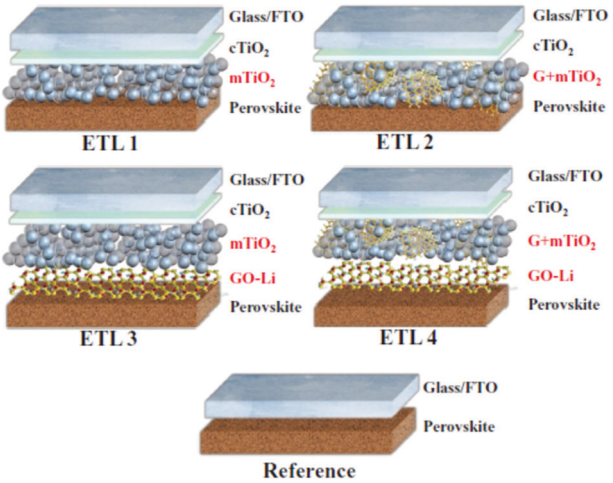

Fig. 10 Layer structures of the investigated samples. The ETLs are indicated in red. ETL 1: $mTiO_2$, ETL 2: G + $mTiO_2$, ETL 3: $mTiO_2$ + GO-Li, ETL 4: G + $mTiO_2$ + GO-Li, reference sample: no ETL. Reproduced from ref. 109 with permission from John Wiley and Sons, copyright 2017.

Although incorporation of graphene into ETLs does improve the carrier dynamics of devices with a TiO_2 ETL, TiO_2-based PSCs degrade rapidly when exposed to UV light. Such devices also typically require a high-temperature sintering process to achieve TiO_2 crystallization, thus restricting the fabrication of PSCs on flexible substrates.[153] ZnO has a band structure similar to that of TiO_2 (approximately −3.6 to −4.4 eV below the vacuum level for the conduction band and −7 to −7.5 eV for the valence band).[154] However, the electron mobility of ZnO is 200 $cm^2\ V^{-1}\ s^{-1}$, two orders of magnitude higher than that of TiO_2.[150] In addition, a sintering process is not necessary to achieve highly crystalline ZnO. The use of graphene ETLs in ZnO-based PSC devices may be viable for enhancing electron extraction and transport. It has been reported that the addition of GO into ZnO ETLs lowered the series resistance of PSCs by 75% due to the higher electron mobility and lower resistivity for the ZnO–GO nanocomposite (6.7×10^{-3} Ω m *vs.* 1.9×10^2 Ω m for the pristine ZnO ETL).[149] With a ZnO–GO nanoparticle ETL, electron transport was increased due to improved conductivity. The interfacial resistance between the graphene/ZnO ETL and the perovskite film was reduced, thereby enhancing charge extraction efficiency.[77] In contrast, pristine ZnO ETL-based PSCs typically exhibited low efficiencies due to low temperature annealing during the formation of perovskite crystals. High temperature (>70 °C) can lead to a chemical reaction between

the perovskite absorber and ZnO.[155] Thus, the grain size of the perovskite in pristine ZnO ETL-based PSCs is usually small. The insertion of graphene between the ZnO ETL and perovskite absorber can prevent such interactions. The annealing temperature can increase up to 150 °C, resulting in larger perovskite grains.[155] Moreover, the addition of graphene can decrease the root mean square roughness of the perovskite film due to the easier infiltration of perovskite precursors into the surface of the graphene/ZnO ETL.[77] As a result, the interfacial modification of ZnO with graphene leads to a significant increase in the J_{sc} and PCE because of the enhanced charge extraction and transport efficiency as well as the improved perovskite film.[77] In addition to the improvement of efficiency, graphene can also improve the stability of PSCs due to its hydrophobic nature. A graphene–SnO_2 ETL-based PSC retained ~90% performance after aging in ambient conditions with a relative humidity of 40 ± 5% for 300 h.[156]

In contrast to widely studied binary oxides, ternary oxides used in ETLs are rarely reported. $SrTiO_3$ (E_g is 3.25 eV with a conduction band of −3.65 eV below the vacuum level and a valence band of −6.9 eV) has a band gap similar to that of TiO_2,[157] but its band structure is more compatible with $MAPbI_3$ whose valence band and conduction band are −3.88 eV and −5.43 eV, respectively.[158] The electron mobility of $SrTiO_3$ at room temperature is 5–8 $cm^2\ V\ s^{-1}$, a value larger than that of TiO_2. Furthermore, its high dielectric constant is helpful for increasing the charge lifetime and suppressing trap-assisted recombination at the interface due to the small electron–hole binding energy.[159] The crystallization of $MAPbI_3$ grown on a $SrTiO_3$ ETL is improved when compared to $MAPbI_3$ grown on a pristine TiO_2 layer due to the similar crystal structure shared by $MAPbI_3$ and $SrTiO_3$.[104] The use of pristine $SrTiO_3$ as the ETL in PSCs led to a high V_{OC} but low J_{sc} due to low electron extraction and transport efficiency.[104] Graphene can be introduced into the ETL to improve the electron dynamics due to the high charge mobility and electronic conductivity. Graphene/$SrTiO_3$ nanocomposites as the ETL improved the J_{sc} of devices from 12.42 to 18.08 mA cm^{-2} after loading with graphene.[104] With a PCE of 10%, this is the highest reported efficiency for $SrTiO_3$-based PSCs.[104]

3.2.1.2 Electron extraction and transport efficiency of graphene derivative/organic material composites and their effect on device performance. Organic semiconductors are highly desirable as ETLs in PSC devices because of their low temperature fabrication, suitable energy level alignment, and decent electron mobility.[142] Pinhole-free films of organic semiconductors (*e.g.*, fullerene,[160] graphene,[103] and ionic liquids[161]) are typically applied in an inverted p-i-n configuration due to challenges associated with their depositions in a conventional n-i-p configuration.[153] Fullerene and its derivatives, such as [6,6]-phenyl-C_{61}-butyric acid methyl ester ($PC_{61}BM$), indene-C_{60} bisadduct (ICBA) and [6,6]-phenyl-C_{71}-butyric acid methyl ester ($PC_{71}BM$), are the most widely used n-type materials for ETLs in inverted PSCs due to their efficient electron extraction.[142] The conductivity of $PC_{61}BM$ (0.109 ± 0.005 mS cm^{-1}) is significantly increased after the incorporation of rGO as the ETLs in PSCs compared to that without rGO (0.495 ± 0.001 mS cm^{-1}). Thus, the photogenerated charge carriers in the perovskite are more efficiently transported to the rGO:$PC_{61}BM$ electron conductor than to the pristine $PC_{61}BM$, leading to higher J_{sc} and FF values.[160] The rGO additive functions as a bridge for charge injection from the perovskite to the $PC_{61}BM$ ETL. And also, rGO stabilizes the $PC_{61}BM$/perovskite interface with a suppressed degradation rate, making the PSC devices stable under continuous solar illumination.[160] The perovskite film becomes smoother when it is coated with the rGO:PCBM ETL compared to that coated with the pure PCBM ETL.[160] The traps on the perovskite surface are reduced and passivated, thereby resulting in a higher V_{OC}.[160] The architecture of the fabricated planar inverted rGO:$PC_{61}BM$ ETL-based PSCs is shown in Fig. 11a. The device exhibited an average hysteresis-free PCE of 14.5%. This value was larger than that of pristine PCBM-based devices at 12.9% (Fig. 11b and c) due to the enhanced rate of carrier extraction and transport at the rGO:PCBM/perovskite interface (Fig. 11d) as well as improved perovskite films.[160]

Due to their high electron mobility, graphene derivatives are promising alternatives to incorporate with inorganic and organic electron conductors such as TiO_2 and PCBM, respectively, as composite ETLs in PSCs. They can not only enhance the electron extraction and transport efficiency but also improve the crystal size and film morphology of the perovskite.

However, the insertion of these graphene derivatives inevitably decreases the transmittance of devices. The graphene derivatives, such as rGO, can absorb light in the wavelength range of 200–800 nm. The light absorption by the perovskite absorber is reduced with the increase in the density of graphene derivatives, which can reduce the amount of photo-generated carriers and eventually decrease the photocurrent density.[106] In addition, the dimension of the graphene derivatives prepared is usually much larger than the thickness of the perovskite. There is unavoidable direct contact between graphene derivatives and perovskites. Thus, conductive graphene derivatives create new recombination centers inducing lower photocurrent and fill factor.[103,104] In order to achieve high performance PSCs, it is critical to find a good balance between the transmittance, carrier extraction and conductivity of graphene derivative-based ETLs.

3.2.2 Electron extraction and transport efficiency of graphdiyne-based composites and their effect on device performance. The success of graphene-based ETLs in PSC devices has encouraged the development of ETLs based on other TDMs. However, highly conductive graphene has no energy band gap, limiting its application in semiconductor fields.[162] In addition, it is generally difficult to control the functionalization of pure sp^2-carbon materials such as graphene because of their tendency to aggregate.[163] Graphdiyne (GD), a novel kind of 2D carbon allotrope composed of sp- and sp^2-hybridized carbon atoms forming a network of delocalized π electrons, possesses characteristics similar to that of graphene but with the added benefit of easier functionalization due to improved dispersion.[164] First principle calculations have shown that graphdiyne possesses a natural band-gap in contrast with graphene whose band-gap is zero. Owing to these superior properties, GD is an attractive candidate for use as an ETL in PSCs.

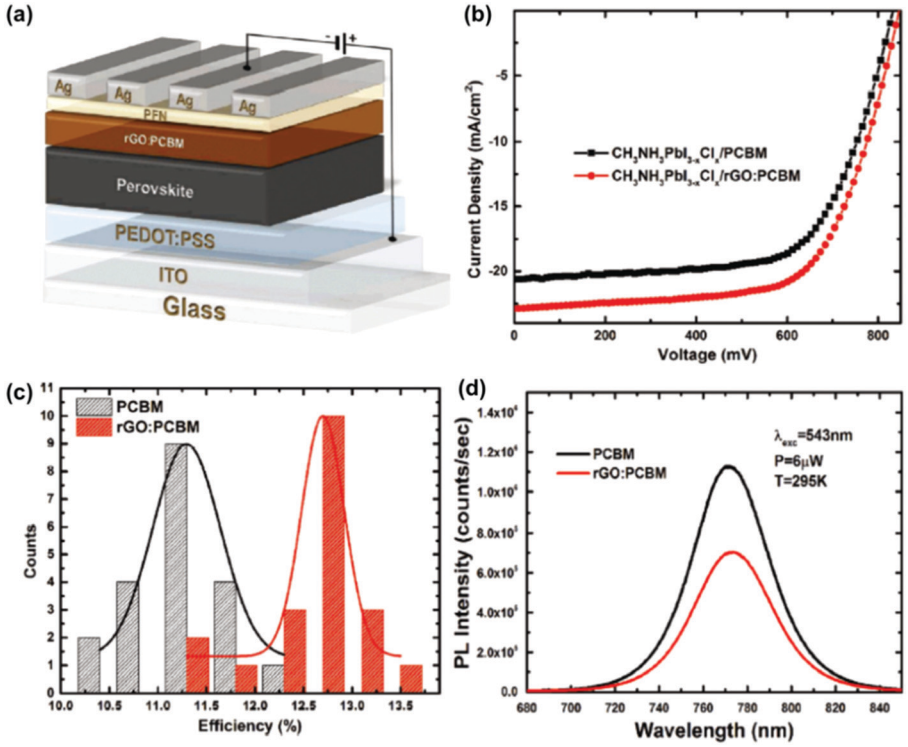

Fig. 11 (a) Schematic of the layered structure of a fabricated planar inverted PSC. (b) The *J*–*V* curves of PSCs containing a 5% rGO-doped PCBM ETL and pure PCBM ETL. (c) PCE distribution of devices with and without rGO in the PCBM ETL. (d) Photoluminescence (PL) spectra (excitation at 543 nm) of $CH_3NH_3PbI_{3-x}Cl_x$/PCBM and rGO:PCBM/glass substrates. Reproduced from ref. 160 with permission from John Wiley and Sons, copyright 2016.

As mentioned above, PCBM is the most widely used ETL material in p-i-n type planar PSCs. However, pristine PCBM-based PSC devices show unsatisfactory photovoltaic performance due to the low coverage area of pristine PCBM ETLs on the perovskite layer, leakage currents, and interfacial charge recombination.[165,166] In 2015, an ETL composed of PCBM doped with GD was first employed in a planar heterojunction PSC device with an inverted structure (*i.e.*, ITO/PEDOT:PSS/$CH_3NH_3PbI_{3-x}Cl_x$/PCBM:graphdiyne/C_{60}/Al).[23] The device architecture of the PSC is shown in Fig. 12a. Based on the c-AFM measurements, the PCBM:GD film showed significantly increased vertical current, suggesting that the electrical conductivity of PCBM:GD increases upon GD doping.[23] The electron mobility of the PCBM:GD based electron-only device increased from 2.98×10^{-4} cm^2 $(V\ s)^{-1}$ to 5.32×10^{-4} cm^2 $(V\ s)^{-1}$.[23] A significant quenching effect of PL was observed when the perovskite layer was coated with the PCBM:GD ETL.[23,113] The GD doping enhanced electron transport from the perovskite to PCBM and reduced the electron accumulation that usually occurs at the interlayer of perovskite devices due to the relatively strong π–π stacking interaction between GD and PCBM.[113] Moreover, the perovskite layer coated with the PCBM:GD film became smoother than that coated with the pure PCBM film. The grain-boundary of the perovskite was passivated after the addition of GD, thereby reducing the trap states of the perovskite surface and suppressing carrier recombination.[23,113] The introduction of GD led to improved performance with the PCE increasing from 13.5 to 14.8% and the J_{sc} increasing from 22.3 to 23.4 mA cm^{-2} (Fig. 12b).[23] A steady-state PCE was obtained, as shown in Fig. 12c. The enhanced performance can be attributed to the improved electrical conductivity, strong electron mobility, efficient charge extraction and transport, and improved coverage area of the PCBM:GD ETL on the perovskite layer.[23] GD has also been integrated into a solution-processable cross-linked fullerene [6,6]-phenyl-C_{61}-butyric styryl dendron ester (PCBSD) ETL.[112] The structure of the perovskite planar heterojunction solar cells is shown in Fig. 13. After GD doping, face-on stacked PCBSD molecules were assembled due to the π–π stacking interaction between GD and cross-linkable PCBSD. This orientation is favorable for the growth and crystallization of subsequent perovskite films. The cross-linkable PCBSD–graphdiyne composite ETL demonstrated superior electron mobility, energy-level tailoring, and efficient charge extraction. Consequently, these PSCs attained a maximum PCE of 20.19% with improved cell stability in air (dark).[112] When ZnO replaces the organic electron transporters such as PCBM and PCBSD as ETLs in PSCs, it was found that the doping of GD increases the electrical conductivity and the electron mobility of ZnO and improves perovskite film morphology.[111] Doping GD passivates the traps in organic and inorganic ETLs such as PCBM and ZnO films, respectively, thus suppressing carrier recombination at the interface of PSCs and consequently reducing the *J*–*V* hysteresis and improving FF.[23,113]

Thus, we conclude that GD is a cost-effective and superior alternative to prevalent carbon materials such as graphene and carbon nanotubes for several applications in photovoltaics. Due to its excellent intrinsic electrical properties, it can greatly

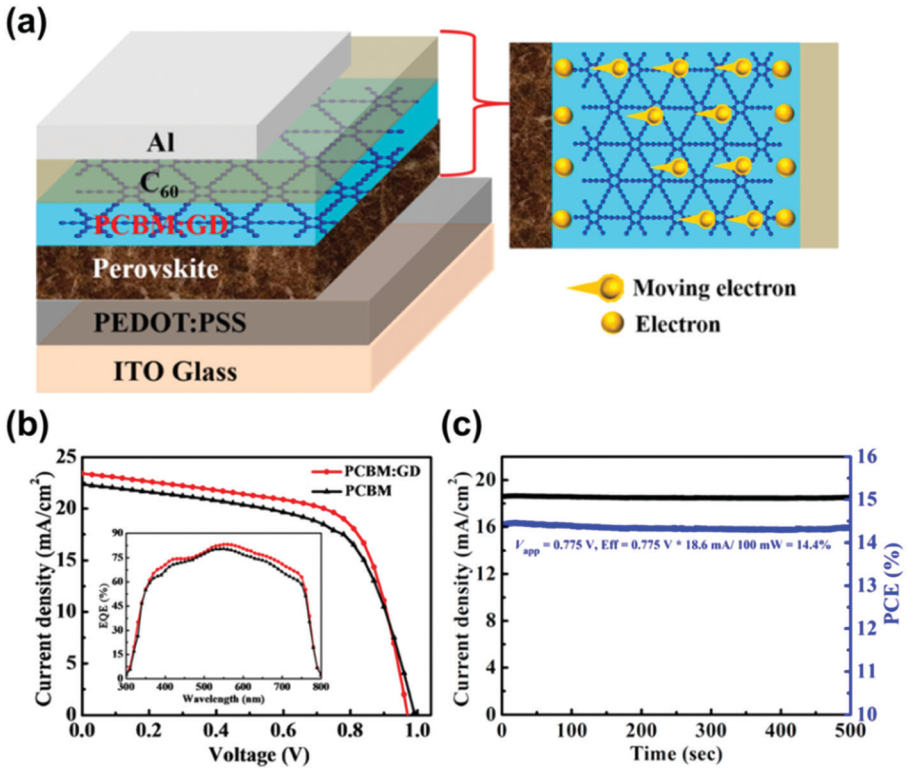

Fig. 12 (a) Layer structure of a PSC device with graphdiyne; (b) *J*–*V* curves of pure PCBM and PCBM:GD based PSCs (the inset shows the corresponding EQE spectra of the devices); (c) steady-state efficiency (blue) with the J_{sc} (black) of the PCBM:GD based PSC. Reproduced from ref. 23 with permission from American Chemical Society, copyright 2015.

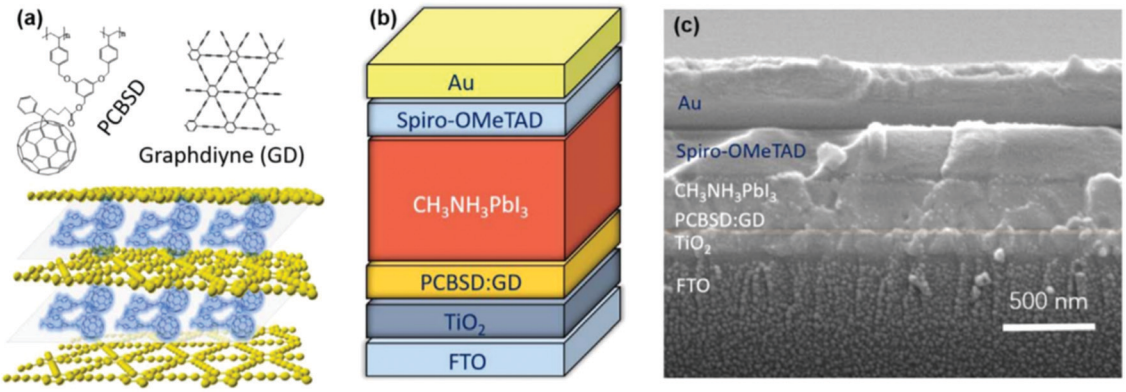

Fig. 13 (a) Chemical structure of PCBSD and GD, and schematic illustration of the face-on stacked cross-linkable PCBSD (C-PCBSD) film. (b) Structure of planar heterojunction PSC devices. (c) Cross-section SEM image of a typical PSC with a C-PCBSD:GD based ETL. Reproduced from ref. 112 with permission from Elsevier, copyright 2017.

enhance electron extraction and transport when combined with traditional ETL materials such as ZnO and PCBM in PSCs, bridging the gaps at interfaces by providing good electrical contact and low interfacial resistance. GD can passivate the grain boundaries of perovskite films and reduce the trap states on the surface to eliminate carrier recombination. Despite these advantages, the study on GD-based ETLs is still in its infancy. The large scale fabrication of high-quality and defect-free ultrathin GD still remains challenging which limits its application in PSCs. Moreover, the studies on chemical functionalization of GD with other elements or functional materials are needed to produce the desired bandgap structure.

3.2.3 Electron extraction and transport efficiency of two-dimensional metal oxides and their effect on device performance. Two-dimensional (2D) metal oxide nanosheets can enhance the electrical contact at the perovskite interface to facilitate electron extraction and transport.[44] They can provide direct pathways for electron transport, shortened pathways for carrier diffusion, and high specific surface area offering more transport channels. The interlayer spacing in 2D nanosheets is beneficial for the

intercalation of perovskite particles in bi-layer PSC configurations. Therefore, it is viable to use 2D metal oxides as ETLs in PSCs. To date, several 2D metal oxides have been used in ETLs for PSCs including SnO_2 nanosheets,[43,44] TiO_2 nanosheets,[45,46] WO_3 nanosheets,[47] and ZnO nanosheets.[48] Current research on 2D metal oxide-based ETLs remains sparse. TiO_2 nanosheet ETLs containing high levels of exposed (001) facets were reported in a hole-conductor-free mesoscopic TiO_2/$MAPbI_3$ heterojunction solar cell device, as shown in Fig. 14a.[45] Owing to the high ionic charge concentration of the (001) facets in the TiO_2 nanosheet, the attachment of the perovskite onto the TiO_2 surface is stronger than that to the nanoparticle layer. This stronger anchoring further facilitates electron injection from the perovskite layer into the TiO_2 ETL, resulting in improved device performance.[167] When employing ZnO nanosheets as ETLs in $MAPbI_3$ PSCs (Fig. 14b),[48] 2D ZnO nanosheets increased electron transfer leading to an improvement in PCE comparable to that of PSCs based on ZnO nanoparticles.[48] This improvement is also attributed to the increased interfacial contact between the ZnO nanosheet and the perovskite layer. In addition, the PbI_2 could form on the ZnO nanosheet surfaces due to the alkaline behavior, leading to reduced charge recombination and improved electron collection at the interface of ZnO and perovskite.[168] A type I band alignment between PbI_2 and perovskite forms energy barriers to prevent excitons from the surface defects and trap states.[168] Thus, a carrier transport route with less non-radiative channels is presented in the film. The self-induced conversion of PbI_2 effectively passivates the grain locally, resulting in a high quality perovskite film.[168] It has been demonstrated that 2D metal oxide based ETLs are superior to other types of metal oxide nanostructures in PSCs.[47] The PSC devices using WO_3 nanosheet arrays as ETLs showed enhanced photovoltaic performance (PCE = 11.24%) compared to devices using one-dimensional nanorods (PCE = 9.10%) and zero-dimensional nanoparticles (PCE = 6.08%) as ETLs. Single crystalline growth of monoclinic WO_3 nanosheets with dominant facet (002) occurred perpendicular to the substrate surface. Such highly oriented crystals improve the diffusion of electrons for longer distance diffusion and enhance the charge transport.[47] Also, optimized perovskite absorber infiltration in the porous scaffold of WO_3 nanoseheets is achieved, which may be an additional main cause of enhanced photovoltaic performance as compared to nanoparticles and nanorod arrays. In addition to enhancing electron extraction and transport efficiency, 2D metal oxide ETLs can also improve the stability of PSCs. A hierarchical ETL containing a thin compact SnO_2 layer and a mesoporous layer of 2D SnO_2 nanosheets was reported which provides efficient electron diffusion from SnO_2 to the perovskite for enhanced electron collection.[43] This hierarchical SnO_2 layer can protect the perovskite layer from moisture in the air, leading to improved device lifetime. It was found that almost no change occurs for the perovskite/SnO_2

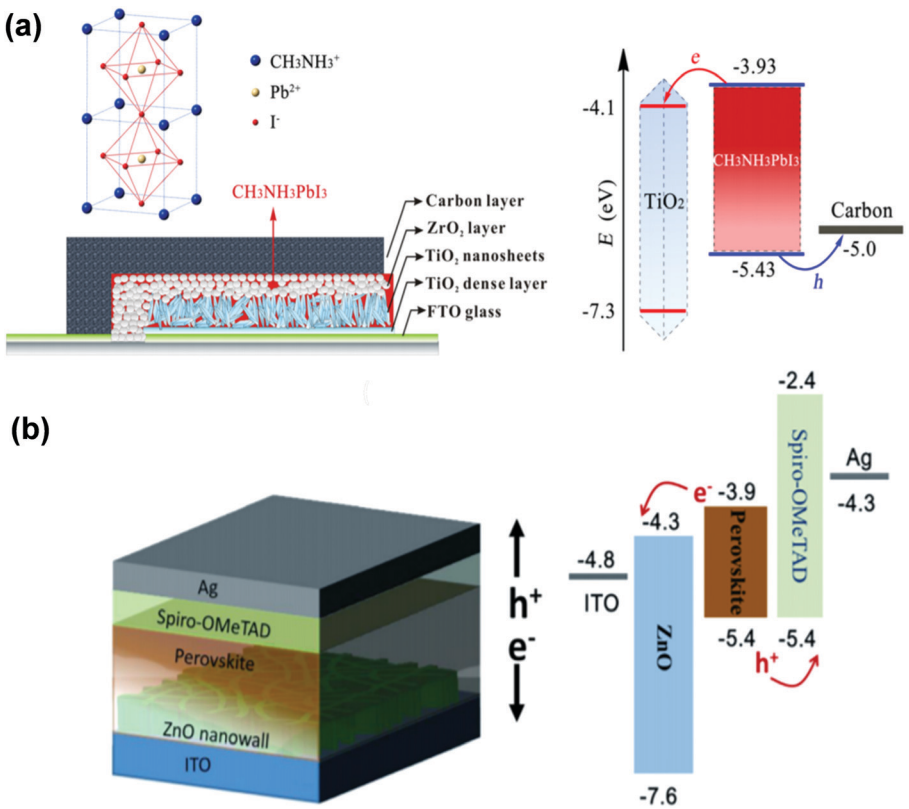

Fig. 14 (a) Schematic and energy level diagram of a PSC based on an anatase TiO_2 nanosheet ETL and carbon counter electrodes. Reproduced from ref. 45 with permission from American Chemical Society, copyright 2014. (b) Device structure and energy band diagram of the ZnO nanosheet ETL-based device. Reproduced from ref. 48 with permission from Elsevier, copyright 2016.

ETL after 1500 h under 20% humidity. Even after pushing to the limit by testing for 10 h under 95% humidity, virtually no change was observed. Consequently, 90% of the initial device efficiency (16.17%) was retained after storage in an ambient atmosphere for 130 days without encapsulation.[43]

Therefore, 2D nanosheet arrays of metal oxides as ETLs open up new opportunities in the development of highly efficient perovskite solar cells. They can be vertically aligned with respect to the substrate surface in PSC devices and present an open structure which favors rapid electron extraction and transport as well as excellent perovskite infiltration to form a high quality perovskite film. The nanosheet ETLs can improve the stability of PSC devices by protecting the perovskite layer from moisture. Nevertheless, there is still a lack of sufficient understanding of the intrinsic relationship between the ETL nanostructures and their PSC performance. Controlled synthesis is of great importance for improving the performance and understanding the intrinsic mechanisms. The morphology, optical and electronic properties, band structures and charge transfer processes can be designed *via* controlled synthesis. Density functional theory calculations can be adopted as an effective method to simulate the electronic structures of these metal oxide nanostructures, rendering purposeful design of PSC devices.

3.3 Effect of two dimensional material-based hole transporting layers on the carrier dynamics and performance of perovskite solar cells

In addition to the ETL, the HTL is another important layer whose development can significantly improve the PCE and stability of PSCs. The ideal HTL should have an appropriate work function to ensure an ohmic contact with the donor material and the ability to exclusively extract holes effectively from a light absorber (such as $MAPbI_3$) and quickly transport them to the electrodes. Furthermore, the reliability and chemical compatibility of HTLs should also be taken into account to guarantee the long-term stability of PSC devices. Spiro-OMeTAD (2,2′,7,7′-tetrakis-(*N*,*N*-di-4-methoxyphenylamino)-9,9′-spirobifluorene) and PEDOT:PSS are widely used as HTLs in n-i-p- and p-i-n-type PSCs, respectively. However, the stability of these materials is uncertain.[169] They are sensitive to oxygen and even more sensitive to moisture than their inorganic counterparts.[170] Attempts to substitute them with other HTL materials have been made. Some of the alternatives that have been realized include organic phthalocyanines[171] and inorganic copper(I) iodide.[172] Traditional TDMs, such as graphene and its derivatives, have suitable work functions and good film-forming properties, which make them useful as efficient HTLs.[173] With the various strategies developed for improving graphene-based material properties in PSCs, several highly efficient and stable PSCs have been reported using graphene-based HTLs. The details of graphene-based HTLs are reviewed in the following section.

3.3.1 Hole extraction and transport efficiency of graphene derivatives and their effect on device performance. In 2014, Sun *et al.* first reported the use of graphene oxide (GO) as a HTL in an inverted planar heterojunction PSC with $CH_3NH_3PbI_{3-x}Cl_x$ as the active layer (Fig. 15a).[174] GO was applied as an HTL due to its suitable work function ($\sim$4.9 eV) and acceptable vertical resistivity which is an order of magnitude lower ($\sim 10^3$–10^4 Ω cm) than the lateral resistivity.[173] Holes can be easily extracted and transported *via* the sp^2 clusters of GO. The sp^2 clusters are isolated laterally but are in contact with the electrodes. In addition, GO can dope the surface of active layers.[175] The presence of carboxylic acid and phenolic and enolic groups in GO leads to a high proton density of one exchangeable proton per 8.7 carbon rings,[175] resulting in the p-type doping of the active absorber and high conductivity at the interfaces. The increased proton mobility can be attributed to the stabilized negative charge on the surface oxygen because of the delocalization of the 2p electrons of functional oxygen into the π-conjugated system.[176] When a thin GO layer was deposited onto a P3HT HTL, the electrical conductivity of P3HT increased by six orders of magnitude to reach as high as 3.70 S m^{-1} with a metallic-like characteristic.[175] Charge transfer absorption peaks in near infrared regions were observed due to the increase in conductivity.[175] Thus, the GO layer can efficiently extract and transport the photo-generated holes from the $CH_3NH_3PbI_{3-x}Cl_x$ perovskite active layer to the electrode resulting in GO HTL-based PSC devices with efficiencies of over 12%.[174] In addition, the perovskite film grown on GO exhibited enhanced crystallization with preferred orientation of the (110) plane, leading to more carriers generated in the perovskite layer.[174] Based on these results, researchers have further optimized the fabrication process. A balance of high work function and conductivity was achieved by controlling the thickness of the GO layer.[24] By optimizing the thickness of GO, GO HTL-based PSCs can achieve a PCE as high as 16.5% with no hysteresis (Fig. 15b). The devices exhibited better hole extraction efficiency due to the higher work function of GO (5.2 eV) than that of PEDOT:PSS (4.9 eV) as shown in Fig. 15c. Under high humidity and continuous light irradiation, the PSC devices retained $>80\%$ of their initial efficiency after 2000 h. This performance was better than that of the reference device using a PEDOT:PSS HTL.[24] The performance improvement is due to the enhanced charge extraction efficiency stemming from the better alignment of band energies and higher optical absorption due to a higher work function of GO and the larger grain size of the perovskite grown on the GO film. Mohammadi, Lianos *et al.* prepared GO-based PSCs with GO as the HTL, Li-modified GO as the ETL, and Al as the counter electrode in p-i-n type PSCs (Fig. 15d).[72] A maximum solar conversion efficiency of 10.2% was achieved.

Despite these achievements of GO HTLs, the photovoltaic performance of GO HTL-based PSCs remains low due to the insulating properties of GO and the high degree of oxygen contents such as –C–O–C, –C–OH, and –C–COOH on the surface. Holes are efficiently extracted from the perovskite to GO but also trapped on the localized oxygen atoms of GO, leading to electron–hole recombination at the interfaces. rGO is a carbon material which is formed by eliminating a significant fraction of the oxygenated moieties in GO *via* reduction. rGO exhibits semi-metal characteristics with a work function of 4.9 eV, a hole conductivity of 0.05–4 S cm^{-1}, and a hole mobility of 2–200 $cm^2\ V^{-1}\ s^{-1}$, with the last parameter being higher than that of GO (0.25 $cm^2\ V^{-1}\ s^{-1}$), yet 2–4 orders of magnitude lower

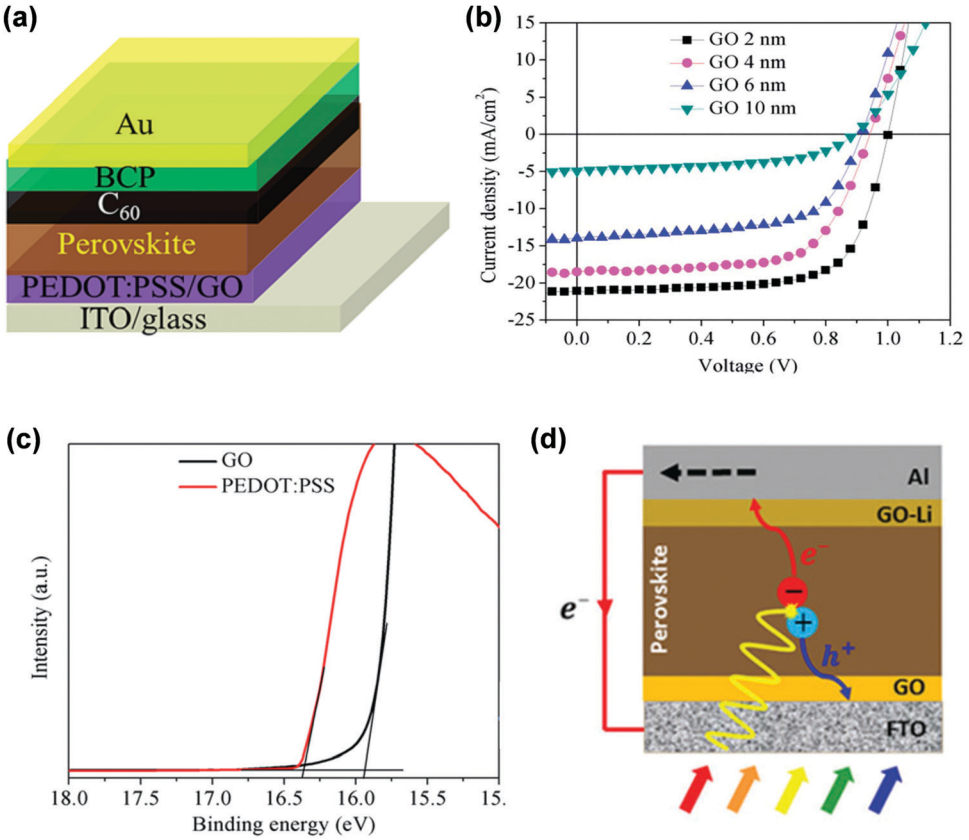

Fig. 15 (a) Device architecture of PSCs with PEDOT:PSS or GO as the HTL, (b) J–V curve of PSCs with different thicknesses of the GO layer, (c) UPS spectra of PEDOT:PSS and GO on an ITO substrate. Reproduced from ref. 24 with permission from The Royal Society of Chemistry, copyright 2017. (d) Schematic illustration of an inverted planar PSC with GO as the HTL and lithium-modified GO as the ETL. Reproduced from ref. 72 with permission from The Royal Society of Chemistry, copyright 2017.

than that of graphene due to the presence of residual groups and defects.[177] As oxygen-containing groups are reduced, the delocalized holes on the rGO ring can transport freely to the ITO substrate, leading to a larger photocurrent in the rGO device *versus* the GO device (Fig. 16a).[178] The contact angle of rGO becomes larger due to the decrease of oxygenated moieties, which induces lower surface energy. It has been verified that the low surface energy of a HTL in PSCs can suppress heterogeneous nucleation, facilitating the perovskite crystal grain growth and the formation of a uniform perovskite film.[179] An average grain size of $MAPbI_3$ on GO was 183 nm, while becoming over 200 nm with more centralized grain size distributions when the perovskite was coated on rGO.[180] A preferred (220) grain growth of $MAPbI_3$ was obtained when the perovskite was deposited on rGO which was not observed for deposition on ITO or GO.[180] The (220) crystallographic plane has small surface energy and interfacial energy, which can reduce recombination in the bulk or at interfaces.[181] The hole trap density was calculated to be 7.72×10^{15} cm^{-3} and 5.99×10^{15} cm^{-3} for perovskites on GO and rGO, respectively.[180] The decrease in trap density can enhance V_{OC} by improving the extraction efficiency of holes at the interfaces of HTLs and perovskites. It is important to note that rGO HTL-based PSCs showed improved stability not only under illumination but also during bending tests. Carlo *et al.* demonstrated mesoscopic PSCs using rGO as a HTL (Fig. 16b).[182] Although the PCE was 40% lower than that of Spiro-OMeTAD-based devices due to the smaller J_{sc}, the rGO-based PSCs retained a PCE of 6.6% after testing for 1987 h, an improvement over conventional devices using a Spiro-OMeTAD HTL (PCE = 6.5%). After a 120 h light endurance test, the rGO-based PSC retained 26% of its pristine PCE whereas the Spiro-OMeTAD-based PSC retained roughly 10% of its pristine PCE.[182] The improved stability of rGO-based PSCs in comparison to the Spiro-OMeTAD counterpart is because some additives (*i.e.*, 4-TBP) corrode the perovskite layer. Fortunately, these additives are not necessary in rGO HTLs.[183] A flexible device with a rGO HTL on an ITO/polyethylene 2,6-naphthalate substrate showed a PCE 13.8% and retained 70% of the original performance after continuous bending for more than 150 cycles,[178] demonstrating the good bending durability of rGO due to its excellent flexibility.

One major challenge of using graphene derivatives such as GO and rGO nanosheets as HTLs in PSCs is that they generally do not completely cover the ITO surface when applied by spin coating due to their 2D nanosheet structure and minimal interaction with the ITO surface.[173,184] It has been demonstrated that the quality of the carbon nanosheet film is strongly related to the amount of hydrophilic groups on its surface.

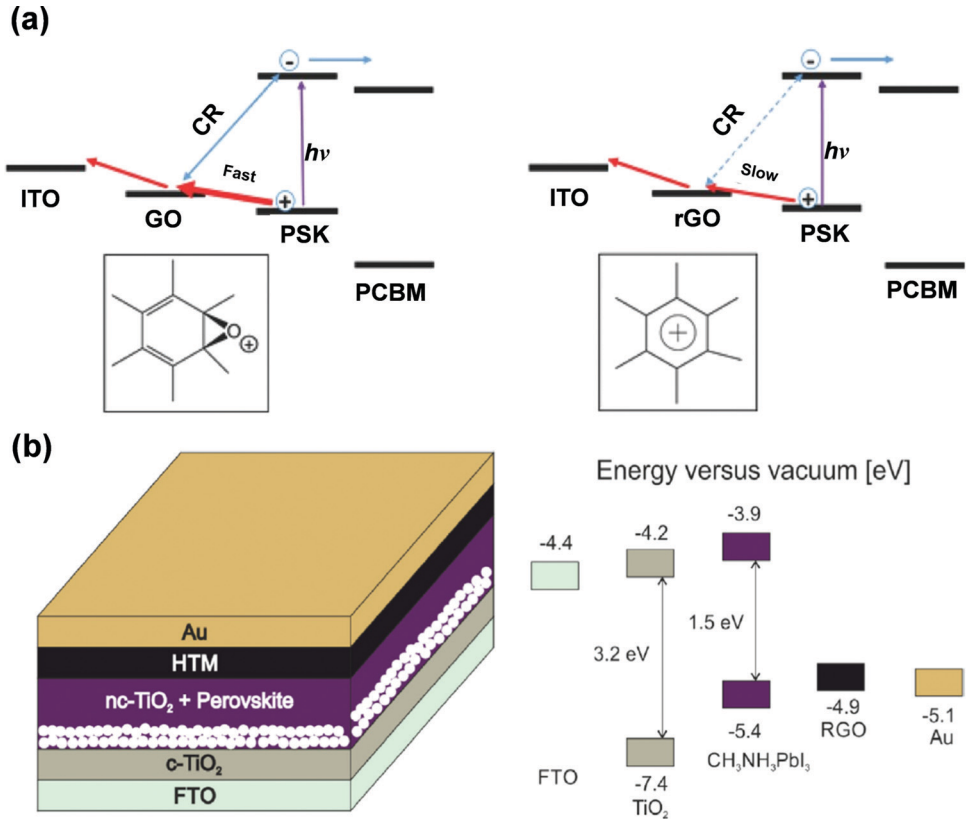

Fig. 16 (a) Diagram of the charge recombination (CR) and transfer mechanism for GO and rGO used to rationalize the observed hole extraction kinetics at the HTL/perovskite (PSK) interface. The boxes in the insets represent the localized holes on the oxygen atoms and the delocalized holes in the benzene ring of GO and rGO, respectively. Reproduced from ref. 178 with permission from John Wiley and Sons, copyright 2017. (b) Device architecture and energy band alignment of a PSC device containing a rGO HTL. Reproduced from ref. 182 with permission from Elsevier, copyright 2016.

These groups favor the formation of a stable nanosheet suspension during spin coating.[178] Compared to –BH groups, $–SO_3H$ and –NH– groups on the surface can produce a more stable nanosheet suspension with less aggregation, which facilitates the formation of a more uniform HTL film in PSCs.[178] Another problem is that the increased reduction time may decrease the work function of carbon nanosheets such as rGO due to the shift of the surface ionization potential,[180] increasing the mismatch of the energy band level between the perovskite and the HTL. This leads to an acceleration in radiative carrier recombination. In addition, the properties of the solvents for nanosheets are important in preventing corrosion of the perovskite layer as the spin coating of the nanosheets is carried out directly on the perovskite layer. The solvents with low boiling point, such as isopropyl alcohol and chlorobenzene, are required to permit their evaporation before reaching the substrates.[182] Thus, the high performance of graphene derivative HTL-based PSCs is highly dependent on the preparation procedure, which directly dictates the morphological, electrical and optical properties of the carbon nanosheets. Even though GO and rGO are promising hole extraction and transport materials, the reported results are still unclear as to which is more suitable as an HTL for PSC devices. The high proton density of GO facilitates the proton doping of the perovskite. The unique 2D structure of GO prevents it from penetrating into the bulk of the active absorber, making it an ideal material for surface doping to increase conductivity.[174] The existence of ample oxygen-containing functional groups attached to the tetrahedral-coordinated carbon atoms ($–C_{sp3}–O–C_{sp3}$, $–C_{sp3}–OH$, $–C_{sp3}–COOH$, *etc.*) may induce efficient hole extraction and transport.[178] However, the localized holes on oxygen atoms may increase the possibility for charge recombination at the HTL/perovskite interface.[183]In addition, the epoxy and hydroxyl groups, which disrupt the sp^2 conjugation of the graphene lattice, result in the insulating property of pristine GO which is detrimental for hole collection.[185,186] In contrast, when these oxygen-containing groups are reduced in rGO, the hole injection from the perovskite to the HTL occurs most likely at the C=C double bonds of the carbon rings in rGO, which can reduce hole injection at the interface. Further, the delocalized holes in the benzene rings of rGO retard charge recombination and improve performance.[178] Thus, there exist both advantages and disadvantages for each with respect to hole extraction and transport. Systematic investigations of these graphene derivatives are required to better understand their optoelectronic properties and to optimize their photovoltaic performance.

3.3.2 Hole extraction and transport efficiency of graphene derivative-based composites and their effect on device performance. Since pristine GO as an HTL in PSCs has some drawbacks such as its insulating properties and charge recombination induced by oxygen-containing groups, a composite of GO and PEDOT:PSS as the HTL is expected to compensate for the drawbacks of

pure GO.[116–118,120,187–190] A well-matched work-function between graphene oxide (4.9 eV) and PEDOT:PSS (5.1 eV) resulted in more efficient charge extraction and transport to the ITO electrode (4.7 eV) as well as an overall decrease in the series resistance (R_S) as shown in Fig. 17a and b.[117] GO suppresses carrier recombination, leading to an increase in shunt resistance (R_{Sh}).[117] When a conventional PEDOT:PSS HTL was doped with GO, the hole mobility increased from 5.55×10^{-5} to 1.57×10^{-4} cm^2 V^{-1} s^{-1}.[191] The GO/PEDOT:PSS HTL fabricated by sequential spin-coating of GO and PEDOT:PSS in a planar heterojunction PSC (Fig. 17c)[117] can reduce the impact of single component GO HTLs and conventional PEDOT:PSS HTLs. For example, the insulating properties of a pure GO HTL induced a low PCE of 6.4%, whereas a conventional PEDOT:PSS based PSC showed an improved PCE of 8.23%. In contrast, PSCs with a GO/PEDOT:PSS composite HTL exhibited a higher PCE of 9.7%.[117] Devices with GO exhibited relatively wide variations due to the low uniformity of GO caused by its 2D nanosheet nature and minimal interaction with the ITO surface, as noted in Section 3.2.1.[173,184] Large morphological deviations of the perovskite active layers occurred in p-i-n PSC devices. In contrast, GO/PEDOT:PSS based devices showed highly reproducible performance due to the optimized compatibility of the composite HTL with the ITO substrate. The long-term stability of such PSCs under atmospheric conditions was also improved when compared to a conventional PEDOT:PSS or pristine GO system. The PCE of PSCs fabricated with GO-modified PEDOT:PSS as a HTL retained 83.5% of their initial efficiency after aging for 39 days under 15% relative humidity.[187] GO prevented direct contact between ITO and the highly acidic PEDOT:PSS layer leading to improved stability. In addition, the $MAPbI_3$ films grown on GO/PEDOT:PSS were highly homogeneous and pin-hole free with large crystalline domains and a preferential in-plane orientation of the (110) plane, whereas the films on pristine GO HTLs exhibited pin-holes which may act as defects to induce severe degradation and reduction in the performance.[117] The superior wettability of the GO-modified PEDOT:PSS surface compared to pristine GO was observed

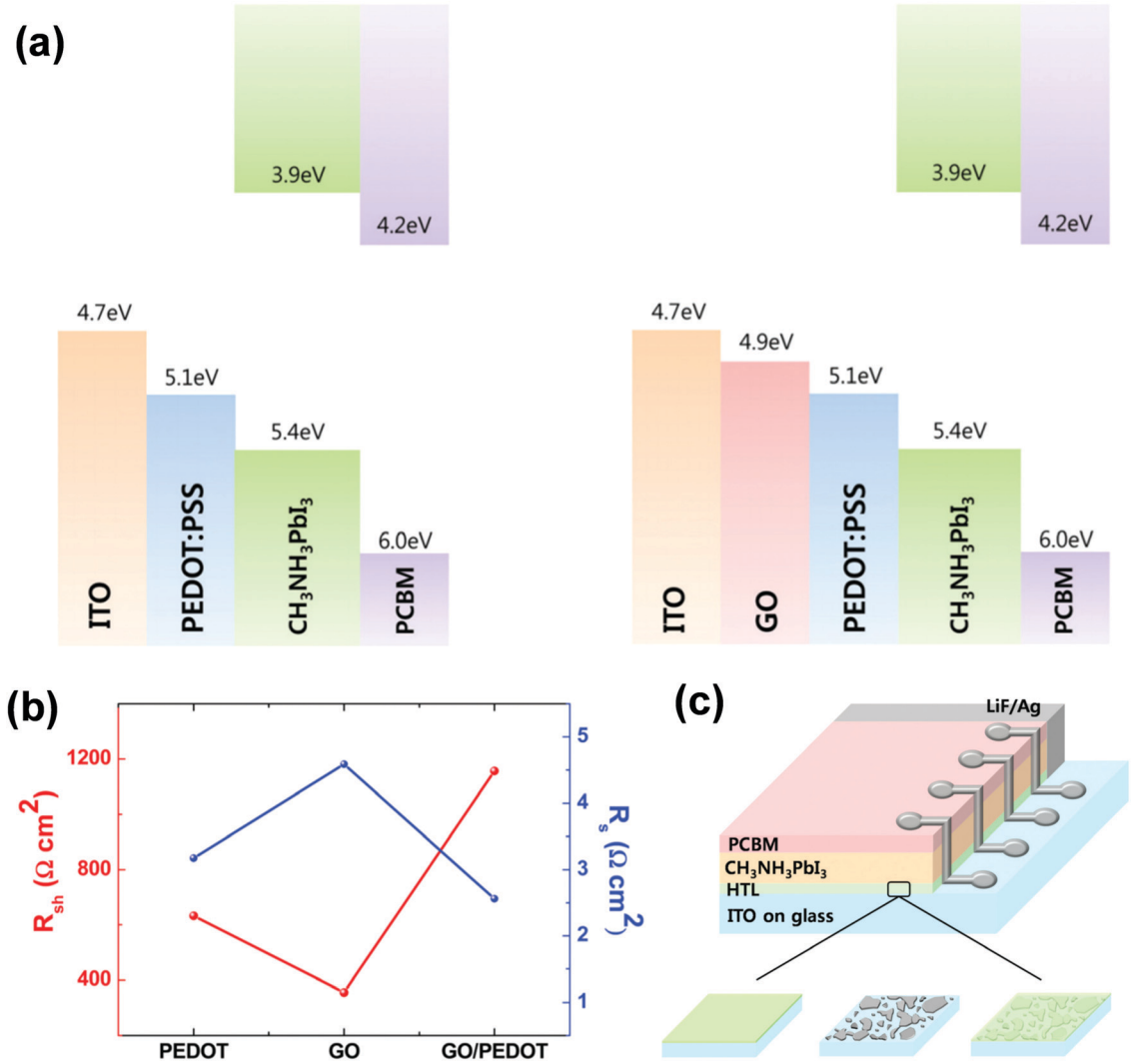

Fig. 17 (a) Schematic of energy levels for PSC architectures with PEDOT:PSS (left) and GO/PEDOT:PSS (right) HTLs, (b) R_{Sh} and R_S evaluated from J–V curves, and (c) the structure of the layered PSC device. Reproduced from ref. 117 with permission from The Royal Society of Chemistry, copyright 2015.

which may account for the formation of a high-quality perovskite layer with better crystallinity and reduced pin holes.[187] Another reason for the improved efficiency and stability of the GO/PEDOT:PSS-based devices is that the hygroscopic and low-conductive PSS at the PEDOT:PSS surface was partly removed during spin-coating with the GO solution, thereby improving the moisture resistance and decreasing the contact barrier between the GO/PEDOT:PSS HTL and the perovskite for enhanced hole-extraction.[192,193]

For the PEDOT:PSS HTL in PSCs, the poly(styrene sulfonate) (PSS) templates are generally dispersed in water, which can dissolve the underlying perovskite films.[194] Snaith *et al.* and Brabec *et al.* introduced a water-free toluene-dispersed PEDOT HTL into the PSCs, which demonstrated improved performance.[195,196] However, the relatively low performance of the PEDOT HTL-based PSCs remains an issue. The composite interfacial HTLs based on graphene derivatives have shown synergetic effects on charge-collection.[117,197] Yeo *et al.* first applied this strategy in the n-i-p PSCs with a double interlayer HTL consisting of water-free PEDOT and fluorinated reduced graphene oxide (FrGO) (Fig. 18a).[29] Different from rGO or GO which cannot completely cover substrates with the spin-coating method,[173,184] the FrGO layer can be uniformly deposited onto the PEDOT film *via* spin-coating due to the orthogonal solubility of PEDOT in 2-propanol, which is also used to disperse FrGO.[29] The PEDOT-FrGO HTL-based devices showed higher internal quantum efficiency with broader photo-response from 300 nm to 800 nm.[29] The resulting fluorinated surfaces of the HTL led to more hydrophobic surfaces and higher work functions of the HTL with the average work function enhanced by ~0.2 eV compared to the pristine PEDOT film. The change of the work function can be attributed to the reduced surface potential after incorporating FrGO in the HTL.

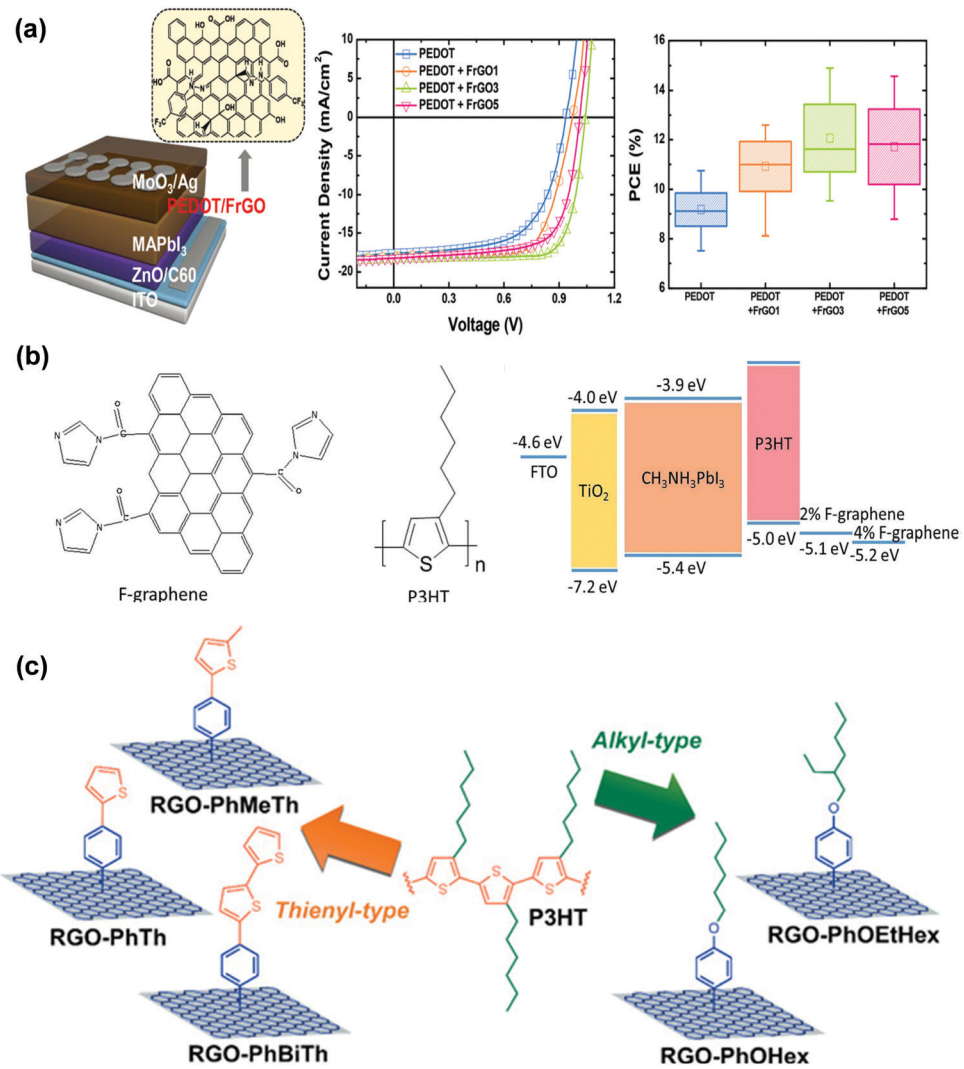

Fig. 18 (a) Schematic architecture of a PEDOT/FrGO HTL-based PSC, and the chemical structure of FrGO; *J*–*V* curves of PSCs with different HTLs, and the corresponding PCE data. Reproduced from ref. 29 with permission from The Royal Society of Chemistry, copyright 2017. (b) The chemical structures of F-graphene and P3HT and the corresponding schematic energy diagram of PSCs using different amounts of F-graphene. Reproduced from ref. 201 with permission from The Royal Society of Chemistry, copyright 2016. (c) Schematic illustration of five types of functionalized RGO species. Reproduced from ref. 202 with permission from John Wiley and Sons, copyright 2018.

The different surface potentials between PEDOT and FrGO induce interfacial dipoles at the PEDOT/FrGO interface pointing outward from FrGO.[198] Such dipoles can prevent undesirable recombination and accelerate hole transport by providing energy barriers and reinforcing the built-in potential across the device.[199,200] Thus, enhanced V_{OC} and FF were achieved.[29] The PEDOT-FrGO interlayer-based PSC exhibited a significantly improved PCE of 14.9%, a value larger than that measured for PEDOT HTL-based devices (PCE = 10.3%).[29]

The more hydrophobic surface of the PEDOT-FrGO HTL due to the graphitic 2-dimensional structure of FrGO induced enhanced device stability. Devices maintained 70% of their initial PCE after 30 days of exposure to an ambient atmosphere.[29]

P3HT is another HTL material that is widely used in organic photovoltaic devices owing to its free dopant and facile processing without an extra oxidation step.[203] However, the conductivity of pure P3HT limits the hole transport of PSCs. Thus, it is necessary to enhance the hole mobility and conductivity of P3HT HTLs. Ye *et al.* dispersed functional graphene (F-graphene, GO modified by imidazole as shown in Fig. 18b) in P3HT as the HTL in PSCs.[201] The F-graphene showed high mobility and conductivity which is favorable for HTLs in PSCs. According to the space-charge limited current test, the device with bare P3HT displayed a low hole mobility with a slope of 0.07, and was enhanced with a slope of 1.42 after incorporating F-graphene in the HTL. The work function changed from 5.0 eV to 5.2 eV when P3HT was modified with F-graphene.[201] This work function shift creates ohmic contact between the P3HT/F-graphene HTL and the $MAPbI_3$ perovskite. $MAPbI_3$ readily crystallized with the (110) and (220) crystal planes of the F-graphene HTL-based PSCs.[201] As a result, PCEs up to 13.82% were achieved.[201] Compared to devices with a pure P3HT HTL, the incorporation of F-graphene led to a longer device lifetime. Due to the hydrophobicity of graphene composites, F-graphene-based PSCs contained nearly 70% of the pristine PCE after storage in an atmosphere with a humidity of 20–40% for 8 weeks compared with only 35% of the original PCE remaining for bare P3HT-based devices.[201] Composites of rGO with P3HT have been employed to greatly improve the efficiency and stability of PSCs due to the good hole mobility of rGO.[16] rGO and P3HT have the potential to establish π–π stacking interactions between their individual delocalized π electron clouds,[204] making the resulting composites stable. Unfortunately, this does not often occur due to the self-aggregation of pristine rGO. In this regard, chemical functionalization of rGO without disrupting the native electronic structure is useful to improve the dispersion of rGO composites.[205] Gatti and Menna *et al.* investigated the effect of the covalent functionalization of rGO flakes with different organic functional groups (Fig. 18c) on the stability and homogeneity of their dispersion on the surface of the P3HT HTL.[202] The five functional groups are 4-(thien-2-yl)phenyl (PhTh), 4-(5-methylthien-2-yl)phenyl (PhMeTh), 4-[(2-2′-bithiophene)-5-yl]phenyl (PhBiTh), 4-(hexyloxy)phenyl (PhOHex) and 4-[(2-ethyl)hexyloxy]phenyl (PhOEtHex). The alkyl chain-contained PhOHex-functionalized P3HT exhibited the best dispersion, whereas rGO-PhBiTh@P3HT showed the highest surface roughness with the graphene cluster, which acted as carrier recombination sites to diminish the extracted photocurrent.[202] The hexyl chain in PhOHex allows rGO to form a homogeneous film on the surface of the P3HT layer, yielding few protrusions on the HTL surface. In contrast, the bithienyl groups bound to the surface of rGO-PhBiTh@P3HT are prone to the formation of single flakes through the formation of intramolecular π-stacking interactions to produce aggregated rGO flakes, resulting in short circuits between the perovskite and the electrode and thus a low J_{sc}.[202] This work demonstrated the possibility to control the morphology of graphene derivatives dispersed within polymer HTLs by modifying the covalently grafted functional groups.

Graphene derivative-based composite HTLs have enhanced mechanical, electrical and optical properties over polymer HTLs as well as bare graphene derivative HTLs due to the large surface area for effective electrical conduction and carrier transfer, and the 2D functional surfaces enabling strong graphene derivative/polymer interaction. The superior properties of the HTL composites improve hole extraction and transport in PSCs. However, pristine graphene derivatives are usually incompatible with organic HTLs such as PEDOT and P3HT during actual operation. This leads to inferior optical and electrical properties of the composites. In order to improve the properties of the graphene derivative-based composite HTL, techniques aiming to improve the dispersion of graphene derivatives in polymer HTLs need to be explored. Surface modification of graphene derivatives such as nucleophilic addition of organic molecules to the surface of graphene derivatives represents a promising route to achieve modified graphene with solvent dispersible properties, which will assist the preparation of graphene-based HTL composites.[206]

3.3.3 Hole extraction and transport efficiency of graphdiyne-based composites and their effect on device performance. As noted above, the conductivity of pure P3HT semiconductors is limited for hole transportation. Owing to its fascinating properties including excellent semiconducting properties, superior electrical properties and stability, graphdiyne (GD) has been reported to enhance the hole mobility and conductivity of the P3HT HTL.[121] The structure of the GD-doped P3HT composite HTL is shown in Fig. 19a. Strong π–π stacking interaction occurs between graphdiyne and P3HT. The HOMO level of the graphdiyne–P3HT HTL can be lowered while interchain hopping between the polymer chains and graphdiyne can be enhanced due to the π–π stacking interaction.[121] In this way, electrons can be partially transferred from P3HT to GD (Fig. 19b). Furthermore, the addition of GD enhanced light absorption in PSCs because of the improved scattering nature of graphdiyne. The PCE and stability of GD/P3HT-based devices are superior to those of pristine P3HT-based devices.[121] It is proposed that doping of GD into polymer HTLs renders uniform heterogeneous nucleation of the perovskite and thus facilitates perovskite crystal growth by improving the surface wettability of HTLs.[207] When GD was doped into a polymer P3CT-K HTL, a decreased contact angle measured by using DMF and DMSO as solvent at V_{DMF} and V_{DMSO} of 4 : 1 was observed from 12° to 4°,[207] which is beneficial to the flow and spread of the perovskite precursors to yield uniform perovskite films.[179]

As a new carbon allotrope, GD exhibits an attractive structure and physical properties, as well as greater potential than many

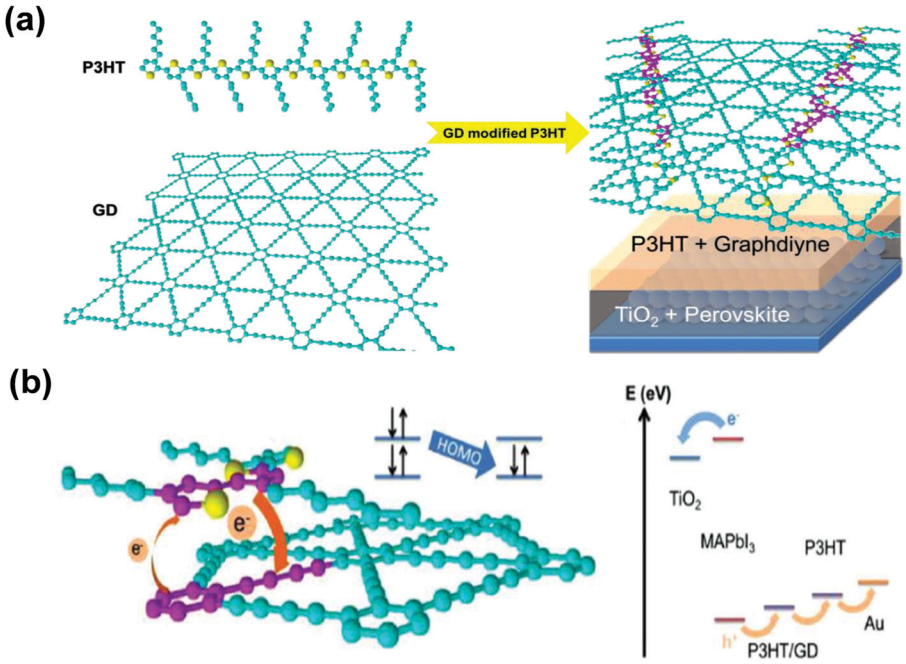

Fig. 19 (a) Schematic of PSCs with P3HT HTLs modified with GD. (b) The atomic-level interaction between GD, P3HT and charge carriers, and the energy levels in P3HT/GD-based PSCs. Reproduced from ref. 121 with permission from John Wiley and Sons, copyright 2015.

other carbon materials for application in solar cells. However, GD-based PSCs are rarely reported. One major challenge is the preparation of a large amount of GDs with high purity.[208] The development and optimization of the processing methods to create well-defined GD nanostructures is still in its infancy. The ability to achieve well-defined GD or GD-based nanostructures with competitive optical and electrical properties and clarify the underlying operating mechanisms may significantly impact both fundamental study and further potential applications of GD.

3.3.4 Hole extraction and transport efficiency of transition metal dichalcogenides and their effect on device performance. Unlike graphene's single atomic layer of carbon, transition metal dichalcogenides (TMDs), such as molybdenum disulfide (MoS_2), tungsten disulfide (WS_2), molybdenum diselenide ($MoSe_2$), and tungsten diselenide (WSe_2), consist of a "sandwich" structure of a transition metal layer between two chalcogen layers. This unique structure determines their distinctive optical and electrocatalytic characteristics as well as chemical stability.[41] The electronic and optical properties significantly change depending on the number of layers. For example, the band energy of MoS_2 increases from 1.29 (multilayer MoS_2) to 1.9 eV (monolayer MoS_2), and the band gap goes from being indirect to direct as the layer number decreases.[209] Furthermore, TMDs possess superior charge carrier capabilities making them applicable in next generation HTLs for use in high-performance PSCs. However, currently only limited work has been done on the incorporation of TMDs into PSCs.

The work functions of MoS_2 and WS_2 are similar to that of GO with values of 5.0, 4.95, and 5.1 eV, respectively.[124] When using MoS_2, WS_2, and GO as HTLs in an inverted $CH_3NH_3PbI_{3-x}Cl_x$ PSC, the PCEs of the MoS_2 and WS_2-based PSCs are comparable to those obtained from GO or PEDOT:PSS-based devices.[124] The lone-pair electrons of the chalcogen atoms in the isolated monolayer structure of TMDs allow for significantly enhanced transport which can improve carrier mobility in devices.[210] Furthermore, the energy levels of TMD layers can be modulated by simple surface treatments. These results indicate that TMDs such as MoS_2 and WS_2 can be promising candidates as HTLs in PSCs. It is well known that 2D MoS_2 and WS_2 have two phases, the semiconducting trigonal prismatic (2H phase) and the metallic octahedral (1T phase).[211] The effect of the crystal structure has been previously discussed elsewhere.[212] Zhou, Song *et al.* used MoS_2 and WS_2 as HTLs in p-i-n type PSCs.[125] It was found that the content of the 1T phase in the HTLs significantly contributed to the improved PCEs. The 1T-rich (2H-poor) TMDs showed improved performance over 1T-poor (2H-rich) TMDs due to the better extraction ability of charge carriers in the 1T phase which exhibited a completely quenched PL.[125] The 1T TMDs possess much higher conductivity than the 2H phase TMDs.[213] The electronic properties of the 1T phase suggested its metallic nature, with an estimated high carrier concentration of $>10^{13}$ cm^{-2}.[213] The highest PCEs for 1T-rich MoS_2 and WS_2-based PSCs were 14.35% and 15.00%, respectively. The small difference between the PCE of MoS_2 and WS_2 is because of the higher work function of the latter at 5.18 compared to 5.13 for MoS_2, a value closer to the valence band of the perovskite. Thus, a higher V_{OC} is achieved.[125] Compared with PEDOT:PSS, these 1T-rich TMD HTLs can further enhance the performance and the stability of PSCs because of the improved moisture resistance.[125] Another reason for the inferior performance of the 2H phase-TMD HTL-based PSCs compared with that of 1T phase-TMD HTL-based PSCs may be due to the formation of a type-I band-alignment (straddling gap) with

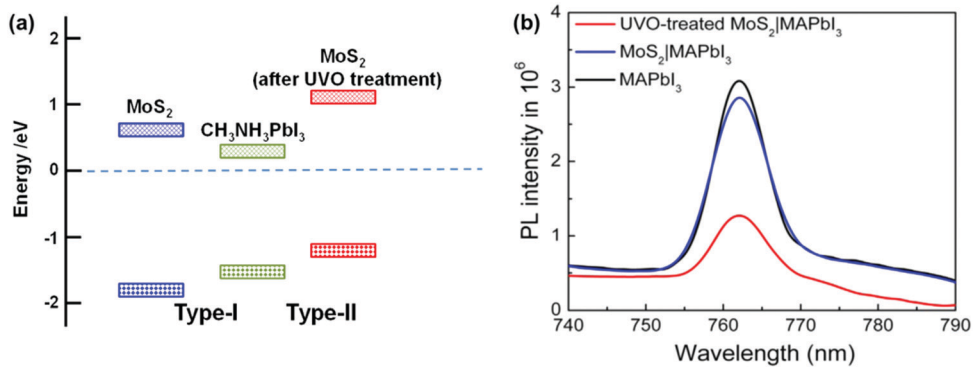

Fig. 20 (a) Band-diagram of MoS_2/$MAPbI_3$ heterojunctions based on two types of MoS_2 with type I and type II heterojunctions illustrated; Fermi energy after alignment is shown as a dashed line. (b) PL spectra of the perovskite layer on quartz, pristine and UVO-treated MoS_2 layers. Reproduced from ref. 214 with permission from Elsevier, copyright 2017.

$MAPbI_3$ as shown in Fig. 20a.[214,215] According to band edge analysis using ultraviolet photoelectron spectroscopy, the valence band maximum (VBM) of $MAPbI_3$ films is −5.79 eV, a value higher than the VBM of the MoS_2 monolayer (−6.28 eV).[214,215] This prevented the efficient extraction and transport of holes from the perovskite to the MoS_2 HTL. To deepen the work function of MoS_2 and form a type-II heterojunction (staggered gap) between MoS_2 and $MAPbI_3$, mild UV ozone (UVO) treatment is an efficient method which can create sulfur vacancies within MoS_2 and form p-type doping to lower the Fermi level of MoS_2.[216] The band edge state-filling in the perovskite slows when the photo-induced holes in the perovskite are transferred into the sulfur vacancy-engineered MoS_2.[216] The hole transfer time from $MAPbI_3$ to MoS_2 was estimated to be $\sim 490 \pm 50$ fs.[216] Thus, the introduction of sulfur vacancies *via* plasma treatment may open routes to ultrafast hole transfer from $MAPbI_3$ to MoS_2. The PL spectra quenching (Fig. 20b) suggests efficient hole transfer from the perovskite layer to the UVO-treated MoS_2 layer.[214]

In addition to MoS_2, TiS_2, another TMD that had been investigated, exhibits good electrical conductivity ($\approx$103 Ohm^{-1} cm^{-1}) and a suitable valence band edge, which is only 0.15 eV lower than that of $MAPbI_3$, indicating a favorable energy level alignment.[15,217] TiS_2 has the added advantage of being 1/30th the cost of the widely used spiro-OMeTAD HTL. Nazeeruddin *et al.* introduced TiS_2 HTLs into n-i-p type mesoscopic PSCs (Fig. 21a–c).[15] The TiS_2-based cell

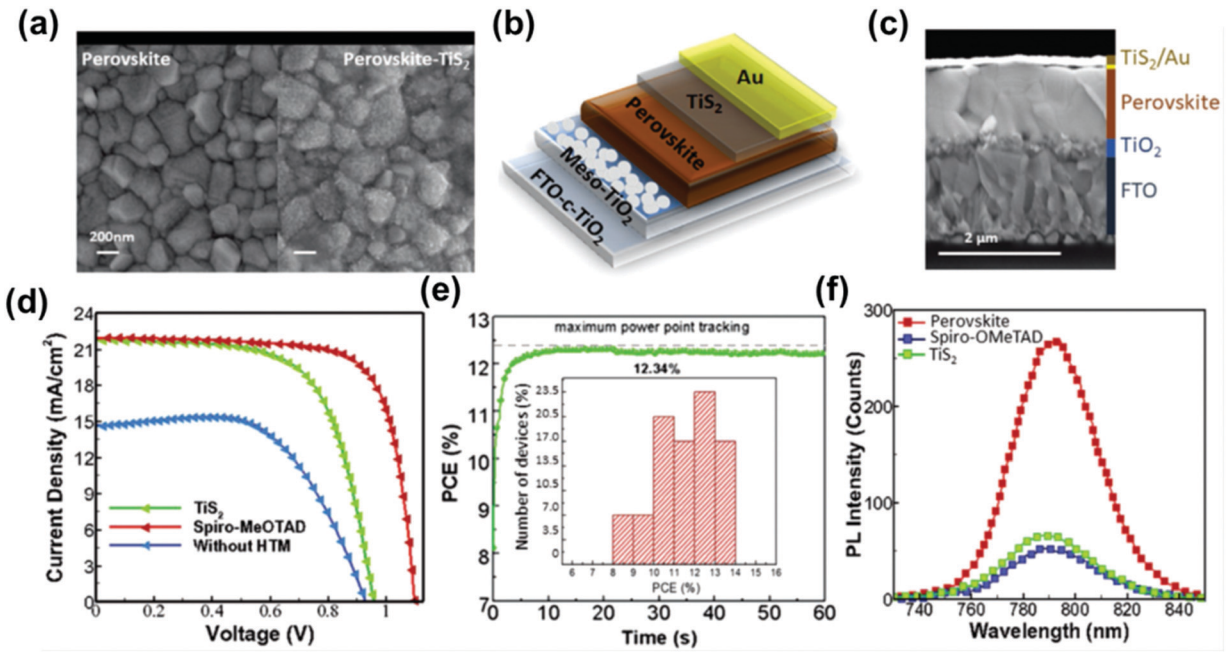

Fig. 21 (a) SEM images of perovskite and perovskite–TiS_2 films. (b) Schematic and (c) cross-sectional SEM image of a typical TiS_2 HTL-based PSC device. (d) *J*–*V* curves of devices using TiS_2 and spiro-OMeTAD as the HTLs and a device without an HTL for comparison. (e) Maximum power point tracking (MPPT) of one of the best performing TiS_2-based devices. Inset: Histogram of PSC efficiencies obtained from more than 50 TiS_2-containing devices. (f) Steady-state PL spectra of PSCs containing TiS_2 and spiro-OMeTAD as HTLs as well as a device with no HTL for comparison. Reproduced from ref. 15 with permission from John Wiley and Sons, copyright 2017.

exhibited a high PCE of 13.5% under full sun illumination, comparable to that of spiro-OMeTAD-based devices (Fig. 21d–f). The presence of a TiS_2 layer on the perovskite led to a nanostructured perovskite morphology although the average crystal grain size of the perovskite remained the same before and after the TiS_2 deposition. It was found that the spin-coating rate had a significant impact on the perovskite morphology. High rates led to improved coverage of the perovskite layer, whereas the roughness of the perovskite film increased significantly due to the large distribution of TiS_2 particles obtained for speeds lower than 5000 rpm.[15]

Although TMDs have promising electrical and optical properties, it remains challenging to mass-produce them. Furthermore, their low solubility in most common solvents makes it difficult to prepare them by simple solution processes. To address these limitations, strategies for functionalizing TMDs were investigated and found to be efficient for enhancing their solubility.[218] After functionalizing 2H-phase MoS_2 with phenyl acetylene silver (PAS), MoS_2 showed good dispersion in polar solvents such as DMF and water.[218] By blending PEDOT:PSS with MoS_2–PAS to serve as the HTL, planar heterojunction PSCs demonstrated an enhanced PCE and stability. The PCE of the devices increased from 14.69% to 16.47% after incorporating MoS_2–PAS with PEDOT:PSS as the HTL. There was only a 13% reduction in the initial PCE after 10 days of storage in an ambient atmosphere owing to the hydrophobicity of MoS_2–PAS. For comparison, there was a 54% decrease in the initial PCE for the device without MoS_2–PAS.[218] Another issue for TMD-based HTLs in PSCs (especially in n-i-p devices) is that the choice of the deposition method is limited because the perovskite layer is sensitive to a variety of solvents. As such, more efficient functional groups need to be explored to increase the solubility of these TMDs in solvents such as isopropyl alcohol and chlorobenzene, which have less impact on the degradation of perovskite films.

3.3.5 Hole extraction and transport efficiency of other two dimensional materials and their effect on device performance. BP (called phosphorene when in monolayer form) is a promising 2D nanomaterial due to its suitable electronic and optoelectronic properties.[25,219–221] Similar to graphene and MoS_2, monolayer phosphorene is flexible, stable and can be mechanically exfoliated. Unlike graphene, BP has a direct band gap. The E_g of single-layer phosphorene is $\sim$2.0 eV.[222] When the BP layer number increases, E_g reduces, reaching a limit of 0.33 eV in the bulk[220] thus providing a large range of values for energy level matching in different device configurations. Interestingly, the direct band gap of BP is independent of the layer number due to the strong conduction band wave function overlap.[67,223] BP exhibits a carrier mobility up to $\sim$1000 $cm^2\ V^{-1}\ S^{-1}$ at room temperature.[224] Thus, it is a promising candidate as a HTL in PSCs. Mhaisalkar, Mathews *et al.* introduced liquid exfoliated few-layer 2D BP nanosheets as a HTL for mesoscopic PSCs with a device architecture of FTO/blocking layer TiO_2/mesoporous TiO_2/$MAPbI_3$/BP/Au (Fig. 22).[25] The low valence band of BP nanosheets (−5.2 eV, Fig. 22a) favors hole injection from $MAPbI_3$ which has a valence band level of −5.4 eV. A PCE of 7.88% was achieved in BP-based PSCs, 4% higher than that observed for HTL-free devices. When using BP nanosheets + spiro-OMeTAD as a HTL, a 25% improvement in PCE from 13.1% (spiro-OMeTAD only) to 16.4% was observed.[25] These early findings strongly suggest that BP nanosheets are a good material for the HTL in PSCs.

All-inorganic novel halide perovskite $CsPbI_3$ and BP heterostructures with two kinds of typical van der Waals-type

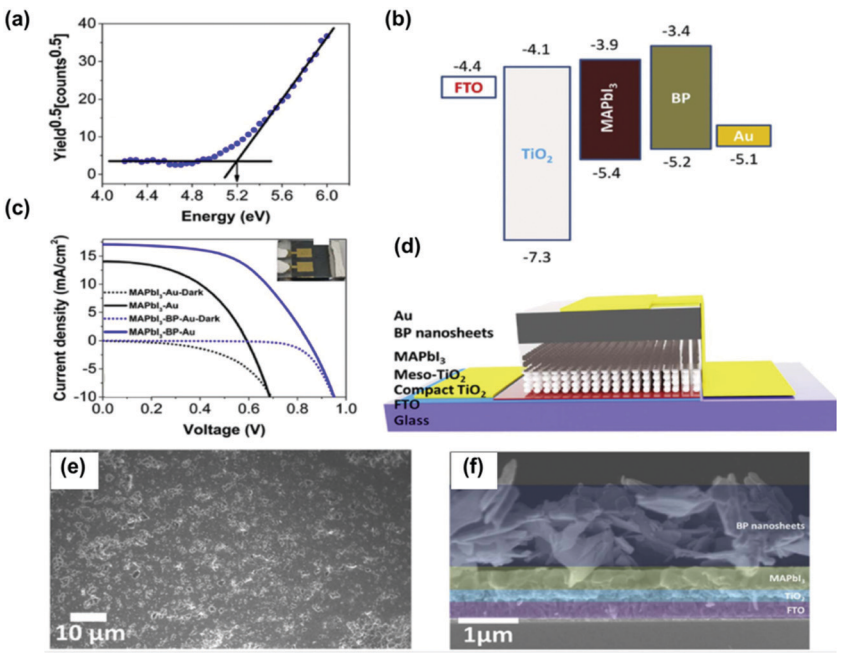

Fig. 22 (a) Photo-electron spectroscopy measurement; (b) band alignment of PSCs based on BP HTLs, (c) *J*–*V* curve of PSCs with (blue) and without (black) BP HTLs, (d) schematic of a PSC with BP, (e) FE-SEM image of BP on $MAPbI_3$, and (f) cross-sectional FE-SEM image of a PSC with a BP HTL. Reproduced from ref. 25 with permission from Elsevier, copyright 2017.

electrical contacts, *i.e.*, the electrical contacts of the Pb–I interface and Cs–I interface with BP, were constructed by first-principle calculations for exploring the structural, electronic, and optical properties of the perovskite/BP interfaces.[225] It was found that the heterostructure of the Pb–I interface contacting the BP showed type-I band arrangement, whereas the Cs–I interface contacting the BP demonstrated type-II band arrangement.[225] The energy level shift can be attributed to the work function difference of $CsPbI_3$ slabs relative to the BP monolayer, driving the movement of carriers spontaneously.[225] In view of the energy alignment, the heterostructure of Cs–I interface of $CsPbI_3$ in contact with BP has great potential for PSCs.[225] Light absorption, especially in the infrared region, is enhanced in $CsPbI_3$-BP heterostructures, thereby improving the potential harvesting of infrared photons in PSCs. Similar heterostructures were constructed between 2D perovskites M_2XBr_4 [M = $(C_4H_9NH_3)^+$; X = Pb^{2+}, Sn^{2+}, Ge^{2+}] and BP.[226] The M_2SnBr_4-BP and M_2GeBr_4-BP heterostructures showed type-II band alignment, whereas the M_2PbBr_4-BP heterostructure exhibited type-I band alignment. [226] Among the three perovskites, the BP increased the light absorption of M_2GeBr_4 the most. In consideration of the energy levels, barrier heights, and light absorption, the M_2GeBr_4/BP heterostructure stood out as the best HTL candidate for PSCs.[226] On the basis of these studies, it is clear that heterostructures between perovskite and BP can efficiently tune the optical and electrical properties of the interface. To achieve high-performance BP-based PSCs, it is imperative to tailor the elemental composition of the perovskite and types of electrical contacts between perovskite and BP.

A few metal oxide nanosheet materials were also investigated for use as HTLs in PSCs due to their large specific surface area which can enable effective charge diffusion.[227] Yu *et al.* fabricated $MAPbI_3$ PSCs using mesoscopic TiO_2 nanosheets and NiO nanosheets as ETLs and HTLs, respectively.[228] The nanosheet-based PSC with printable carbon counter electrodes showed higher PCEs than devices using NiO nanoparticles as the HTL under AM 1.5G illumination. Clearly, nanosheet-structured PSCs can reduce electron–hole recombination and enhance the collection of charge carriers.[228] Compared with NiO nanoparticle HTLs, the nanosheet structure can supply a direct pathway for charge transfer. In addition, 2D NiO nanosheets possess high porosity and large surface area facilitating perovskite loading and diffusion further leading to increased photo-generated electron–hole pairs.[229] NiO nanosheet-based devices showed a higher J_{sc} of 11.2 mA cm^{-2} and an improved V_{OC} of 1.01 V compared to nanoparticle-based counterparts, leading to an average PCE of 7.50%. A higher FF of 0.66 suggests a smaller series resistance and larger shunt resistance for devices with NiO nanosheet HTLs.[228]

3.4 Effect of two dimensional material-based buffer layers on the carrier dynamics and performance of perovskite solar cells

PSC device performance is governed not only by the electronic energy levels and charge carrier mobility of the HTL and ETL materials, but also by the effective charge extraction from the perovskite layer and charge collection by the electrodes. An effective approach to improve the latter two aspects is to incorporate additional buffer layers at the ETL/absorber/HTL/electrode interlayers of the PSC structure. These buffer layers can improve the extraction and collection of carriers. The introduction of buffer layers aims to decrease the trap states induced by the large lattice mismatch between the interfaces, suppress charge recombination and enhance photovoltaic performance.[230]

3.4.1 Graphene oxide buffer layers at the hole transporting layer/electrode interface for improved device stability. 2D GO was chosen as a buffer layer in PSCs because of its high band gap, transparency and mesoporous structure.[21,91,127,231] In addition, carbon nanostructures in PSCs can improve the stability of the cells due to their hydrophobicity.[16] Arora, Dar *et al.* demonstrated a mesoscopic PSC using a thin and uniform CuSCN layer as the HTL and a $CsFAMAPbI_{3-x}Br_x$ (MA = $CH_3NH_3^+$, FA= $CH(NH_2)_2^+$) perovskite layer as the absorber.[127] CuSCN HTLs have high hole mobility (0.1 cm^2 V^{-1} s^{-1}) and well-aligned work functions which facilitate fast carrier extraction and collection.[232] The CuSCN-based PSC achieved an efficiency exceeding 20%. However, due to the degradation of the CuSCN/Au contact induced by the reaction between gold and thiocyanate ions and formation of an undesirable barrier layer, the operational stability is poor.[127] The addition of an rGO spacer layer between CuSCN and Au enabled PSCs to retain >95% of their initial efficiency after aging for 1000 h at 60 °C. These graphene–CuSCN-based devices surpass the stability of spiro-OMeTAD-based PSCs.[127] The effect of graphene as an interlayer between the Au electrode and the spiro-OMeTAD HTL was also studied in planar PSCs.[61] Stability testing showed that more than 94% of the initial PCE in graphene-based devices was retained after ageing in 45% humid air for 96 h or thermal annealing at 80 °C for 12 h. These performance values clearly support the importance of graphene layers in improving PSC stability across many different material compositions. This graphene interlayer can block the diffusion of air and Au into the perovskite layer after annealing treatment which further reduces carrier recombination.[61]

3.4.2 Graphene derivative and MoS_2 buffer layers at the perovskite/hole transporting layer interface for improved hole extraction from the perovskite. The deposition of a buffer layer between the perovskite and the HTL can also improve PSC performance. It was found that metals can migrate from the electrode through the HTL and eventually contact the perovskite. This is in part responsible for PSC device degradation.[233] The contact between the metal and the perovskite leads to a low shunt resistance during aging and in turn the degradation of PSCs.[233] Depositing a HTL within a buffer layer can prevent metal migration while blocking the shunt pathway that can arise during aging. The consequence of the introduction of such a buffer layer is a considerable improvement in V_{OC} and FF as well as device stability.[21,91] A thin layer of GO nanosheets employed as a buffer layer sandwiched between the perovskite and the tetra-*n*-butyl-copper phthalocyanine (CuBuPc) HTL was found to inhibit the formation of shunting pathways and improved HTL morphology.[231] The presence of the GO buffer layer prevented the formation of aggregated structures with voids in CuBuPc and thus blocked the shunt paths. The GO buffer layer facilitated hole transport between the perovskite and the CuBuPc layer. The efficiency of GO-based solar cells increased to a maximum of

14.4%, whereas devices without the GO layer achieved a maximum PCE of 7.3%. It was also found that the GO buffer layer at the perovskite/HTL interface can improve the contact between the absorber layer and the HTL.[21] The surface contact angle of PSCs decreased from 13.4° to zero degrees (fully wetting) after introducing GO as the buffer layer. This can be ascribed to the amphiphilic nature of GO. The decreased contact angle led to an enhancement of the short circuit current due to the improved contact between the perovskite and the HTL.[21]

On the basis of the discussion noted above, GO appears to be a good buffer layer candidate used between perovskite and HTL to improve the efficiency and stability of devices. However, one major risk is that GO may accelerate the degradation of the perovskite once the active layer is decomposed in air. Carlo *et al.* investigated the stability of PSC devices using graphene-doped mesoporous TiO_2 ($mTiO_2$ + G) as the ETL and GO as the buffer layer between the perovskite active layer and the spiro-OMeTAD HTL.[234] Four cells with different structures were designed (Fig. 23a and 24f). Device C, using $mTiO_2$ + G as the ETL, showed remarkable stability with 88% retention of the initial PCE value after 16 h of thermal stress testing.[234] Under the same conditions, the perovskite/GO/HTL interface (device B) suffered degradation because the GO layer was reduced upon irradiation.[234] In the presence of O_2 and H_2O, $MAPbI_3$ single crystals can undergo decomposition with the release of $CH_3NH_2^+$ and HI.[235] HI can reduce GO to rGO which may react with photo-generated electrons and further accelerate the decomposition of the perovskite.[236] Thus, rGO may not be a promising alternative as the buffer layer between perovskite and HTL in PSCs. However, the use of a functionalized rGO instead of pristine rGO as a buffer layer in PSCs may change the situation. Wang *et al.* introduced 4-fluorophenyl-functionalized rGO (rGO-4FPH) as an interfacial layer between the perovskite and the HTL.[22] The 4-fluorophenyl functionalization passivated the traps on the surface and at the grain boundaries within the perovskite layer by interacting with the under-coordinated Pb

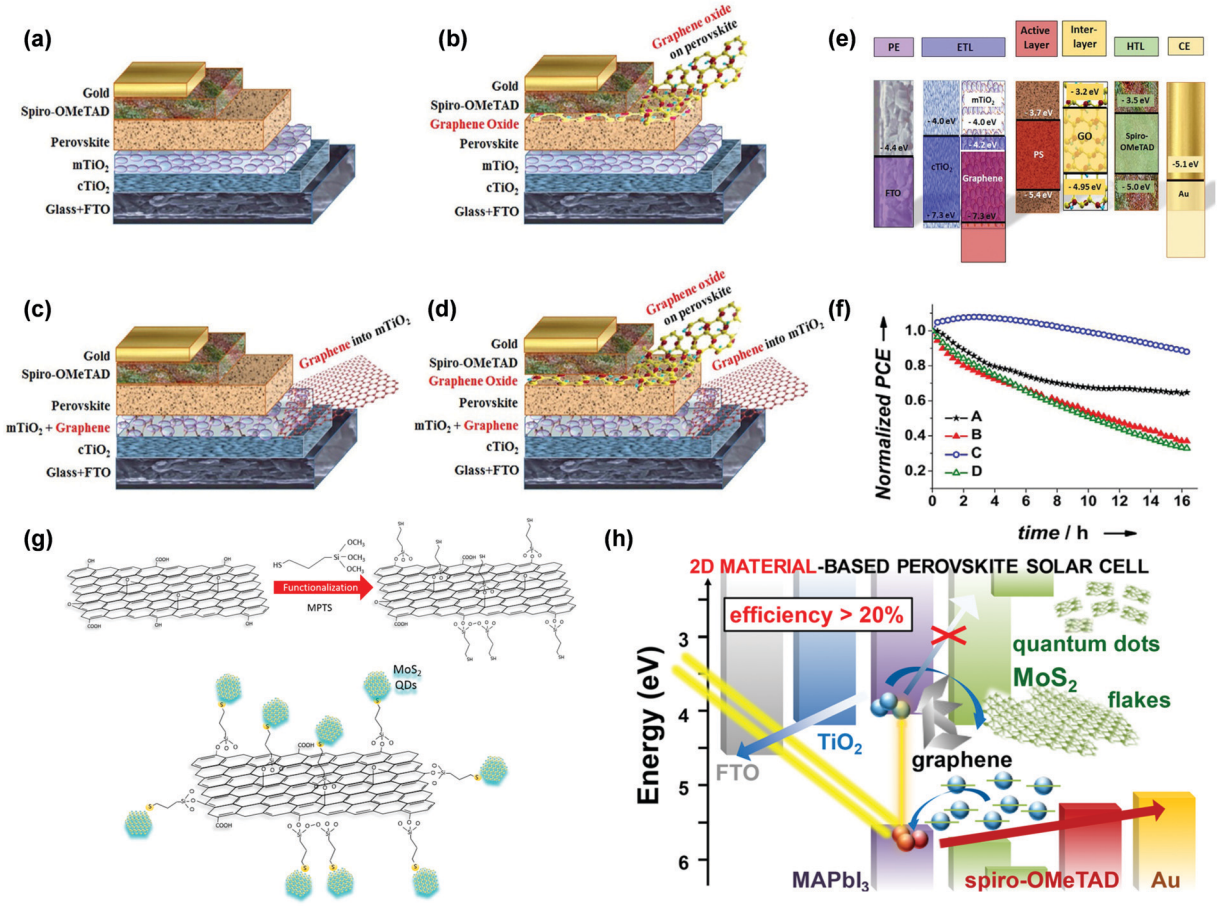

Fig. 23 PSC structures (a) without a buffer layer between the perovskite and spiro-OMeTAD layers (device A), (b) with graphene oxide (GO) as an interlayer between the perovskite and spiro-OMeTAD layers (device B), (c) with mesoporous TiO_2 ($mTiO_2$) + graphene (G) interlayer (device C), and (d) combined device with the layer structure FTO/contact TiO_2 ($cTiO_2$)/$mTiO_2$ + G/perovskite/GO/spiro-OMeTAD/Au (device D), and (e) energy band diagram of the different functional layers in a PSC relative to vacuum. The band alignments are not to scale and show only the relative position of the energy levels. (f) PCE trends *versus* time under extended 1 sun illumination at maximum power point polarization provided by a calibrated white LED for devices A through D. Reproduced from ref. 234 with permission from John Wiley and Sons, copyright 2016. (g) Schematic illustration of the functionalization of rGO (upper panels) and the hybridization of MoS_2 QDs and rGO (lower panel). (h) Schematic of the energy band edges of materials used in the rGO/MoS_2 QD buffer layer-based PSC. Reproduced from ref. 237 with permission from American Chemical Society, copyright 2018.

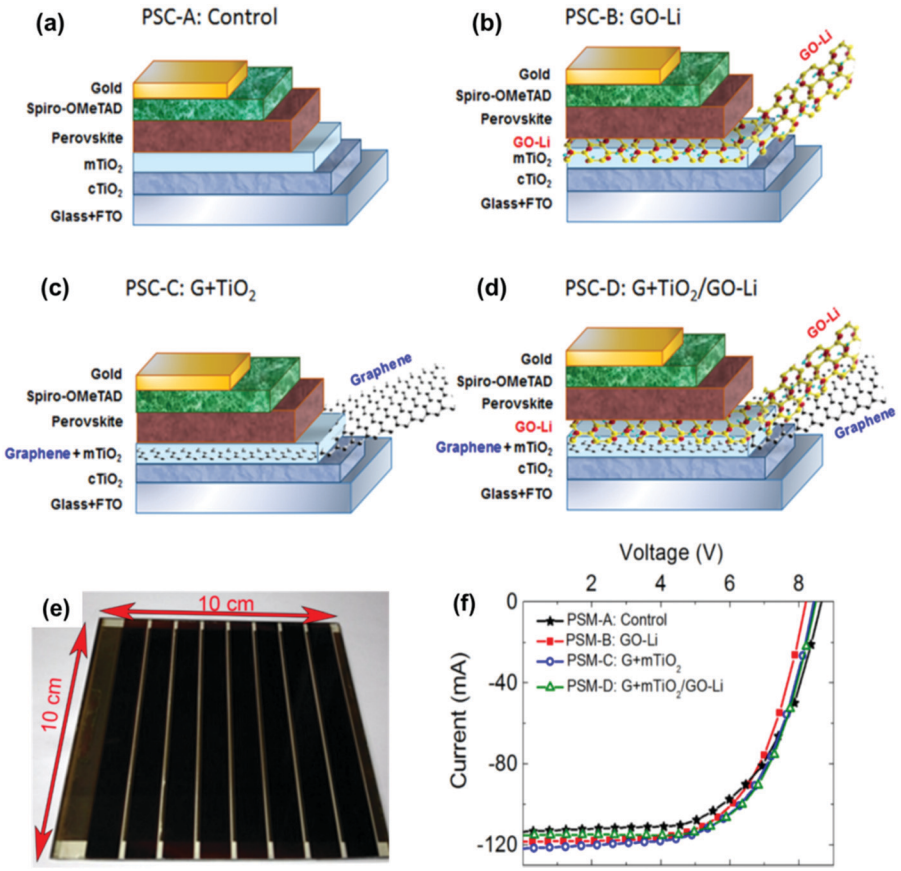

Fig. 24 PSC layer structures (a) with the reference mesoscopic structure FTO/$cTiO_2$/$mTiO_2$/perovskite/spiro-OMeTAD/Au, (b) with the GO-Li buffer layer between perovskite and $mTiO_2$ layers, (c) with graphene-doped $mTiO_2$ as the ETL, and (d) with GO-Li as the buffer layer and graphene-doped $mTiO_2$ as the ETL. (e) Photograph of a large-area PSC device (50 cm^2 active area). (f) *J*–*V* characteristics of the different modules tested. Reproduced from ref. 20 with permission from American Chemical Society, copyright 2017.

ions in the perovskite layer.[22] As a result, it reduced interfacial recombination and enhanced hole extraction efficiency which further enhanced the V_{OC}. The rGO-4FPH-based PSC achieved a V_{OC} of 1.11 V and a PCE of up to 18.75%.[22] Despite similar stability for devices with and without a buffer layer in air (with humidity at approximately 30%), a slightly higher stability under glovebox illumination was observed after the incorporation of the buffer layer in the devices.[22] A hybrid structure with MoS_2 quantum dots (QDs) and functional rGO (obtained by chemical silanization-induced linkage between rGO and (3-mercaptopropyl)-trimethoxysilane) in PSCs was designed as a buffer layer between $MAPbI_3$ and spiro-OMeTAD.[237] As shown in Fig. 23g, the functional molecules anchored onto the rGO enabled f-rGO to interact with MoS_2 QDs.[237] The van der Waals hybridization of MoS_2 QDs with rGO enabled a uniform deposition of HTLs or buffer layers onto the perovskite film owing to the filling of pinholes of the MoS_2 QD films by rGO.[237] MoS_2 QDs provide both hole-extraction and electron-blocking properties due to their suitable energy alignment with the perovskite (Fig. 23h). Effective collection of the photo-generated holes from the perovskite towards the anode was achieved, reaching a maximum PCE of 20.12%.[237] The rGO buffer layer-based PSCs exhibited a reduced PCE of only 8.8% after 1032 h of aging. This is significantly lower than that of devices without the buffer layer (PCE = 24.6%).[237] The improved stability can be attributed to the surface passivation of the perovskite layer rendered by the rGO buffer layer. A TDM composed of liquid-phase exfoliated few-layer MoS_2 flakes has also been exploited as an active buffer layer in PSCs with a layer structure of glass/FTO/$cTiO_2$/$mTiO_2$/$CH_3NH_3PbI_3$/MoS_2/Spiro-OMeTAD/Au.[126] The MoS_2 buffer layer serves two functions: first, it forms a barrier preventing metal electrode migration, and second it serves as an energy-matching layer to further ease hole collection from the spiro-OMeTAD HTL for transport to the electrode. As a result, the MoS_2-incorporated PSCs (0.1 cm^2 active area) achieved a higher PCE (13.3%) and improved stability over a period of 550 h (93% peak PCE retention *vs.* 66% PCE retention for the reference cell without the MoS_2 buffer layer.[126]

3.4.3 Graphene oxide buffer layers at the perovskite/electron transporting layer interface lead to improved electron extraction from the perovskite. Modifying the interface between the ETL and the perovskite layer is proposed as an effective way to boost the PCE of PSCs by limiting the charge losses occurring at the perovskite/ETL interface, simultaneously improving the device stability. Bonaccorso, Carlo *et al.* introduced the concept of graphene interfacial engineering using lithium-neutralized graphene oxide (GO–Li) flakes as an interlayer between the mesoporous TiO_2 ($mTiO_2$) and perovskite layers to improve charge injection from

the perovskite layer into the $mTiO_2$ layer.[20] Graphene flakes were also dispersed into the $mTiO_2$ ETL to facilitate electron transport. The fabricated PSC architectures are shown in Fig. 24. An increased electron injection from the perovskite to the $mTiO_2$ layer and a reduction in back-transfer processes from the $mTiO_2$ to the perovskite layer were observed as a result of the GO–Li buffer layer. A significant improvement in the average J_{sc} (+18%) was observed for device B. Meanwhile, there was a 4.3% loss in V_{OC} due to the downward displacement of the conduction band of TiO_2.[20] In contrast, device D with graphene flakes incorporated into the TiO_2 layer did not show a reduction in V_{OC}. First-principle calculations on graphene/$MAPbI_3$ interfaces suggested that graphene can suppress the octahedral tilt of the perovskite, leading to ferroelectric distortion with a permanent polarization.[238] Such polarization drives electron extraction from the perovskite into the ETLs. A PCE of 12.6% on an over 50 cm^2 active area of PSCs was achieved in the presence of the GO–Li buffer layer.[20]

4. Tunable optoelectronic properties of 2D perovskite absorbers and their effect on device performance

2D perovskite active layer materials in solar cells exhibit excellent photoelectric conversion efficiencies while maintaining the excellent light absorption properties of three-dimensional perovskites.[239–241] 2D perovskites are direct band-gap materials in which the process of exciton generation is very fast.[80] It was found that the photo-generated holes and electrons in layered 2D perovskites could be transferred in different directions within the perovskite film, and further accumulated at the top and bottom of the film, respectively.[242] Consequently, charge collection at the electrodes became easier. Compared to the traditional 3D $MAPbI_3$ perovskite, the layered 2D perovskite structure offers greater tunability at the molecular level for optimizing the optical and electrical properties of materials.[130] Single-crystalline $(C_4H_9NH_3)_2PbBr_4$ prepared *via* separating the individual layers of $PbBr_4^-$ was first reported in 2015.[241] As-grown 2D perovskite sheets exhibited high PL quantum efficiency as well as wide composition and color tunability on changing the perovskite sheet thickness.[241] A slightly increased optical band gap of the 2D hybrid perovskite sheets with respect to the bulk crystal was observed. This is likely induced by the lattice expansion.[241] The 2D perovskite structure with a larger bandgap is also suitable as a higher bandgap absorber in a dual-absorber tandem device.[130]

Garner *et al.* optimized 2D perovskite structures by varying the length of the organic chain on the diammonium cations.[243] The investigated perovskite materials include $[NH_3(CH_2)_4NH_3]PbI_4$ ($BdAPbI_4$), $[NH_3(CH_2)_6NH_3]PbI_4$ ($HdAPbI_4$), and $[NH_3(CH_2)_8NH_3]PbI_4$ ($OdAPbI_4$) with band gaps of 2.37, 2.44 and 2.55 eV, respectively.[243] Compared to traditional $MAPbI_3$, these 2D perovskites have larger band gaps and lower photo-conductivity. The performance of PSCs using 2D perovskite materials as the light absorbing layer was investigated as well. As the whole process of solar cell fabrication (except for the silver evaporation process) is performed in ambient air (with a humidity of 55.6%) and at ambient temperature (23.4 °C), the moist conditions produce PSCs with overall poor quality. The best performing material was $BdAPbI_4$ with a PCE of 1.08% comparable to that of $MAPbI_3$-based solar cells (2.1%).[243] However, the stability of $BdAPbI_4$- and $HdAPbI_4$-based PSCs (PCE dropped from 1.082% to 0.798% and 0.592% to 0.339% after 4 days, respectively) is superior to that of $MAPbI_3$-based devices (PCE dropped from 2.11% to 0.03% over the same period). The devices are also thermally stable up to 200 °C.[243] Zhou *et al.* fabricated ternary cation halide quasi-2D perovskite active layer materials such as $(BA)_2(MA,FA)_3Pb_4I_{13}$ (where BA = n-$C_4H_9NH_3$, MA = methylamine, FA = formamidinium), in which MA is gradually replaced by FA.[244] It was found that the incorporation of FA^+ can improve perovskite crystallization to enable the reduction of non-radiative recombination centers. An *in situ* PL technique was employed to probe the phase formation sequence wherein the 2D $(BA)_2(MA, FA)_{n-1}Pb_nI_{3n+1}$ phase (n = 2, 3, 4) formed early, followed by the generation of $(MA, FA)PbI_3$ ($n = \infty$) in a quasi-2D perovskite system.[244] A peak efficiency of 12.81% was reported for such 2D perovskite-based solar cells (Fig. 25a). In order to further improve the properties of the 2D $(BA)_2(MA, FA)_3Pb_4I_{13}$ perovskite, cesium cations (Cs^+) were doped into the structure (Fig. 25b).[245] These devices exhibited a maximum PCE of 13.68% with excellent moisture tolerance and thermal stability.[245] Cs^+ plays a key role in controlling the oriented growth of perovskite crystals and increasing the crystal dimension. As a result, Cs^+ doping improves the optoelectronic properties by reducing trap density, increasing charge-carrier mobility, and increasing charge-transfer kinetics. Docampo *et al.* developed a facile solution-based cation infiltration process to produce a hybrid 2D/3D perovskite film in which a 2D layered perovskite (LPK) is deposited onto methylammonium lead iodide (MAPI) films (Fig. 25c).[246] The MAPI/LPK heterojunction system incorporating phenylethylammonium has a PCE up to 16.84% due to the increased V_{OC} and FF which are related to a reduction in charge recombination. The top layer of the 2D LPK can act as a selective charge extraction layer for the MAPI perovskite leading to suppressed recombination of photo-generated carriers.[246] These results suggest that the formation of a 2D perovskite interface on top of the $MAPbI_3$ perovskite improves the photovoltaic and optoelectronic properties of the overall PSC device.

The low Young's modulus and unique modular structural sequence of 2D perovskites add additional structural flexibility and enable their use as an active layer in high-performance PSCs.[247] To date, however, the efficiency of 2D-based PSCs is still unsatisfactory due to the suppressed out-of-plane charge transport by the organic cations in 2D perovskites. The properties of 2D perovskites still depend highly on the inorganic counterpart with only a few exceptions. Functionalization or modification of the organic portion, such as using small organics with strong charge transfer properties to improve the conductivity of 2D perovskites, will open up an avenue for property discovery and development.[247,248]

5. Stability of two-dimensional material-based perovskite solar cells

In addition to high efficiency, long-term device stability remains a lingering and essential challenge to overcome in solar cells in

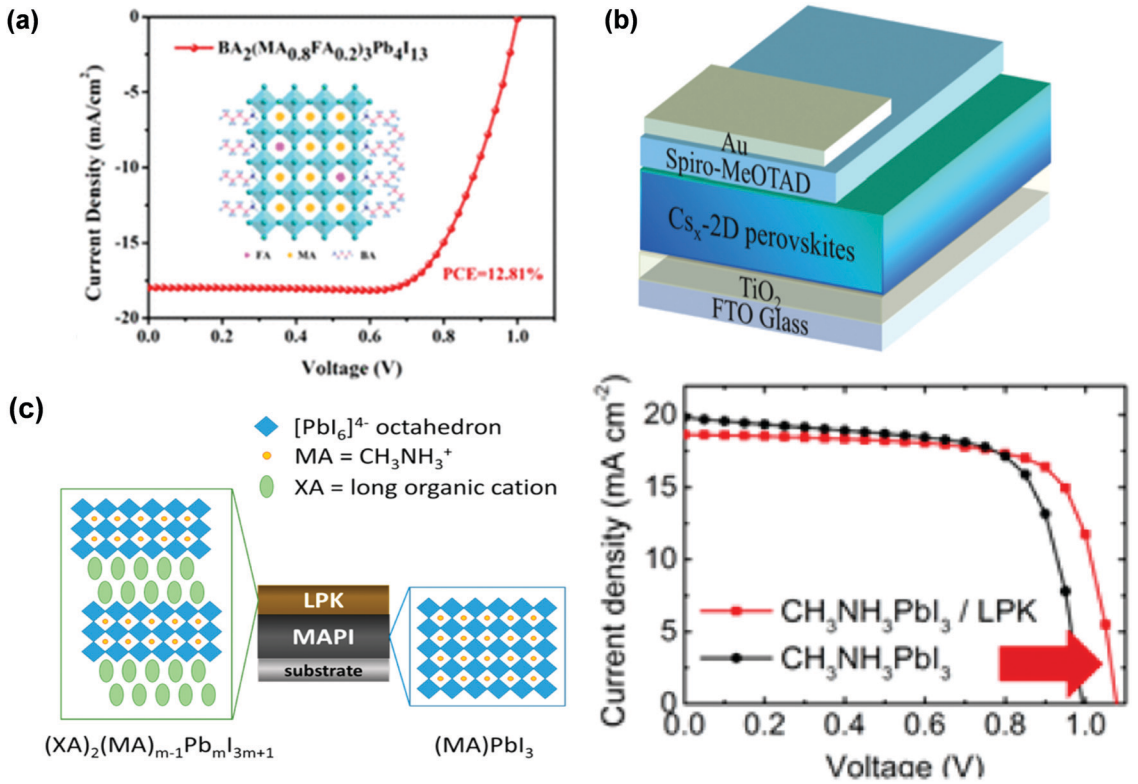

Fig. 25 (a) PL measurement for a $(BA)_2(MA, FA)_{n-1}Pb_nI_{3n+1}$ film produced by detecting the emission peak at 585 nm (n = 2), 670 nm (n = 4), and 780 (n = ∞), and the J–V curve of a $(BA)_2(MA_{0.8}FA_{0.2})_3Pb_4I_{13}$-based PSC; the inset is the crystal structure of $(BA)_2(MA_{0.8}FA_{0.2})_3Pb_4I_{13}$. Reproduced from ref. 244 with permission from American Chemical Society, copyright 2018. (b) Device architecture of a Cs_x-incorporated 2D perovskite-based PSC. Reproduced from ref. 245 with permission from The Royal Society of Chemistry, copyright 2017. (c) Crystal structures of methylammonium lead iodide (MAPI) and a layered perovskite (LPK) with their performance in solar cells. Reproduced from ref. 246 with permission from American Chemical Society, copyright 2016.

order to realize future commercial development. Several reaction pathways involving water, oxygen, light, acid and heat lead to the degradation of several device materials. Among them, H_2O and O_2 are two significant factors impacting the stability of devices.[29,61,116,126,234,249] Perovskites tend to hydrolyze under high humidity because of their high sensitivity to water, leading to the degradation of the active layers in PSCs. The conversion of the perovskite $MAPbI_3$ follows the following equations:[250]

$$CH_3NH_3PbI_3 \leftrightarrow PbI_2 + CH_3NH_3I \quad (1)$$

$$CH_3NH_3I \leftrightarrow CH_3NH_2I + HI \quad (2)$$

$$HI + O_2 \leftrightarrow I_2 + H_2O \quad (3)$$

$$2HI \leftrightarrow H_2 + I_2 \quad (4)$$

In addition, the diffusion of molecular oxygen can be activated by illumination in the presence of organic molecules, promoting the formation of peroxide or superoxide compounds that attack and degrade the active layers. The long-term stability of PSCs in the presence of moisture and oxygen can be improved by an interfacial buffer layer, as noted in Section 3.4, which can avoid the direct contact between perovskite and moisture.[61,126,127] Two dimensional graphene-related materials are well known for being thermally, mechanically and chemically stable. They can be easily processed into uniform ultrathin optically transparent layers which can efficiently transport electronic charge carriers as well.[251] It was reported that an rGO buffer layer between a CuSCN HTL and a Au electrode enabled PSCs to retain >95% of their initial efficiency after aging for 1000 h at 60 °C.[122] A 4-fluorophenyl-functionalized rGO (rGO-4FPH) interfacial layer between the perovskite and the HTL was also found to enhance the stability of PSCs.[22] The improvement in stability results from the rGO layer diffusion barrier, which hinders the diffusion of oxygen molecules from the electrode to the active layers. It is known that PEDOT:PSS is typically used as the HTL in PSCs, which is acidic and hygroscopic in nature and thus facilitates the decomposition of active layers in PSCs. Pristine graphene is hydrophobic, whereas the GO surface consists of hydrophilic regions with hydrophobic islands.[49,184] Yeo *et al.* reported that a PEDOT:PSS-based PSC was completely deteriorated and the PCE decreased to 0% after 5 days of exposure to ambient conditions.[119] In comparison, rGO-based solar cell devices retained 62% of their initial PCE (9.95%) after 6 days, suggesting improved stability against oxygen and moisture compared to conventional PEDOT:PSS-based solar cell devices.[119]

2D perovskites have been recognized as improving the stability of PSCs. Despite this, the underlying mechanism remains unclear.[245] It is reported that the moisture stability of perovskite can be improved by partial substitution of the MA^+ cations with long-chain organic cations which can change the

perovskite structure from 3D to 2D.[129,130,252,253] The hydrophobicity of long organic cations prevents direct contact between water and perovskite layer. Tsai, Nie *et al.* used Ruddlesden–Popper layered 2D perovskites, $(BA)_2(MA)_2Pb_3I_{10}$ ($n = 3$) and $(BA)_2(MA)_3Pb_4I_{13}$ ($n = 4$), to produce PSCs with near-single-crystalline active layers (Fig. 26a).[129] Stability testing under constant light illumination (AM1.5G) or in a humidity chamber (with a relative humidity of 65%) showed that unprotected 2D perovskite-based devices retained over 60% of their initial efficiency after 2250 h of illumination. These devices also exhibited improved humidity resistance when compared to their 3D equivalents.[129] Similar results are also observed for the encapsulated devices with no degradation occurring in the

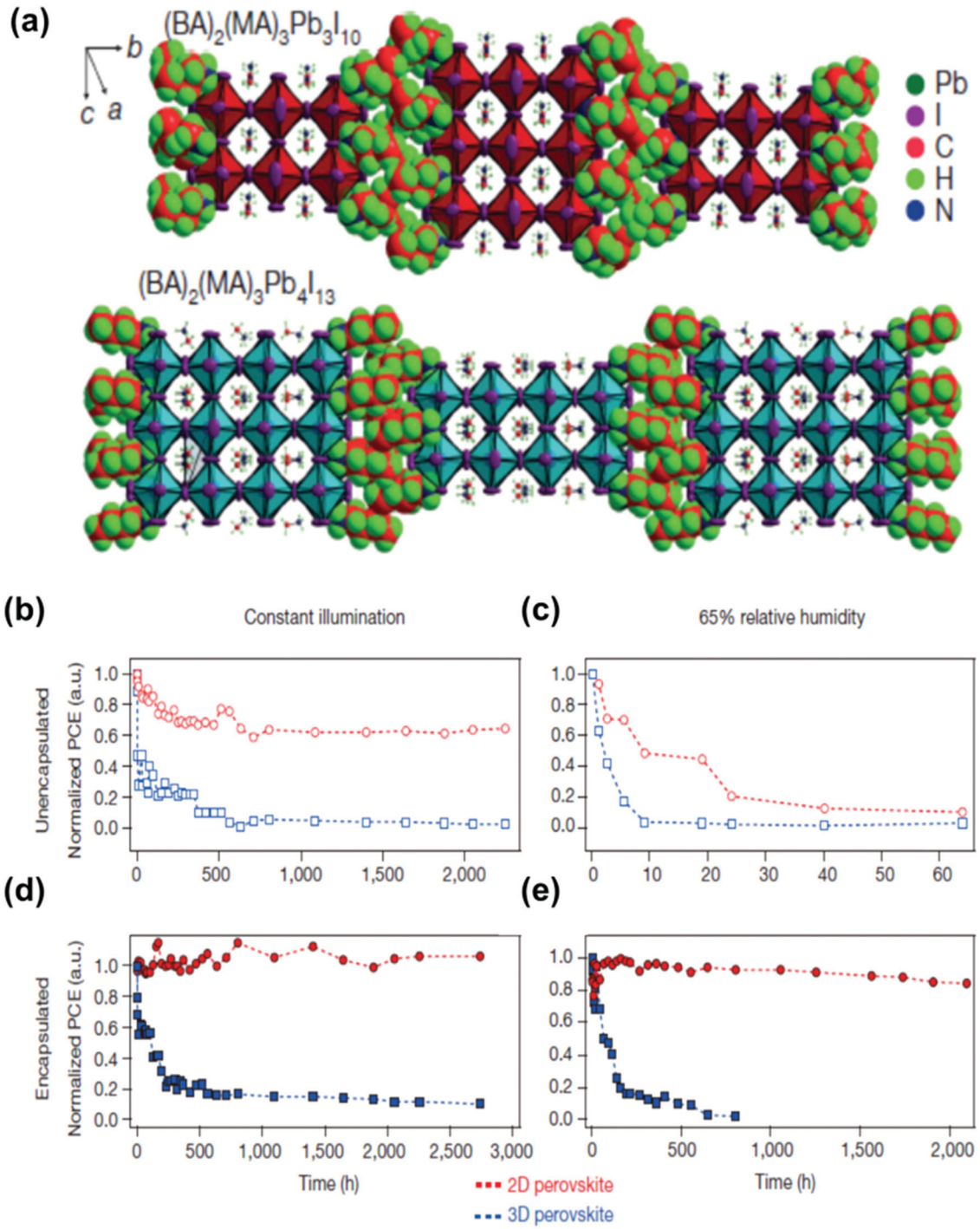

Fig. 26 (a) The crystal structures of the $(BA)_2(MA)_2Pb_3I_{10}$ and $(BA)_2(MA)_3Pb_4I_{13}$ layered perovskites. (b) Photo-stability tests under constant AM1.5G illumination for 2D $(BA)_2(MA)_3Pb_4I_{13}$ (red) and 3D $MAPbI_3$ (blue) perovskite devices without (b) and with (d) encapsulation. Humidity stability tests under 65% relative humidity for 2D $(BA)_2(MA)_3Pb_4I_{13}$ (red) and 3D $MAPbI_3$ (blue) perovskite devices without (c) and with (e) encapsulation. Reproduced from ref. 129 with permission from Springer Nature, copyright 2016.

layered 2D perovskite-based devices under extended illumination (Fig. 26b and d) or humidity exposure (Fig. 26c and e). The 2D perovskite-based devices exhibited enhanced stability in comparison to their 3D counterparts.[129] The slower degradation may be due to the hydrophobic properties of the long organic side groups in the 2D perovskite structure which can prevent direct moisture exposure. Despite their superior stability, the efficiency of 2D-based PSCs is unsatisfactory due to the suppressed out-of-plane charge transport by the organic cations in 2D perovskites.[254] Tsai, Nie *et al.* fabricated thin hot-cast films of near-single-crystalline quality to optimize the preferential out-of-plane alignment of the inorganic perovskite component which can facilitate efficient charge transport.[129] The crystal domains in the hot-cast films are oriented with their (101) planes parallel to the substrate surface with a 2D in-plane orientation randomness.[129]

6. Conclusions and outlook

Two dimensional materials can serve as conductive electrodes, carrier transporting layers and buffer layers for application in PSCs. The applications of graphene (and its derivatives), BP, transition metal dichalcogenides, and metal oxide nanosheets in PSCs have led to devices with superior photovoltaic performance. The electrical and optical properties of TDMs can be tuned by controlling the thickness and functionalization process. Furthermore, the van der Waals interaction between neighboring atomic layers allows for more flexible integration of different materials to control the optical and electrical properties at the atomic scale as needed. The tunable energy-level capabilities of TDMs allow them to pair with a number of donor/acceptor systems in PSCs to form well-matched energy levels for effective carrier extraction, transport and collection. Other unique properties of TDMs including excellent mechanical flexibility and a large specific surface area facilitate charge transfer and light absorption which further improve the performance of TDM-incorporated PSCs. In addition, the incorporation of TDMs in PSCs can improve the morphology of other layers such as the HTL and the perovskite layer, thereby increasing carrier generation in the perovskite and facilitating carrier extraction at the interfaces. 2D active perovskite absorbers in PSCs can be considered a feasible alternative to 3D perovskites. The long alkyl chains contained in the organic cations of 2D perovskites confer hydrophobicity to the perovskite structure which provides a greater resistance to humidity when compared to 3D perovskites. The optical and electrical properties of 2D perovskites can be tuned by using different organic cations. Thus, the 2D perovskite structure can be electronically designed to fit the selective contacts of various established and emerging PSC architectures.

Although significant progress has been made in TDM-incorporated and 2D perovskite-based PSCs, several challenges remain to be addressed. First, since the surfaces of TDMs are mostly hydrophobic, it is difficult to dissolve them directly in water without additional surface treatments. Finding appropriate solvents to dissolve these TDMs for use in PSCs is a significant problem. A facile method to improve water solubility is through covalent functionalization. Covalent attachment of functional groups is generally achieved by reaction with unsaturated atoms at the edges or defect sites which change their properties and lead to improved solubility of TDMs in common solvents. For example, GO can be tethered to $-CH_2OH$ terminated regioregular P3HT *via* esterification reaction to exhibit superior solubility due to the presence of an abundant number of hydroxyl groups in the added polymer.[255] For example, conjugated polymer functionalized BP derivatives such as (poly[(1,4-dieth-ynylbenzene)-*alt*-9-bis(4-diphenylaminophenyl)fluorene]-(PDDF)-covalently grafted BP) showed very good solubility in organic solvents. Second, although CVD methods are commonly used to produce TDM thin films, the as-synthesized single-layer films inevitably have high sheet resistance (*i.e.*, $\sim 1050 \pm 150\ \Omega\ sq^{-1}$ for graphene). The prevalent defects such as vacancies, impurities, nanoplatelet edges, and topological defects as well as the defect density in the TDM lattice can increase electron scattering resulting in an increase in sheet resistance. Finding an efficient way to reduce the sheet resistance of TDMs is of great importance for enhancing the performance of TDM-based PSCs. One strategy is to stack TDMs to form a multilayer structure which can introduce more channels for charge transport. Preparation techniques need to be optimized in terms of solvent, temperature, time and precursor selection to improve the quality of the TDM lattice and thereby enhance its conductivity. Another strategy is to increase the density of states by shifting the Fermi level of TDMs to raise the conductivity. Surface treatments such as doping and functionalization can improve the sheet resistance of TDMs by moving the Fermi level of TDMs to a region where the resistance is considerably lower due to an increase in the density of states. For example, graphene sheets with electron donating groups, such as –COOR (ester), have relatively low sheet resistance than that of pristine graphene sheets.[256] Benzyl viologen-doped MoS_2 showed higher electron sheet density and lower resistance than pristine MoS_2.[257] A graphene–conducting-carbon-nanotube hybrid material circumvents electron scattering due to defects in graphene and reduces the sheet resistance by a factor of two relative to the neat graphene. In addition, the resistance can be further reduced by doping the hybrid with nitric acid. Third, the physical processes involved in the incorporation of TDMs into PSCs, such as interface transport, need to be better understood in order to achieve more efficient solar cells. Factors such as crystallization, position and orientation of TDMs also have a significant impact on the performance of PSCs with each requiring further investigation and optimization to improve device efficiency. Another figure of merit for high performance PSCs is the thickness of the layers. Engineering PSCs for achieving the desired performance with various mono- or few-layered TDMs by assembling them into stacks is challenging. The development of synthesis strategies for TDMs of different layer architectures is essential to produce high-performance devices requiring different performance characteristics for different applications. Fourth, some TDMs, such as graphdiyne and BP, have been shown to enhance the performance of PSCs. However, reports on these TDM-based PSCs are still scarce, and more research should be devoted to

these novel TDM materials to further boost their performance in PSCs. For 2D perovskite-based PSCs, the performance is still not comparable to that of 3D perovskite-based devices due to transport problems and the large exciton binding energy. Carrier transport through 2D perovskite films is inhibited due to the presence of long organic cations which act as insulating layers between the conducting inorganic slabs. One way to improve the performance of 2D perovskite-based PSCs is by controlling the preferential out-of-plane alignment of the crystallographic planes of the inorganic perovskite components to enhance charge carrier transport through selective contacts. Another approach is to design 2D perovskite-based PSCs in the form of a bulk heterojunction (*i.e.*, an interpenetrating network at layer junctions) where the diffusion length of the exciton can be decreased to facilitate charge carrier separation.

The development of 2D materials will provide a new promising resource for incorporation into high-performance PSCs. Once the feasibility and benefits of TDMs are maximized to improve device efficiency, the promise of low-cost solar cells will be that much closer to being realized and commercialized.

Conflicts of interest

There are no conflicts to declare.

Acknowledgements

This work was financially supported by the AFOSR (FA9550-19-1-0317), NSF (CMMI 1914713, ECCS 1914562, DMR 1903990 and CBET 1803495), National Natural Science Foundation of China (21603098, 61728403, 21471116 and 51772219), Natural Science Foundation of Jiangsu Province (BK20150580), and Zhejiang Provincial Natural Science Foundation of China (LZ18E030001 and LY17E020002). B. W. gratefully acknowledges financial support from the China Scholarship Council.

References

1 M. Acik and S. B. Darling, *J. Mater. Chem. A*, 2016, **4**, 6185–6235.
2 V. M. Goldschmidt, *Naturwissenschaften*, 1926, **14**, 477–485.
3 Y. Tsujimoto, K. Yamaura and E. Takayama-Muromachi, *Appl. Sci.*, 2012, **2**, 206–219.
4 C. J. Bartel, C. Sutton, B. R. Goldsmith, R. Ouyang, C. B. Musgrave, L. M. Ghiringhelli and M. Scheffler, *Sci. Adv.*, 2018, **5**, eaav0693.
5 D. Lee and H. N. Lee, *Materials*, 2017, **10**, 368.
6 P. Gao, A. R. B. M. Yusoff and M. K. Nazeeruddin, *Nat. Commun.*, 2018, **9**, 5028.
7 L. L. Mao, H. Tsai, W. Y. Nie, L. Ma, J. Im, C. C. Stoumpos, C. D. Malliakas, F. Hao, M. R. Wasielewski, A. D. Mohite and M. G. Kanatzidis, *Chem. Mater.*, 2016, **28**, 7781–7792.
8 H. L. Wang, W. Z. Lv, X. X. Tang, L. F. Chen, R. F. Chen and W. Huang, *Prog. Chem.*, 2017, **29**, 859–869.
9 H. Lai, B. Kan, T. Liu, N. Zheng, Z. Xie, T. Zhou, X. Wan, X. Zhang, Y. Liu and Y. Chen, *J. Am. Chem. Soc.*, 2018, **140**, 11639–11646.
10 G. C. Xing, B. Wu, X. Y. Wu, M. J. Li, B. Du, Q. Wei, J. Guo, E. K. L. Yeow, T. C. Sum and W. Huang, *Nat. Commun.*, 2017, **8**, 14558.
11 P. F. Cheng, T. Wu, J. W. Zhang, Y. J. Li, J. X. Liu, L. Jiang, X. Mao, R. F. Lu, W. Q. Deng and K. L. Han, *J. Phys. Chem. Lett.*, 2017, **8**, 4402–4406.
12 A. Kojima, K. Teshima, Y. Shirai and T. Miyasaka, *J. Am. Chem. Soc.*, 2009, **131**, 6050–6051.
13 H. S. Kim, C. R. Lee, J. H. Im, K. B. Lee, T. Moehl, A. Marchioro, S. J. Moon, R. Humphry-Baker, J. H. Yum, J. E. Moser, M. Gratzel and N. G. Park, *Sci. Rep.*, 2012, **2**, 591.
14 F. Hao, C. C. Stoumpos, D. H. Cao, R. P. H. Chang and M. G. Kanatzidis, *Nat. Photonics*, 2014, **8**, 489–494.
15 A. J. Huckaba, S. Gharibzadeh, M. Ralaiarisoa, C. Roldan-Carmona, N. Mohammadian, G. Grancini, Y. H. Lee, P. Amsalem, E. J. Plichta, N. Koch, A. Moshaii and M. K. Nazeeruddin, *Small Methods*, 2017, **1**, 1700250.
16 T. Gatti, S. Casaluci, M. Prato, M. Salerno, F. Di Stasio, A. Ansaldo, E. Menna, A. Di Carlo and F. Bonaccorso, *Adv. Funct. Mater.*, 2016, **26**, 7443–7453.
17 J. S. Yeo, C. H. Lee, D. Jang, S. Lee, S. M. Jo, H. I. Joh and D. Y. Kim, *Nano Energy*, 2016, **30**, 667–676.
18 X. Sun, T. Lin, Q. G. Song, Y. Fu, Y. Wang, F. M. Jin, H. F. Zhao, W. L. Li, Z. S. Su and B. Chu, *RSC Adv.*, 2017, **7**, 45320–45326.
19 Y. X. Zhao, A. M. Nardes and K. Zhu, *J. Phys. Chem. Lett.*, 2014, **5**, 490–494.
20 A. Agresti, S. Pescetelli, A. L. Palma, A. E. D. Castillo, D. Konios, G. Kakavelakis, S. Razza, L. Cina, E. Kymakis, F. Bonaccorso and A. Di Carlo, *ACS Energy Lett.*, 2017, **2**, 279–287.
21 W. Z. Li, H. P. Dong, X. D. Guo, N. Li, J. W. Li, G. D. Niu and L. D. Wang, *J. Mater. Chem. A*, 2014, **2**, 20105–20111.
22 H. Li, L. M. Tao, F. H. Huang, Q. Sun, X. J. Zhao, J. B. Han, Y. Shen and M. K. Wang, *ACS Appl. Mater. Interfaces*, 2017, **9**, 38967–38976.
23 C. Y. Kuang, G. Tang, T. G. Jiu, H. Yang, H. B. Liu, B. R. Li, W. N. Luo, X. D. Li, W. J. Zhang, F. S. Lu, J. F. Fang and Y. L. Li, *Nano Lett.*, 2015, **15**, 2756–2762.
24 Q. D. Yang, J. Li, Y. H. Cheng, H. W. Li, Z. Q. Guan, B. B. Yu and S. W. Tsang, *J. Mater. Chem. A*, 2017, **5**, 9852–9858.
25 S. K. Muduli, E. Varrla, S. A. Kulkarni, G. F. Han, K. Thirumal, O. Lev, S. Mhaisalkar and N. Mathews, *J. Power Sources*, 2017, **371**, 156–161.
26 F. Giustino and H. J. Snaith, *ACS Energy Lett.*, 2016, **1**, 1233–1240.
27 National Renewable Energy Laboratory, Best Research-Cell Efficiencies, 2019.
28 F. Lang, M. A. Gluba, S. Albrecht, J. Rappich, L. Korte, B. Rech and N. H. Nickel, *J. Phys. Chem. Lett.*, 2015, **6**, 2745–2750.
29 J. H. Yu, C. H. Lee, H. I. Joh, J. S. Yeo and S. I. Na, *Nanoscale*, 2017, **9**, 17167–17173.
30 Y. C. Hsiao, T. Wu, M. X. Li, Q. Liu, W. Qin and B. Hu, *J. Mater. Chem. A*, 2015, **3**, 15372–15385.

31 J. M. Frost, K. T. Butler, F. Brivio, C. H. Hendon, M. van Schilfgaarde and A. Walsh, *Nano Lett.*, 2014, **14**, 2584–2590.
32 Y. S. Liu, Z. R. Hong, Q. Chen, W. H. Chang, H. P. Zhou, T. B. Song, E. Young, Y. Yang, J. B. You, G. Li and Y. Yang, *Nano Lett.*, 2015, **15**, 662–668.
33 M. H. Li, P. S. Shen, K. C. Wang, T. F. Guo and P. Chen, *J. Mater. Chem. A*, 2015, **3**, 9011–9019.
34 T. Salim, S. Y. Sun, Y. Abe, A. Krishna, A. C. Grimsdale and Y. M. Lam, *J. Mater. Chem. A*, 2015, **3**, 8943–8969.
35 Z. K. Liu, S. P. Lau and F. Yan, *Chem. Soc. Rev.*, 2015, **44**, 5638–5679.
36 K. S. Novoselov, V. I. Fal'ko, L. Colombo, P. R. Gellert, M. G. Schwab and K. Kim, *Nature*, 2012, **490**, 192–200.
37 A. J. Mannix, X. F. Zhou, B. Kiraly, J. D. Wood, D. Alducin, B. D. Myers, X. L. Liu, B. L. Fisher, U. Santiago, J. R. Guest, M. J. Yacaman, A. Ponce, A. R. Oganov, M. C. Hersam and N. P. Guisinger, *Science*, 2015, **350**, 1513–1516.
38 M. E. Davila, L. Xian, S. Cahangirov, A. Rubio and G. Le Lay, *New J. Phys.*, 2014, **16**, 095002.
39 D. Golberg, Y. Bando, Y. Huang, T. Terao, M. Mitome, C. C. Tang and C. Y. Zhi, *ACS Nano*, 2010, **4**, 2979–2993.
40 H. Liu, Y. C. Du, Y. X. Deng and P. D. Ye, *Chem. Soc. Rev.*, 2015, **44**, 2732–2743.
41 Q. H. Wang, K. Kalantar-Zadeh, A. Kis, J. N. Coleman and M. S. Strano, *Nat. Nanotechnol.*, 2012, **7**, 699–712.
42 S. Z. Butler, S. M. Hollen, L. Y. Cao, Y. Cui, J. A. Gupta, H. R. Gutierrez, T. F. Heinz, S. S. Hong, J. X. Huang, A. F. Ismach, E. Johnston-Halperin, M. Kuno, V. V. Plashnitsa, R. D. Robinson, R. S. Ruoff, S. Salahuddin, J. Shan, L. Shi, M. G. Spencer, M. Terrones, W. Windl and J. E. Goldberger, *ACS Nano*, 2013, **7**, 2898–2926.
43 Q. Liu, M. C. Qin, W. J. Ke, X. L. Zheng, Z. Chen, P. L. Qin, L. B. Xiong, H. W. Lei, J. W. Wan, J. Wen, G. Yang, J. J. Ma, Z. Y. Zhang and G. J. Fang, *Adv. Funct. Mater.*, 2016, **26**, 6069–6075.
44 W. Q. Wu, D. H. Chen, Y. B. Cheng and R. A. Caruso, *Sol. RRL*, 2017, **1**, 1700117.
45 Y. G. Rong, Z. L. Ku, A. Y. Mei, T. F. Liu, M. Xu, S. G. Ko, X. Li and H. W. Han, *J. Phys. Chem. Lett.*, 2014, **5**, 2160–2164.
46 C. Li, Y. H. Li, Y. J. Xing, Z. L. Zhang, X. F. Zhang, Z. Li, Y. T. Shi, T. L. Ma, R. Z. Ma, K. L. Wang and J. Q. Wei, *ACS Appl. Mater. Interfaces*, 2015, **7**, 15117–15122.
47 K. Mahmood, B. S. Swain, A. R. Kirmani and A. Amassian, *J. Mater. Chem. A*, 2015, **3**, 9051–9057.
48 J. F. Tang, Z. L. Tseng, L. C. Chen and S. Y. Chu, *Sol. Energy Mater. Sol. C*, 2016, **154**, 18–22.
49 E. Singh and H. S. Nalwa, *RSC Adv.*, 2015, **5**, 73575–73600.
50 T. Mueller, F. N. A. Xia and P. Avouris, *Nat. Photonics*, 2010, **4**, 297–301.
51 O. Lopez-Sanchez, D. Lembke, M. Kayci, A. Radenovic and A. Kis, *Nat. Nanotechnol.*, 2013, **8**, 497–501.
52 F. Bonaccorso, Z. Sun, T. Hasan and A. C. Ferrari, *Nat. Photonics*, 2010, **4**, 611–622.
53 M. Z. Cai, D. Thorpe, D. H. Adamson and H. C. Schniepp, *J. Mater. Chem.*, 2012, **22**, 24992–25002.
54 G. L. Li, G. Liu, M. Li, D. Wan, K. G. Neoh and E. T. Kang, *J. Phys. Chem. C*, 2010, **114**, 12742–12748.
55 C. M. Hill, Y. Zhu and S. Pan, *ACS Nano*, 2011, **5**, 942–951.
56 J. Kim, S. Kwon, D. H. Cho, B. Kang, H. Kwon, Y. Kim, S. O. Park, G. Y. Jung, E. Shin, W. G. Kim, H. Lee, G. H. Ryu, M. Choi, T. H. Kim, J. Oh, S. Park, S. K. Kwak, S. W. Yoon, D. Byun, Z. Lee and C. Lee, *Nat. Commun.*, 2015, **6**, 8294.
57 P. You, Z. K. Liu, Q. D. Tai, S. H. Liu and F. Yan, *Adv. Mater.*, 2015, **27**, 3632–3638.
58 Z. K. Liu, P. You, C. Xie, G. Q. Tang and F. Yan, *Nano Energy*, 2016, **28**, 151–157.
59 J. Y. Liu, Y. Z. Xue, Z. Y. Wang, Z. Q. Xu, C. X. Zheng, B. Weber, J. C. Song, Y. S. Wang, Y. R. Lu, Y. P. Zhang and Q. L. Bao, *ACS Nano*, 2016, **10**, 3536–3542.
60 Y. H. Lee, X. Q. Zhang, W. J. Zhang, M. T. Chang, C. T. Lin, K. D. Chang, Y. C. Yu, J. T. W. Wang, C. S. Chang, L. J. Li and T. W. Lin, *Adv. Mater.*, 2012, **24**, 2320–2325.
61 X. H. Hu, H. Jiang, J. Li, J. X. Ma, D. Yang, Z. K. Liu, F. Gao and S. Z. Liu, *Nanoscale*, 2017, **9**, 8274–8280.
62 A. Kumar and C. H. Lee, *Adv. Graphene Sci.*, 2013, 55–75, DOI: 10.5772/55728.
63 D. Akinwande, *Proc. SPIE*, 2014, **9083**, 90831N.
64 S. Y. Lee and S. J. Park, *Carbon Lett.*, 2012, **13**, 73–87.
65 S. Pari, A. Cuellar and B. M. Wong, *J. Phys. Chem. C*, 2016, **120**, 18871–18877.
66 R. Roldan, A. Castellanos-Gomez, E. Cappelluti and F. Guinea, *J. Phys.: Condens Mater.*, 2015, **27**, 313201.
67 J. S. Qiao, X. H. Kong, Z. X. Hu, F. Yang and W. Ji, *Nat. Commun.*, 2014, **5**, 4475.
68 J. W. Gong, H. Qiao, S. Sigdel, H. Elbohy, N. Adhikari, Z. P. Zhou, K. Sumathy, Q. F. Wei and Q. Q. Qiao, *AIP Adv.*, 2015, **5**, 067134.
69 J. H. Park, G. S. Kang, S. I. Kwon, D. G. Lim, Y. J. Choi, K. J. Choi and J. G. Park, *J. Nanosci. Nanotechnol.*, 2008, **8**, 4658–4661.
70 X. Li and H. W. Zhu, *J. Materiomics*, 2015, **1**, 33–44.
71 A. Capasso, A. E. D. Castillo, L. Najafi, V. Pellegrini, F. Bonaccorso, F. Matteocci, L. Cina and A. Di Carlo, *2015 Ieee 15th International Conference on Nanotechnology (IEEE-Nano)*, 2015, pp. 1138–1141.
72 E. Nouri, M. R. Mohammadi and P. Lianos, *Chem. Commun.*, 2017, **53**, 1630–1633.
73 G. Yoon, D. H. Seo, K. Ku, J. Kim, S. Jeon and K. Kang, *Chem. Mater.*, 2015, **27**, 2067–2073.
74 M. P. Lavin-Lopez, J. L. Valverde, L. Sanchez-Silva and A. Romero, *Ind. Eng. Chem. Res.*, 2016, **55**, 845–855.
75 B. C. Brodie, *Ann. Chim. Phys.*, 1860, **59**, 466–472.
76 S. Gambhir, R. Jalili, D. L. Officer and G. G. Wallace, *NPG Asia Mater.*, 2015, **7**, e186.
77 P. S. Chandrasekhar and V. K. Komarala, *RSC Adv.*, 2017, **7**, 28610–28615.
78 D. B. Mitzi, S. Wang, C. A. Feild, C. A. Chess and A. M. Guloy, *Science*, 1995, **267**, 1473–1476.
79 M. C. Weidman, M. Seitz, S. D. Stranks and W. A. Tisdale, *ACS Nano*, 2016, **10**, 7830–7839.

80 C. C. Stoumpos, D. H. Cao, D. J. Clark, J. Young, J. M. Rondinelli, J. I. Jang, J. T. Hupp and M. G. Kanatzidis, *Chem. Mater.*, 2016, **28**, 2852–2867.
81 F. O. Saouma, C. C. Stoumpos, J. Wong, M. G. Kanatzidis and J. I. Jang, *Nat. Commun.*, 2017, **8**, 742.
82 K. Kikuchi, Y. Takeoka, M. Rikukawa and K. Sanui, *Curr. Appl. Phys.*, 2004, **4**, 599–602.
83 J. J. Peng, Y. N. Chen, K. B. Zheng, T. Pullerits and Z. Q. Liang, *Chem. Soc. Rev.*, 2017, **46**, 5714–5729.
84 C. X. Huo, B. Cai, Z. Yuan, B. W. Ma and H. B. Zeng, *Small Methods*, 2017, **1**, 1600018.
85 P. Tyagi, S. M. Arveson and W. A. Tisdale, *J. Phys. Chem. Lett.*, 2015, **6**, 1911–1916.
86 K. Yao, X. F. Wang, Y. X. Xu, F. Li and L. Zhou, *Chem. Mater.*, 2016, **28**, 3131–3138.
87 K. Meng, S. S. Gao, L. L. Wu, G. Wang, X. Liu, G. Chen, Z. Liu and G. Chen, *Nano Lett.*, 2016, **16**, 4166–4173.
88 J. Z. Song, L. M. Xu, J. H. Li, J. Xue, Y. H. Dong, X. M. Li and H. B. Zeng, *Adv. Mater.*, 2016, **28**, 4861–4869.
89 J. Shamsi, Z. Y. Dang, P. Bianchini, C. Canale, F. Di Stasio, R. Brescia, M. Prato and L. Manna, *J. Am. Chem. Soc.*, 2016, **138**, 7240–7243.
90 S. K. Balakrishnan and P. V. Kamat, *Chem. Mater.*, 2018, **30**, 74–78.
91 S. K. Pathak, A. Abate, T. Leijtens, D. J. Hollman, J. Teuscher, L. Pazos, P. Docampo, U. Steiner and H. J. Snaith, *Adv. Energy Mater.*, 2014, **4**, 1301667.
92 A. Ng, Z. W. Ren, Q. Shen, S. H. Cheung, H. C. Gokkaya, S. K. So, A. B. Djurisic, Y. Y. Wan, X. J. Wu and C. Surya, *ACS Appl. Mater. Interfaces*, 2016, **8**, 32805–32814.
93 Y. P. Wang, Y. F. Shi, G. Q. Xin, J. Lan and J. Shi, *Cryst. Growth Des.*, 2015, **15**, 4741–4749.
94 Q. Zhang, R. Su, X. F. Liu, J. Xing, T. C. Sum and Q. H. Xiong, *Adv. Funct. Mater.*, 2016, **26**, 6238–6245.
95 S. T. Ha, X. F. Liu, Q. Zhang, D. Giovanni, T. C. Sum and Q. H. Xiong, *Adv. Opt. Mater.*, 2014, **2**, 838–844.
96 S. T. Ha, R. Su, J. Xing, Q. Zhang and Q. H. Xiong, *Chem. Sci.*, 2017, **8**, 2522–2536.
97 M. Z. Liu, M. B. Johnston and H. J. Snaith, *Nature*, 2013, **501**, 395–398.
98 I. Jeon, J. Yoon, N. Ahn, M. Atwa, C. Delacou, A. Anisimov, E. I. Kauppinen, M. Choi, S. Maruyama and Y. Matsuo, *J. Phys. Chem. Lett.*, 2017, **8**, 5395–5401.
99 J. Yoon, H. Sung, G. Lee, W. Cho, N. Ahn, H. S. Jung and M. Choi, *Energy Environ. Sci.*, 2017, **10**, 337–345.
100 M. Duan, Y. G. Rong, A. Y. Mei, Y. Hu, Y. S. Sheng, Y. J. Guan and H. W. Han, *Carbon*, 2017, **120**, 71–76.
101 J. H. Heo, D. H. Shin, S. Kim, M. H. Jang, M. H. Lee, S. W. Seo, S. H. Choi and S. H. Im, *Chem. Eng. J.*, 2017, **323**, 153–159.
102 F. Shao, Z. L. Tian, P. Qin, K. J. Bu, W. Zhao, L. Xu, D. L. Wang and F. Q. Huang, *Sci. Rep.*, 2018, **8**, 7033.
103 J. T. W. Wang, J. M. Ball, E. M. Barea, A. Abate, J. A. Alexander-Webber, J. Huang, M. Saliba, I. Mora-Sero, J. Bisquert, H. J. Snaith and R. J. Nicholas, *Nano Lett.*, 2014, **14**, 724–730.
104 C. Wang, Y. Tang, Y. J. Hu, L. Huang, J. X. Fu, J. Jin, W. M. Shi, L. J. Wang and W. G. Yang, *RSC Adv.*, 2015, **5**, 52041–52047.
105 S. W. Tong, J. Balapanuru, D. Y. Fu and K. P. Loh, *ACS Appl. Mater. Interfaces*, 2016, **8**, 29496–29503.
106 G. S. Han, Y. H. Song, Y. U. Jin, J. W. Lee, N. G. Park, B. K. Kang, J. K. Lee, I. S. Cho, D. H. Yoon and H. S. Jung, *ACS Appl. Mater. Interfaces*, 2015, **7**, 23521–23526.
107 T. Umeyama, D. Matano, J. Baek, S. Gupta, S. Ito, V. Subramanian and H. Imahori, *Chem. Lett.*, 2015, **44**, 1410–1412.
108 K. T. Cho, G. Grancini, Y. Lee, D. Konios, S. Paek, E. Kymakis and M. K. Nazeeruddin, *ChemSusChem*, 2016, **9**, 3040–3044.
109 F. Biccari, F. Gabelloni, E. Burzi, M. Gurioli, S. Pescetelli, A. Agresti, A. E. D. Castillo, A. Ansaldo, E. Kymakis, F. Bonaccorso, A. Di Carlo and A. Vinattieri, *Adv. Energy Mater.*, 2017, **7**, 1701349.
110 S. S. Mali, C. S. Shim, H. Kim and C. K. Hong, *J. Mater. Chem. A*, 2016, **4**, 12158–12169.
111 X. J. Zhao, L. M. Tao, H. Li, W. C. Huang, P. Y. Sun, J. Liu, S. S. Liu, Q. Sun, Z. F. Cui, L. J. Sun, Y. Shen, Y. Yang and M. K. Wang, *Nano Lett.*, 2018, **18**, 2442–2449.
112 M. Li, Z. K. Wang, T. Kang, Y. G. Yang, X. Y. Gao, C. S. Hsu, Y. L. Li and L. S. Liao, *Nano Energy*, 2018, **43**, 47–54.
113 J. S. Li, T. G. Jiu, C. H. Duan, Y. Wang, H. N. Zhang, H. M. Jian, Y. J. Zhao, N. Wang, C. S. Huang and Y. L. Li, *Nano Energy*, 2018, **46**, 331–337.
114 P. Huang, L. G. Yuan, K. C. Zhang, Q. Y. Chen, Y. Zhou, B. Song and Y. F. Li, *ACS Appl. Mater. Interfaces*, 2018, **10**, 14796–14802.
115 G. Yang, H. W. Lei, H. Tao, X. L. Zheng, J. J. Ma, Q. Liu, W. J. Ke, Z. L. Chen, L. B. Xiong, P. L. Qin, Z. Chen, M. C. Qin, X. H. Lu, Y. F. Yan and G. J. Fang, *Small*, 2017, **13**, 1601769.
116 J. C. Yu, J. A. Hong, E. D. Jung, D. Bin Kim, S. M. Baek, S. Lee, S. Cho, S. S. Park, K. J. Choi and M. H. Song, *Sci. Rep.*, 2018, **8**, 1070.
117 D. Y. Lee, S. I. Na and S. S. Kim, *Nanoscale*, 2016, **8**, 1513–1522.
118 D. Li, J. Cui, H. Li, D. K. Huang, M. K. Wang and Y. Shen, *Sol. Energy*, 2016, **131**, 176–182.
119 J. S. Yeo, R. Kang, S. Lee, Y. J. Jeon, N. Myoung, C. L. Lee, D. Y. Kim, J. M. Yun, Y. H. Seo, S. S. Kim and S. I. Na, *Nano Energy*, 2015, **12**, 96–104.
120 X. Huang, H. Guo, J. Yang, K. Wang, X. B. Niu and X. B. Liu, *Org. Electron.*, 2016, **39**, 288–295.
121 J. Y. Xiao, J. J. Shi, H. B. Liu, Y. Z. Xu, S. T. Lv, Y. H. Luo, D. M. Li, Q. B. Meng and Y. L. Li, *Adv. Energy Mater.*, 2015, **5**, 1401943.
122 J. Li, M. Zhao, C. Zhao, H. Jian, N. Wang, L. Yao, C. Huang, Y. Zhao and T. Jiu, *ACS Appl. Mater. Interfaces*, 2018, **11**, 2626–2631.
123 G. Kakavelakis, I. Paradisanos, B. Paci, A. Generosi, M. Papachatzakis, T. Maksudov, L. Najafi, A. E. D. Castillo, G. Kioseoglou, E. Stratakis, F. Bonaccorso and E. Kymakis, *Adv. Energy Mater.*, 2018, **8**, 1702287.
124 Y. G. Kim, K. C. Kwon, Q. Van Le, K. Hong, H. W. Jang and S. Y. Kim, *J. Power Sources*, 2016, **319**, 1–8.

125 P. Huang, Z. W. Wang, Y. F. Liu, K. C. Zhang, L. G. Yuan, Y. Zhou, B. Song and Y. F. Li, *ACS Appl. Mater. Interfaces*, 2017, **9**, 25323–25331.
126 A. Capasso, F. Matteocci, L. Najafi, M. Prato, J. Buha, L. Cina, V. Pellegrini, A. Di Carlo and F. Bonaccorso, *Adv. Energy Mater.*, 2016, **6**, 1600920.
127 N. Arora, M. I. Dar, A. Hinderhofer, N. Pellet, F. Schreiber, S. M. Zakeeruddin and M. Gratzel, *Science*, 2017, **358**, 768–771.
128 X. N. Zhang, G. W. Ji, D. B. Xiong, Z. H. Su, B. Zhao, K. C. Shen, Y. G. Yang and X. Y. Gao, *RSC Adv.*, 2018, **8**, 987–993.
129 H. H. Tsai, W. Y. Nie, J. C. Blancon, C. C. S. Toumpos, R. Asadpour, B. Harutyunyan, A. J. Neukirch, R. Verduzco, J. J. Crochet, S. Tretiak, L. Pedesseau, J. Even, M. A. Alam, G. Gupta, J. Lou, P. M. Ajayan, M. J. Bedzyk, M. G. Kanatzidis and A. D. Mohite, *Nature*, 2016, **536**, 312–316.
130 I. C. Smith, E. T. Hoke, D. Solis-Ibarra, M. D. McGehee and H. I. Karunadasa, *Angew. Chem., Int. Ed.*, 2014, **53**, 11232–11235.
131 Q. B. Cai, H. T. Li, Y. X. Jiang, L. M. Tu, L. Ma, X. J. Wu, S. E. Yang, Z. F. Shi, J. H. Zang and Y. S. Chen, *Sol. Energy*, 2018, **159**, 786–793.
132 Y. Q. Liao, H. F. Liu, W. J. Zhou, D. W. Yang, Y. Q. Shang, Z. F. Shi, B. H. Li, X. Y. Jiang, L. J. Zhang, L. N. Quan, R. Quintero-Bermudez, B. R. Sutherland, Q. X. Mi, E. H. Sargent and Z. L. Ning, *J. Am. Chem. Soc.*, 2017, **139**, 6693–6699.
133 G. Grancini, C. Roldan-Carmona, I. Zimmermann, E. Mosconi, X. Lee, D. Martineau, S. Narbey, F. Oswald, F. De Angelis, M. Graetzel and M. K. Nazeeruddin, *Nat. Commun.*, 2017, **8**, 15684.
134 A. Abate, J. P. Correa-Baena, M. Saliba, M. S. Su'ait and F. Bella, *Chem. – Eur. J.*, 2018, **24**, 3083–3100.
135 H. Sung, N. Ahn, M. S. Jang, J. K. Lee, H. Yoon, N. G. Park and M. Choi, *Adv. Energy Mater.*, 2016, **6**, 1501873.
136 C. Lee, X. D. Wei, J. W. Kysar and J. Hone, *Science*, 2008, **321**, 385–388.
137 Z. Chen, B. Cotterell and W. Wang, *Eng. Fract. Mech.*, 2002, **69**, 597–603.
138 N. Liu, A. Chortos, T. Lei, L. H. Jin, T. R. Kim, W. G. Bae, C. X. Zhu, S. H. Wang, R. Pfattner, X. Y. Chen, R. Sinclair and Z. A. Bao, *Sci. Adv.*, 2017, **3**, e1700159.
139 D. H. Shin, S. Kim, J. M. Kim, C. W. Jang, J. H. Kim, K. W. Lee, J. Kim, S. D. Oh, D. H. Lee, S. S. Kang, C. O. Kim, S. H. Choi and K. J. Kim, *Adv. Mater.*, 2015, **27**, 2614–2620.
140 J. M. Kim, S. Kim and S. H. Choi, *ACS Sustainable Chem. Eng.*, 2019, **7**, 734–739.
141 S. J. Kwon, T. H. Han, Y. H. Kim, T. Ahmed, H. K. Seo, H. Kim, D. J. Kim, W. Xu, B. H. Hong, J. X. Zhu and T. W. Lee, *ACS Appl. Mater. Interfaces*, 2018, **10**, 4874–4881.
142 G. Yang, H. Tao, P. L. Qin, W. J. Ke and G. J. Fang, *J. Mater. Chem. A*, 2016, **4**, 3970–3990.
143 K. C. Kwon, K. S. Choi and S. Y. Kim, *Adv. Funct. Mater.*, 2012, **22**, 4724–4731.
144 J. M. Yun, Y. J. Noh, J. S. Yeo, Y. J. Go, S. I. Na, H. G. Jeong, J. Kim, S. Lee, S. S. Kim, H. Y. Koo, T. W. Kim and D. Y. Kim, *J. Mater. Chem. C*, 2013, **1**, 3777–3783.
145 G. Jo, S. I. Na, S. H. Oh, S. Lee, T. S. Kim, G. Wang, M. Choe, W. Park, J. Yoon, D. Y. Kim, Y. H. Kahng and T. Lee, *Appl. Phys. Lett.*, 2010, **97**, 213301.
146 K. S. Novoselov, A. K. Geim, S. V. Morozov, D. Jiang, Y. Zhang, S. V. Dubonos, I. V. Grigorieva and A. A. Firsov, *Science*, 2004, **306**, 666–669.
147 G. V. Dubacheva, C. K. Liang and D. M. Bassani, *Coord. Chem. Rev.*, 2012, **256**, 2628–2639.
148 J. Liu, M. Durstock and L. M. Dai, *Energy Environ. Sci.*, 2014, **7**, 1297–1306.
149 M. I. Ahmed, Z. Hussain, M. Mujahid, A. N. Khan, S. S. Javaid and A. Habib, *AIP Adv.*, 2016, **6**, 065303.
150 P. Tiwana, P. Docampo, M. B. Johnston, H. J. Snaith and L. M. Herz, *ACS Nano*, 2011, **5**, 5158–5166.
151 H. J. Snaith and M. Gratzel, *Adv. Mater.*, 2006, **18**, 1910–1914.
152 P. Yang, Z. J. Hu, X. C. Zhao, D. Chen, H. Lin, X. C. Lai and L. J. Yang, *ChemistrySelect*, 2017, **2**, 9433–9437.
153 M. F. M. Noh, C. H. Teh, R. Daik, E. L. Lim, C. C. Yap, M. A. Ibrahim, N. A. Ludin, A. B. Yusoff, J. Jang and M. A. M. Terid, *J. Mater. Chem. C*, 2018, **6**, 682–712.
154 R. L. Z. Hoye, K. P. Musselman and J. L. MacManus-Driscoll, *APL Mater.*, 2013, **1**, 060701.
155 M. M. Tavakoli, R. Tavakoli, P. Yadav and J. Kong, *J. Mater. Chem. A*, 2019, **7**, 679–686.
156 M. H. Zhu, W. W. Liu, W. J. Ke, L. S. Xie, P. Dong and F. Hao, *ACS Appl. Mater. Interfaces*, 2019, **11**, 666–673.
157 J. I. Fujisawa, T. Eda and M. Hanaya, *Chem. Phys. Lett.*, 2017, **685**, 23–26.
158 J. H. Qiu, Y. C. Qiu, K. Y. Yan, M. Zhong, C. Mu, H. Yan and S. H. Yang, *Nanoscale*, 2013, **5**, 3245–3248.
159 S. Y. Shao, M. Abdu-Aguye, L. Qiu, L. H. Lai, J. Liu, S. Adjokatse, F. Jahani, M. E. Kamminga, G. H. ten Brink, T. T. M. Palstra, B. J. Kooi, J. C. Hummelen and M. A. Loi, *Energy Environ. Sci.*, 2016, **9**, 2444–2452.
160 G. Kakavelakis, T. Maksudov, D. Konios, I. Paradisanos, G. Kioseoglou, E. Stratakis and E. Kymakis, *Adv. Energy Mater.*, 2017, **7**, 1602120.
161 D. Yang, R. X. Yang, X. D. Ren, X. J. Zhu, Z. Yang, C. Li and S. Z. Liu, *Adv. Mater.*, 2016, **28**, 5206–5213.
162 M. J. Zhang, X. X. Wang, H. J. Sun, N. Wang, Q. Lv, W. W. Cui, Y. Z. Long and C. S. Huang, *Sci. Rep.*, 2017, **7**, 11535.
163 J. J. Zheng, X. Zhao, Y. L. Zhao and X. F. Gao, *Sci. Rep.*, 2013, **3**, 1271.
164 F. Chang, L. J. Huang, Y. R. Li, C. Z. Guo and Q. Z. Diao, *Int. J. Electrochem. Sci.*, 2017, **12**, 10348–10358.
165 A. Savva, I. Burgues-Ceballos and S. A. Choulis, *Adv. Energy Mater.*, 2016, **6**, 1600285.
166 M. D. Ye, C. F. He, J. Iocozzia, X. Q. Liu, X. Cui, X. T. Meng, M. Rager, X. D. Hong, X. Y. Liu and Z. Q. Lin, *J. Phys. D: Appl. Phys.*, 2017, **50**, 373002.
167 L. Etgar, P. Gao, Z. S. Xue, Q. Peng, A. K. Chandiran, B. Liu, M. K. Nazeeruddin and M. Gratzel, *J. Am. Chem. Soc.*, 2012, **134**, 17396–17399.
168 Q. Chen, H. P. Zhou, T. B. Song, S. Luo, Z. R. Hong, H. S. Duan, L. T. Dou, Y. S. Liu and Y. Yang, *Nano Lett.*, 2014, **14**, 4158–4163.

169 A. K. Jena, Y. Numata, M. Ikegami and T. Miyasaka, *J. Mater. Chem. A*, 2018, **6**, 2219–2230.
170 J. B. You, L. Meng, T. B. Song, T. F. Guo, Y. Yang, W. H. Chang, Z. R. Hong, H. J. Chen, H. P. Zhou, Q. Chen, Y. S. Liu, N. De Marco and Y. Yang, *Nat. Nanotechnol.*, 2016, **11**, 75–81.
171 L. Calio, J. Follana-Berna, S. Kazim, M. Madsen, H. G. Rubahn, A. Sastre-Santos and S. Ahmad, *Sustainable Energy Fuels*, 2017, **1**, 2071–2077.
172 G. A. Sepalage, S. Meyer, A. Pascoe, A. D. Scully, F. Z. Huang, U. Bach, Y. B. Cheng and L. Spiccia, *Adv. Funct. Mater.*, 2015, **25**, 5650–5661.
173 S. S. Li, K. H. Tu, C. C. Lin, C. W. Chen and M. Chhowalla, *ACS Nano*, 2010, **4**, 3169–3174.
174 Z. W. Wu, S. Bai, J. Xiang, Z. C. Yuan, Y. G. Yang, W. Cui, X. Y. Gao, Z. Liu, Y. Z. Jin and B. Q. Sun, *Nanoscale*, 2014, **6**, 10505–10510.
175 Y. Gao, H. L. Yip, K. S. Chen, K. M. O'Malley, O. Acton, Y. Sun, G. Ting, H. Z. Chen and A. K. Y. Jen, *Adv. Mater.*, 2011, **23**, 1903–1908.
176 V. Strelko, D. J. Malik and M. Streat, *Carbon*, 2002, **40**, 95–104.
177 X. Z. Gong, G. Z. Liu, Y. S. Li, D. Y. W. Yu and W. Y. Teoh, *Chem. Mater.*, 2016, **28**, 8082–8118.
178 E. Jokar, Z. Y. Huang, S. Narra, C. Y. Wang, V. Kattoor, C. C. Chung and E. W. G. Diau, *Adv. Energy Mater.*, 2018, **8**, 1701640.
179 C. Bi, Q. Wang, Y. C. Shao, Y. B. Yuan, Z. G. Xiao and J. S. Huang, *Nat. Commun.*, 2015, **6**, 7747.
180 X. W. Yin, Y. Zhou, J. H. Han, H. Nan, M. Q. Tai, Y. C. Gu, J. B. Li and H. Lin, *J. Mater. Chem. A*, 2018, **6**, 20702–20711.
181 Q. F. Dong, Y. B. Yuan, Y. C. Shao, Y. J. Fang, Q. Wang and J. S. Huang, *Energy Environ. Sci.*, 2015, **8**, 2464–2470.
182 A. L. Palma, L. Cina, S. Pescetelli, A. Agresti, M. Raggio, R. Paolesse, F. Bonaccorso and A. Di Carlo, *Nano Energy*, 2016, **22**, 349–360.
183 W. Z. Li, H. P. Dong, L. D. Wang, N. Li, X. D. Guo, J. W. Li and Y. Qiu, *J. Mater. Chem. A*, 2014, **2**, 13587–13592.
184 J. M. Yun, J. S. Yeo, J. Kim, H. G. Jeong, D. Y. Kim, Y. J. Noh, S. S. Kim, B. C. Ku and S. I. Na, *Adv. Mater.*, 2011, **23**, 4923–4928.
185 V. Singh, D. Joung, L. Zhai, S. Das, S. I. Khondaker and S. Seal, *Prog. Mater. Sci.*, 2011, **56**, 1178–1271.
186 D. W. Johnson, B. P. Dobson and K. S. Coleman, *Curr. Opin. Colloid Interface Sci.*, 2015, **20**, 367–382.
187 H. Luo, X. H. Lin, X. Hou, L. K. Pan, S. M. Huang and X. H. Chen, *Nano-Micro Lett.*, 2017, **9**, 39.
188 K. Ahmad and S. M. Mobin, *New J. Chem.*, 2017, **41**, 14253–14258.
189 S. Y. Wang, X. N. Huang, H. X. Sun and C. Y. Wu, *Nanoscale Res. Lett.*, 2017, **12**, 619.
190 A. Giuri, S. Masi, S. Colella, A. Listorti, A. Rizzo, A. Kovtun, S. Dell'Elce, A. Liscio and C. E. Corcione, *Polym. Eng. Sci.*, 2017, **57**, 546–552.
191 J. Z. Niu, D. Yang, X. D. Ren, Z. Yang, Y. C. Liu, X. J. Zhu, W. G. Zhao and S. Z. Liu, *Org. Electron.*, 2017, **48**, 165–171.
192 D. A. Mengistie, M. A. Ibrahem, P. C. Wang and C. W. Chu, *ACS Appl. Mater. Interfaces*, 2014, **6**, 2292–2299.
193 Z. Y. Jiang, X. H. Chen, X. H. Lin, X. K. Jia, J. F. Wang, L. K. Pan, S. M. Huang, F. R. Zhu and Z. Sun, *Sol. Energy Mater. Sol. Cells*, 2016, **146**, 35–43.
194 J. S. Yeo, J. M. Yun, D. Y. Kim, S. Park, S. S. Kim, M. H. Yoon, T. W. Kim and S. I. Na, *ACS Appl. Mater. Interfaces*, 2012, **4**, 2551–2560.
195 J. W. Liu, S. Pathak, T. Stergiopoulos, T. Leijtens, K. Wojciechowski, S. Schumann, N. Kausch-Busies and H. J. Snaith, *J. Phys. Chem. Lett.*, 2015, **6**, 1666–1673.
196 Y. Hou, H. Zhang, W. Chen, S. Chen, C. O. R. Quiroz, H. Azimi, A. Osvet, G. J. Matt, E. Zeira, J. Seuring, N. Kausch-Busies, W. Lovenich and C. J. Brabec, *Adv. Energy Mater.*, 2015, **5**, 1500543.
197 A. Giuri, S. A. Masi, S. Colella, A. Kovtun, S. Dell'Elce, E. Treossi, A. Liscio, C. E. Corcione, A. Rizzo and A. Listorti, *Adv. Funct. Mater.*, 2016, **26**, 6985–6994.
198 Z. C. He, C. M. Zhong, X. Huang, W. Y. Wong, H. B. Wu, L. W. Chen, S. J. Su and Y. Cao, *Adv. Mater.*, 2011, **23**, 4636–4643.
199 T. H. Han, M. R. Choi, S. H. Woo, S. Y. Min, C. L. Lee and T. W. Lee, *Adv. Mater.*, 2012, **24**, 1487–1493.
200 K. G. Lim, S. Ahn, Y. H. Kim, Y. B. Qi and T. W. Lee, *Energy Environ. Sci.*, 2016, **9**, 932–939.
201 J. Ye, X. L. Li, J. J. Zhao, X. L. Mei and Q. Li, *RSC Adv.*, 2016, **6**, 36356–36361.
202 T. Gatti, F. Lamberti, P. Topolovsek, M. Abdu-Aguye, R. Sorrentino, L. Perino, M. Salerno, L. Girardi, C. Marega, G. A. Rizzi, M. A. Loi, A. Petrozza and E. Menna, *Sol. RRL*, 2018, **2**, 1800013.
203 G. J. Zhao, Y. J. He and Y. F. Li, *Adv. Mater.*, 2010, **22**, 4355–4358.
204 N. Boulanger, V. Yu, M. Hilke, M. F. Toney and D. R. Barbero, *Phys. Chem. Chem. Phys.*, 2017, **19**, 8496–8503.
205 T. Gatti, N. Vicentini, M. Mba and E. Menna, *Eur. J. Org. Chem.*, 2016, 1071–1090, DOI: 10.1002/ejoc.201501411.
206 T. Kuilla, S. Bhadra, D. H. Yao, N. H. Kim, S. Bose and J. H. Lee, *Prog. Polym. Sci.*, 2010, **35**, 1350–1375.
207 J. S. Li, M. Zhao, C. J. Zhao, H. M. Jian, N. Wang, L. L. Yao, C. S. Huang, Y. J. Zhao and T. G. Jiu, *ACS Appl. Mater. Interfaces*, 2019, **11**, 2626–2631.
208 C. S. Huang, Y. J. Li, N. Wang, Y. R. Xue, Z. C. Zuo, H. B. Liu and Y. L. Li, *Chem. Rev.*, 2018, **118**, 7744–7803.
209 K. F. Mak, C. Lee, J. Hone, J. Shan and T. F. Heinz, *Phys. Rev. Lett.*, 2010, **105**, 136805.
210 A. M. van der Zande, P. Y. Huang, D. A. Chenet, T. C. Berkelbach, Y. M. You, G. H. Lee, T. F. Heinz, D. R. Reichman, D. A. Muller and J. C. Hone, *Nat. Mater.*, 2013, **12**, 554–561.
211 Y. Wang, R. Fullon, M. Acerce, C. E. Petoukhoff, J. Yang, C. G. Chen, S. N. Du, S. K. Lai, S. P. Lau, D. Voiry, D. O'Carroll, G. Gupta, A. D. Mohite, S. D. Zhang, H. Zhou and M. Chhowalla, *Adv. Mater.*, 2017, **29**, 1603995.
212 W. J. Zhao, R. M. Ribeiro and G. Eda, *Acc. Chem. Res.*, 2015, **48**, 91–99.

213 R. Kappera, D. Voiry, S. E. Yalcin, B. Branch, G. Gupta, A. D. Mohite and M. Chhowalla, *Nat. Mater.*, 2014, **13**, 1128–1134.
214 U. Dasgupta, S. Chatterjee and A. J. Pal, *Sol. Energy Mater. Sol. Cells*, 2017, **172**, 353–360.
215 B. Peng, G. N. Yu, Y. W. Zhao, Q. Xu, G. C. Xing, X. F. Liu, D. Y. Fu, B. Liu, J. R. S. Tan, W. Tang, H. P. Lu, J. L. Xie, L. J. Deng, T. C. Sum and K. P. Loh, *ACS Nano*, 2016, **10**, 6383–6391.
216 H. P. Komsa and A. V. Krasheninnikov, *Phys. Rev. B: Condens. Matter Mater. Phys.*, 2015, **91**, 125304.
217 Y. Xu and M. A. A. Schoonen, *Am. Mineral.*, 2000, **85**, 543–556.
218 R. N. Dai, Y. Y. Wang, J. Wang and X. Y. Deng, *ChemSusChem*, 2017, **10**, 2869–2874.
219 H. Liu, A. T. Neal, Z. Zhu, Z. Luo, X. F. Xu, D. Tomanek and P. D. Ye, *ACS Nano*, 2014, **8**, 4033–4041.
220 J. Kim, S. S. Baik, S. H. Ryu, Y. Sohn, S. Park, B. G. Park, J. Denlinger, Y. Yi, H. J. Choi and K. S. Kim, *Science*, 2015, **349**, 723–726.
221 M. Batmunkh, M. Bat-Erdene and J. G. Shapter, *Adv. Mater.*, 2016, **28**, 8586–8617.
222 A. Jain and A. J. H. McGaughey, *Sci. Rep.*, 2015, **5**, 8501.
223 B. C. Deng, V. Tran, Y. J. Xie, H. Jiang, C. Li, Q. S. Guo, X. M. Wang, H. Tian, S. J. Koester, H. Wang, J. J. Cha, Q. F. Xia, L. Yang and F. N. Xia, *Nat. Commun.*, 2017, **8**, 14474.
224 L. K. Li, Y. J. Yu, G. J. Ye, Q. Q. Ge, X. D. Ou, H. Wu, D. L. Feng, X. H. Chen and Y. B. Zhang, *Nat. Nanotechnol.*, 2014, **9**, 372–377.
225 B. Liu, M. Q. Long, M. Q. Cai and J. L. Yang, *Appl. Phys. Lett.*, 2018, **112**, 043901.
226 B. Liu, M. Q. Long, M. Q. Cai and J. L. Yang, *J. Phys. Chem. Lett.*, 2018, **9**, 4822–4827.
227 X. Tong, F. Lin, J. Wu and Z. M. M. Wang, *Adv. Sci.*, 2016, **3**, 1500201.
228 D. P. Guo, J. G. Yu, K. Fan, H. Y. Zou and B. W. He, *Sol. Energy Mater. Sol. Cells*, 2017, **159**, 518–525.
229 Z. H. Liu, M. Zhang, X. B. Xu, L. L. Bu, W. J. Zhang, W. H. Li, Z. X. Zhao, M. K. Wang, Y. B. Cheng and H. S. He, *Dalton Trans.*, 2015, **44**, 3967–3973.
230 Z. W. Ren, J. Wang, Z. X. Pan, K. Zhao, H. Zhang, Y. Li, Y. X. Zhao, I. Mora-Sero, J. Bisquert and X. H. Zhong, *Chem. Mater.*, 2015, **27**, 8398–8405.
231 E. Nouri, Y. L. Wang, Q. Chen, J. J. Xu, G. Paterakis, V. Dracopoulos, Z. X. Xu, D. Tasis, M. R. Mohammadi and P. Lianos, *Electrochim. Acta*, 2017, **233**, 36–43.
232 N. Wijeyasinghe, A. Regoutz, F. Eisner, T. Du, L. Tsetseris, Y. H. Lin, H. Faber, P. Pattanasattayavong, J. H. Li, F. Yan, M. A. McLachlan, D. J. Payne, M. Heeney and T. D. Anthopoulos, *Adv. Funct. Mater.*, 2017, **27**, 1701818.
233 S. Guarnera, A. Abate, W. Zhang, J. M. Foster, G. Richardson, A. Petrozza and H. J. Snaith, *J. Phys. Chem. Lett.*, 2015, **6**, 432–437.
234 A. Agresti, S. Pescetelli, B. Taheri, A. E. D. Castillo, L. Cina, F. Bonaccorso and A. Di Carlo, *ChemSusChem*, 2016, **9**, 2609–2619.
235 B. B. Li, Y. F. Li, C. Y. Zheng, D. Q. Gao and W. Huang, *RSC Adv.*, 2016, **6**, 38079–38091.
236 S. F. Pei, J. P. Zhao, J. H. Du, W. C. Ren and H. M. Cheng, *Carbon*, 2010, **48**, 4466–4474.
237 L. Najafi, B. Taheri, B. Martin-Garcia, S. Bellani, D. Di Girolamo, A. Agresti, R. Oropesa-Nunez, S. Pescetelli, L. Vesce, E. Calabro, M. Prato, A. E. D. Castillo, A. Di Carlo and F. Bonaccorso, *ACS Nano*, 2018, **12**, 10736–10754.
238 G. Volonakis and F. Giustino, *J. Phys. Chem. Lett.*, 2015, **6**, 2496–2502.
239 S. J. Zhang, P. Audebert, Y. Wei, A. Al Choueiry, G. Lanty, A. Brehier, L. Galmiche, G. Clavier, C. Boissiere, J. S. Lauret and E. Deleporte, *Materials*, 2010, **3**, 3385–3406.
240 J. Jagielski, S. Kumar, W. Y. Yu and C. J. Shih, *J. Mater. Chem. C*, 2017, **5**, 5610–5627.
241 L. T. Dou, A. B. Wong, Y. Yu, M. L. Lai, N. Kornienko, S. W. Eaton, A. Fu, C. G. Bischak, J. Ma, T. N. Ding, N. S. Ginsberg, L. W. Wang, A. P. Alivisatos and P. D. Yang, *Science*, 2015, **349**, 1518–1521.
242 J. X. Liu, J. Leng, K. F. Wu, J. Zhang and S. Y. Jin, *J. Am. Chem. Soc.*, 2017, **139**, 1432–1435.
243 M. Safdari, P. H. Svensson, M. T. Hoang, I. Oh, L. Kloo and J. M. Gardner, *J. Mater. Chem. A*, 2016, **4**, 15638–15646.
244 N. Zhou, Y. H. Shen, L. Li, S. Q. Tan, N. Liu, G. H. J. Zheng, Q. Chen and H. P. Zhou, *J. Am. Chem. Soc.*, 2018, **140**, 459–465.
245 X. Zhang, X. D. Ren, B. Liu, R. Munir, X. J. Zhu, D. Yang, J. B. Li, Y. C. Liu, D. M. Smilgies, R. P. Li, Z. Yang, T. Q. Niu, X. L. Wang, A. Amassian, K. Zhao and S. Z. F. Liu, *Energy Environ. Sci.*, 2017, **10**, 2095–2102.
246 Y. H. Hu, J. Schlipf, M. Wussler, M. L. Petrus, W. Jaegermann, T. Bein, P. Muller-Buschbaum and P. Docampo, *ACS Nano*, 2016, **10**, 5999–6007.
247 L. L. Mao, C. C. Stoumpos and M. G. Kanatzidis, *J. Am. Chem. Soc.*, 2019, **141**, 1171–1190.
248 S. Ma, M. L. Cai, T. Cheng, X. H. Ding, X. Q. Shi, A. Alsaedi, T. Hayat, Y. Ding, Z. Tan and S. Y. Dai, *Sci. China Mater.*, 2018, **61**, 1257–1277.
249 E. Nouri, M. R. Mohammadi and P. Lianos, *Carbon*, 2018, **126**, 208–214.
250 G. D. Niu, X. D. Guo and L. D. Wang, *J. Mater. Chem. A*, 2015, **3**, 8970–8980.
251 G. Volonakis and F. Giustino, *Adv. Mater. Interfaces*, 2018, **5**, 1800496.
252 D. H. Cao, C. C. Stoumpos, O. K. Farha, J. T. Hupp and M. G. Kanatzidis, *J. Am. Chem. Soc.*, 2015, **137**, 7843–7850.
253 A. R. b. M. N. Yusoff and M. K. Nazeeruddin, *Adv. Energy Mater.*, 2017, **8**, 1702073.
254 L. Etgar, *Energy Environ. Sci.*, 2018, **11**, 234–242.
255 D. S. Yu, Y. Yang, M. Durstock, J. B. Baek and L. M. Dai, *ACS Nano*, 2010, **4**, 5633–5640.
256 M. J. Deka, U. Baruah and D. Chowdhury, *Mater. Chem. Phys.*, 2015, **163**, 236–244.
257 D. Kiriya, M. Tosun, P. D. Zhao, J. S. Kang and A. Javey, *J. Am. Chem. Soc.*, 2014, **136**, 7853–7856.